

TOPICS IN HADRONIC PHYSICS

By
Alfred Tang

A DISSERTATION SUBMITTED IN
PARTIAL FULFILLMENT OF THE
REQUIREMENTS FOR THE DEGREE OF

DOCTOR OF PHILOSOPHY

IN
PHYSICS

at
The University of Wisconsin-Milwaukee
August, 2002

TOPICS IN HADRONIC PHYSICS

By
Alfred Tang

A DISSERTATION SUBMITTED IN
PARTIAL FULFILLMENT OF THE
REQUIREMENTS FOR THE DEGREE OF

DOCTOR OF PHILOSOPHY

IN
PHYSICS

at
The University of Wisconsin-Milwaukee
August, 2002

John W. Norbury

Date

Graduate School Approval

Date

TOPICS IN HADRONIC PHYSICS

By
Alfred Tang

The University of Wisconsin-Milwaukee, 2002
Under the Supervision of Professor John W. Norbury

ABSTRACT

Hadron production cross sections are calculated in the perturbative QCD framework. Parton distribution functions are obtained from a string-soliton model. The fragmentation functions are derived from the Lund model of string breaking.

John W. Norbury

Date

© Copyright 2002
by
Alfred Tang

Dedication

To the pursuit of Truth and Beauty that distinguishes humanity.

καί ἡ ἀλήθεια ἐλευθερώσει ὑμᾶς.

Contents

Dedication	ii
1 Introduction	1
1.1 Notations	2
1.1.1 Particle Physics Notations	2
1.1.2 String Theory Notations	2
2 Regge Trajectories	4
2.1 A Brief History	4
2.1.1 Theoretical Developments	5
2.1.2 Construction of Regge Trajectories	8
2.2 Linearity	10
2.2.1 Zone Test	10
2.2.2 Conclusions from Zone Test	11
2.3 Divergence	12
2.4 Parallelism	13
2.5 Summary	13
3 Nystrom Plus Correction Method	33
3.1 The Basis Function Method	34
3.2 The Nystrom Method	37
3.3 The Correction Method	39
3.4 Exact S-state Solution	42
3.5 Numerical Results for the S-state	43
3.6 $l \neq 0$ Kernels	43

3.7	Summary	47
4	The Lund Model of String Fragmentation	52
4.1	Introduction	52
4.2	Cross Section Formulas	53
4.3	Summary	56
4.4	Future Work	56
5	Hadron Production Formulas	59
5.0.1	The Feynman-Field Model	59
5.0.2	Parameterized Cross Section Formulas	62
A	MKN Theory of Bound States	72
A.1	NRSE in Momentum Space	72
A.2	Exact Solution of NRSE with a Linear Potential	83
A.3	Summary	84
B	The Area Law of the Lund Model	87
B.1	Kinematics	87
B.2	Deriving the Area Law	89
C	The Parton Model	101
C.1	External Cross Section Formulas	101
C.2	Internal Cross Section Formulas	110
C.3	Fragmentation Functions	111
	Bibliography	116

List of Figures

- 1 Meson Regge trajectory of the $N = 1, S = 0$ singlet states. $b_1(1235)$ fails to intersect the zone. The polynomial fit is $M^2 = -0.1077J^2 + 1.6003J + 0.019$ (GeV²). The mass of $\pi(138)$ is taken to be the average of the masses of $\pi^0(135)$ and $\pi^\pm(140)$. Although there is a 6.5 % difference between the mass squares of $\pi^0(135)$ and $\pi^\pm(140)$, the test zone is virtually unchanged by this small difference because of the large mass squared of the other two mesons on the trajectory. The zone test suggests that the π trajectory is non-linear. 15
- 2 Meson Regge trajectory of the $N = 1, S = 0$ singlet states. The RPP assignment table lists K_{1B} as a nearly equal mixture of $K(1270)$ and $K(1400)$. In the graph above, we plot both constituent mesons at $J = 1$ for the sake of completeness. Neither $K(1270)$, $K(1400)$ nor their average satisfies the zone test by simple inspection. The polynomial fit of $K(495)$, $K(1270)$ and $K(1770)$ is $M^2 = 0.0737J^2 + 1.3018J + 0.245$ (GeV²). 16
- 3 Meson Regge trajectory of the $N = 1, S = 1$ third triplet states. Both $a_2(1320)$ and $\rho_3(1690)$ intersect the zone and hence this trajectory passes the zone test. Linearity is supported by the numerical zone test. The polynomial fit is $M^2 = 0.0191J^2 + 1.0629J - 0.4831$ (GeV²). The negative vertical intercept corresponds to a non-sense pole because $J < 1$ is not allowed in an $S = 1$ state. 17
- 4 Meson Regge trajectory of the $N = 1, S = 1$ third triplet states. Both $f_2(1270)$ and $\omega_3(1670)$ fail to intersect the zone. The polynomial fit is $M^2 = 0.0962J^2 + 0.7042J - 0.1837$ (GeV²). 18

5	Meson Regge trajectory of the $N = 1, S = 1$ third triplet states. $f_2'(1525)$ fails to intersect the zone. The polynomial fit is $M^2 = -0.0879J^2 + 1.5505J - 0.4234$ (GeV ²).	19
6	Meson Regge trajectory of the $N = 1, S = 1$ third triplet states. Both $K_2^*(1430)$ and $K_3^*(1780)$ fail to intersect the zone. The polynomial fit is $M^2 = -0.0535J^2 + 1.3922J - 0.5331$ (GeV ²).	20
7	Baryon Regge trajectory of $S = 1/2, P = +$ and $I = 1/2$ octet states. $N(1680)$ satisfies the zone test by simple inspection. The polynomial fit is $M^2 = 0.0207J^2 + 0.9081J + 0.4223$ (GeV).	21
8	Baryon Regge trajectory of $S = 1/2, P = +$ and $I = 0$ octet states. $\Lambda(1820)$ has a bound of $(lb, ub)(3, 2) = (3.360, 3.431)$ GeV ² which does not intersect the experimental bound of $(3.294, 3.331)$ GeV ² . $\Lambda(1820)$ fails the numerical zone test. The polynomial fit is $M^2 = 0.0180J^2 + 0.9797J + 0.7524$ (GeV).	22
9	Baryon Regge trajectory of $S = 3/2, P = +$ and $I = 3/2$ decuplet states. $\Delta(1950)$ satisfies the zone test due to the large error of $\Delta(2420)$. The polynomial fit is $M^2 = -0.029J^2 + 1.2875J - 0.3480$ (GeV).	23
10	Meson Regge trajectories of the $N = 1, S = 0$ singlet states. The series consists of the $1^1S_0, 1^1P_1$ and 1^1D_2 states. The trajectories include those illustrated in Figs. 1 and 2 as well as the D mesons. The D and D_s mesons form a group and the K and light unflavored mesons η and π form another. Global divergence is observed among groups of trajectories of large mass difference but local divergence is violated when the η trajectory (denoted by the dotted line) intersects the K and π trajectories.	24
11	Meson Regge trajectories of the $N = 1, S = 1$ first triplet states. The series consists of the 1^3P_0 and 1^3D_1 states. The trajectories labelled 1–3 are magnified in Fig. 12. Global divergence is observed here.	25

12	Meson Regge trajectories of the $N = 1, S = 1$ first triplet states. The series consists of the 1^3P_0 and 1^3D_1 states. The trajectories 1–3 are the magnifications of a subset of Fig. 11. Trajectories 1 and 2 are shifted horizontally slightly to separate the error bars. Divergence is inconclusive because of the large error bars. The actual mass of $K^*(1680)$ is 1717 MeV which causes it to appear higher than $\rho(1700)$ in the graph.	26
13	Meson Regge trajectories of the $N = 1, S = 1$ third triplet states. The series consists of the $1^3S_1, 1^3P_2, 1^3D_3,$ and 1^3F_4 states. The group of trajectories labelled 4–7 are magnified in Fig. 14. Global divergence is observed.	27
14	Meson Regge trajectories of the $N = 1, S = 1$ third triplet states. The series consists of the $1^3S_1, 1^3P_2, 1^3D_3,$ and 1^3F_4 states. The trajectories 4–7 are magnifications of a subset of the trajectories in Fig. 13 and are the same trajectories as in Figs. 3–6. Divergence is violated by these trajectories.	28
15	Meson Regge trajectories of the $N = 2, S = 1$ third triplet states. The series consists of the 2^3S_1 and 2^3P_2 states. Divergence is observed. . .	29
16	Baryon Regge trajectories of $P = +$ octet states. Due to the scarcity of data and the large error of $N(2220)$, divergence is plausible but inconclusive.	30
17	Baryon Regge trajectories of $P = +$ decuplet states. Due to the scarcity of data and the large error of $\Delta(2420)$, divergence is plausible but inconclusive.	31
18	Meson Regge trajectories of the $N = 1, 2, S = 1$ third triplet states. The series consists of the $1^3S_1, 1^3P_2, 2^3S_1$ and 2^3P_2 states. The $N = 1$ states are denoted by solid lines and $N = 2$ states by long-dashed lines. Parallelism is inconclusive due to the large error bar of $f(2010)$	32
19	Comparison between experimental $d\sigma/dx$ and the string model result. The constants used in the exponential function are chosen to fit the data and are not parameterizations. The data are published by Bailly <i>at al.</i> in <i>Zeitschrift für Physik</i> , C22 , 119 (1984).	57

20	Comparison between experimental $E d\sigma/dp_L$ and the string model result. The constants used in the exponential function are chosen to fit the data and are not parameterizations. The data are published by Ajinenko <i>at al.</i> in <i>Zeitschrift für Physik</i> , C35 , 7 (1987).	58
21	A sample plot of the Feynman-Field model for $pp \rightarrow \pi^+ X$ at different energies. The plot shows that the invariant cross section is suppressed at low \sqrt{s} and high p_T	65
22	A sample plot of the Feynman-Field model for $pp \rightarrow \pi^+ X$ at different angles. The plot shows that the invariant cross section is symmetric around $\theta_{cm} = 90^\circ$ and is suppressed at high p_T for $\theta_{cm} \neq 90^\circ$	66
23	Comparisons of pQCD and parameterized cross sections with $pp \rightarrow \pi^0 X$ experimental data at $\bar{\theta}_{cm} = 90^\circ$. The parameter n in fragmentation functions of the Feynman-Field model are adjusted freely as shown in the graph to fit the data. The references of the data sets Adams 96, Demarzo 87 and Akesson 89 are PR D53 4747 (1996), PR D36 16 (1987) and CERN-EP/89-98 (Aug 1989) respectively.	68
24	Comparisons of pQCD and parameterized cross sections with $pp \rightarrow \pi^+ X$ experimental data at $\bar{\theta}_{cm} = 90^\circ$. The parameter n in fragmentation functions of the Feynman-Field model are adjusted freely as shown in the graph to fit the data. The references of the data sets Abramov 81, Jaffe 89 and Busser 76 are ZETFP 33 304 (1981), PR D40 2777 (1989) and NP B1061 (1976) respectively.	69
25	Comparisons of pQCD and parameterized cross sections with $pp \rightarrow \pi^- X$ experimental data at $\bar{\theta}_{cm} = 90^\circ$. The parameter n in fragmentation functions of the Feynman-Field model are adjusted freely as shown in the graph to fit the data. The references of the data sets Abramov 81, Jaffe 89 and Busser 76 are ZETFP 33 304 (1981), PR D40 2777 (1989) and NP B1061 (1976) respectively.	70
26	Comparisons pQCD and parameterized cross sections with $pp \rightarrow \pi^+ X$ experimental data at various energies and angles. The parameter n in fragmentation functions of the Feynman-Field model are adjusted freely as shown in the graph to fit the data. The experimental data set is produced by Antreasyan and published in PRL 38, 112 (1977). . .	71

27	The graph of the Airy function—The zeros are all negative. Since $S = rR$, S must be zero at the origin $r = 0$. The eigen-energy acts like a horizontal shift which shifts the origin back to a zero.	86
28	The yoyo motion of a quark-antiquark pair confined by a linear potential. The two quarks are assumed to be massless. The mass square of the meson is proportional to the area of each square. The meson shown here is at rest.	97
29	The breakup of a quark-antiquark pair along a surface of constant proper time τ . The bold arrows represents the velocities of the produced mesons. The breakup points are labelled as vertices V_1 to V_n . .	98
30	The geometry of the kinematics of two adjacent vertices V_1 and V_2 . V_1 and V_2 are vertices or spacetime positions which also represent the energy carried by the string field. The quark moves along the positive light-cone and the antiquark moves along the negative light-cone. The antiquark of V_1 combines with the quark of V_2 to produce a meson of mass m . W_{+1} is the energy of V_1 along x_+ . z_+W_{+1} is the fraction of energy used to create a quark from V_2 . W_{-2} is the energy of V_2 along x_- . z_-W_{-2} is the fraction of energy used to create an antiquark from V_1 . A_1, A_2, A_3 and m^2 are the areas of the rectangles. The figure is taken from reference [49].	99
31	The geometry of the kinematics of involving the total area of the space-time diagram such that $A_{total} = \Gamma + A_{rest}$. The total energy square $s = W_+W_-$ is represented by the rectangle labelled s . p_{\pm} is the energy of the parent quark (antiquark) along the \pm light-cone coordinates. $z_{0n}p_+$ is the fraction of energy used to create a quark from V_n . $m^2/(z_{0n}p_+)$ is the energy used to create an antiquark from V_{n-1} . The figure is taken from reference [49] with minor modifications.	100
32	Parton a of hadron A collides with parton b of hadron B producing partons c and d . The transverse momenta, p_T , of c and d are equal and opposite.	114
33	The plot of x_a versus x_b with $x_b = x_ax_2/(x_a - x_1)$. $x_a^{min} = x_1/(1 - x_2)$. The values of $x_1 = 0.5$ and $x_2 = 0.3$ are used.	115

Chapter 1

Introduction

The main purpose of this work is to develop a *fast hadron code* (FHC) that generates the Lorentz invariant hadron production cross sections, $E d^{\sigma}/dp^3$, to be used in the NASA space radiation transport codes. The theoretical frame work of this calculation is based on perturbative QCD (pQCD), more particularly the parton model. The ingredients of pQCD invariant cross section formulas are the parton distribution functions (PDF's), the internal scattering cross sections and the fragmentation functions. So far the structure of hadrons is only poorly understood. PDF's are typically parameterized from experimental data and fragmentation functions are obtained from stochastic models, such as the Lund model. The fragmentation functions cannot be calculated exactly from QCD and are either parametrized from data or simulated by Monte Carlo programs, such as Pythia and Jetset. The secondary purpose of this work is to calculate PDF's and fragmentation functions from string and soliton theories.

An effort is made to present the materials in a self-contained manner. Equations are derived explicitly whenever possible. Much of the background information is quoted in expanded appendices with step-by-step derivations, corrections and consistent notations.

1.1 Notations

Natural units used in this work such that $\hbar = c = 1$.

1.1.1 Particle Physics Notations

p	4-momentum, $p = (E, \mathbf{p})$
\mathbf{p}	3-momentum
E	total energy of a particle or the $0th$ component of p
γ	Lorentz factor defined as $\gamma = \frac{1}{\sqrt{1-v^2}}$
s	Mandelstam variable representing the total energy square in cm frame, $s = (p_1 + p_2)^2 = (p_3 + p_4)^2$ or $\sqrt{s} = E_{1cm} + E_{2cm} = E_{cm}$
t	Mandelstam variable $t = (p_3 - p_1)^2 = (p_2 - p_4)^2$
u	Mandelstam variable $u = (p_4 - p_1)^2 = (p_2 - p_3)^2$
$\frac{d^3\sigma}{dp^3/E}$	Lorentz invariant differential cross section
$\frac{d\sigma}{dE}$	spectral distribution cross section
y	rapidity defined as $\frac{1}{2} \ln \frac{E+p}{E-p}$
\overline{MS}	modified minimal subtraction scheme
LO	leading order
NLO	next-to-the-leading order
pQCD	perturbative QCD
PDF	parton distribution function
DIS	deep inelastic scattering
$\bar{\theta}_{cm}$	average angle in the center-of-momentum frame

1.1.2 String Theory Notations

p	1-dimensional momentum
p_{max}	maximum momentum of the produced particles
x	coordinate of position or fragmentation variable defined as $\frac{p_z}{p_{max}}$
t	time
p_{\pm}	\pm light-cone momentum defined as $p_{\pm} = E \pm p$
x_{\pm}	\pm light-cone configuration defined as $x_{\pm} = t \pm x$
cm	center of mass

κ	string constant
Γ	“proper time” defined as $\kappa x_+ x_- = \kappa(t^2 - x^2) = \kappa\tau^2$
V_n	n -th spacetime position or “vertex” of a breakup point along a string defined as $V_n = \kappa(x_+, x_-)$
$H(\Gamma)$	probability distribution of a vertex occurring at Γ
$f(y)$	transitional probability from one vertex to the next with rapidity y
W_{\pm}	kinetic energy of a quark or an antiquark along the \pm light-cone coordinate

Chapter 2

Regge Trajectories

Early Chew-Frautschi plots show that meson and baryon Regge trajectories are approximately linear and non-intersecting. In this paper, we reconstruct all Regge trajectories from the most recent data. Our plots show that meson trajectories are non-linear and intersecting. We also show that all current meson Regge trajectories models are ruled out by data.

2.1 A Brief History

The topic of Regge trajectories was an active area of research in the 1960's. But there is a resurgence of interest in Regge trajectories because of the quantity of new data that need analysis and the new quark models need more complete experimental fits for testing. Despite these recent interests, some authors [1, 2] are still using old data to construct Chew-Frautschi plots. In this paper, we reconstruct all Regge trajectories with the most recent data and elucidate the principles of their construction. At the end, we explain why all current meson Regge trajectories models are ruled out by data.

2.1.1 Theoretical Developments

This paper is concerned with the properties of Regge trajectories which are graphs of the total quantum number J versus mass squared M^2 over a set of particles of fixed principal quantum number N , isospin I , dimensionality of the symmetry group D , spin-parity and flavor. Variations in J and L ($J = L + S$) are equivalent when S is fixed.

Scattering processes are usually analyzed by the method of partial-waves [3, 4]. The wavefunction in the far zone has the form

$$\psi(\mathbf{r}) \simeq e^{i\mathbf{k}\cdot\mathbf{r}} + f(k, \cos \theta) \frac{e^{i\mathbf{k}\cdot\mathbf{r}}}{r}, \quad (1)$$

where θ is the angle between the wave vector \mathbf{k} and the position vector \mathbf{r} . In the case of bound states, the plane wave term is absent. The form factor f is written as a sum of partial-waves as

$$f(k^2, \cos \theta) = \sum_{l=0}^{\infty} (2l+1) a_l(k^2) P_l(\cos \theta), \quad (2)$$

$$a_l(k^2) = \frac{1}{2} \int_{-1}^1 f(k^2, \cos \theta) P_l(\cos \theta) d \cos \theta, \quad (3)$$

where l is the orbital angular momentum quantum number and P_l is the Legendre polynomial of order l . In 1959, Regge [5, 6] generalized the solution of f by complexifying angular momenta. He interpreted the simple poles of $a_l(k^2)$ on the complex l -plane to be either resonances or bound states.

Chew and Frautschi [7] applied the Regge poles theory to investigate the analyticity of $a_l(k^2)$ in the case of strong interactions. They postulated that all strongly interacting particles are self-generating (the bootstrap hypothesis) and that they must lie on Regge trajectories (Chew-Frautschi conjecture) [8].

At first, linearity was just a convenient guide in constructing the Chew-Frautschi plots because data were scarce and there were few *a priori* rules to direct the mesons and baryons into the same trajectories [9]. Once linearity was found to be a good working hypothesis, justification was given through certain assumptions in the Regge poles theory as follows: For $\text{Re } l \geq -1/2$, the partial-wave components of the scattering amplitude f have only simple poles and are functions of k^2 ,

$$a_l(k^2) \simeq \frac{\beta(k^2)}{l - \alpha(k^2)}, \quad (4)$$

where β is the residue (Regge residue) and α the position (Regge trajectory) of the simple poles. We can use Watson transformation to rewrite Eq. [2] as the Sommerfeld-Watson formula [10] to include the poles.

A Regge trajectory $J = \alpha(k^2)$ is also sometimes expressed as $J = \alpha(E)$, or more commonly in terms of the Mandelstam variable t as $J = \alpha(t)$. t is the center-of-mass energy of the quark-antiquark pair defined as $t \equiv (p_q + p_{\bar{q}})^2$. It is used instead of s or u because Regge poles generally arise in this channel. For the purpose of plotting, we use $J = \alpha(M^2)$. $\alpha(t)$ represents a set of leading Regge poles on the complex l -plane and is called the Reggeon. The condition $\alpha(t) < 0$ does not correspond to any physical particles because J cannot be negative [11].

Many authors [9, 13] are careful to disclaim linearity as being only approximate. For others, linearity is simply stated [14, 15]. By and large, it is believed that Regge trajectories for relativistic scattering are straight lines over a considerable range of energy without any sign of deviation [16, 17, 18]. Attempts have been made to validate this belief on computational grounds. Kahana, Maung and Norbury [19] calculated the numerical solutions of the relativistic Thompson equation which yield linear, non-intersecting and parallel Regge trajectories. Their calculation did not include the effects of spin which can be a factor in predicting the shape of the Regge trajectories. But earlier in 1985, Godfrey and Isgur [20] solved a relativized Schrödinger equation which did include the spin-spin and spin-orbit interactions. Their calculation concurred with the results of linear Regge trajectories obtained from spinless particles. These two works together seem to suggest that the effect of spin on the shape of the Regge trajectories is negligible. On the other hand, if the coupling constants are not negligible, one expects the spin-orbit contributions to be significant for high J values. Salvo [1] *et al.* published solutions for non-linear Regge trajectories by including spin dependent terms in a 3-dimension reduction of the Bethe-Salpeter equation. Salvo's conclusion differs from those of Kahana and Godfrey concerning the effect of spin on Regge trajectories.

The linearity of Regge trajectories has been the object of investigation once again recently. On the theoretical front, Tang [21] used perturbative QCD to show that Regge trajectories are non-linear by studying high-energy elastic scattering with mesonic exchange in the case of both fixed and running coupling constants. On the experimental side, Brandt [22] *et al.* affirmed the existence of non-linear Pomeron

trajectories from the data analysis of the recent UA8 and ISR experiments at CERN. They published a parameterization of Pomeron trajectories containing a quadratic term,

$$\alpha(t) = 1.10 + 0.25t + \alpha''t^2. \quad (5)$$

where α'' is a constant. Recently, Burakovsky [23, 24] presented a phenomenological string model for logarithmic and square root Regge trajectories.

In this paper, we check the claims of non-linear Regge trajectories by plotting the most recent experimental data published in the 1998 Review of Particle Physics (RPP) [25]. Our plots confirm the existence of non-linear trajectories. Early Chew-Frautschi plots also show that Regge trajectories fan out. We refer to this non-intersecting property as “divergence.” We also show that many trajectories intersect. Kahana et al. numerically constructed a set of hypothetical Regge trajectories by using a fully relativistic Thompson equation. They discovered that there are differences in the properties of the trajectories obtained by NRSE versus those by the Thompson equation. We summarize the conclusions of Kahana et al. in Table 1 to illustrate these differences.

Table 1: Comparisons of the predictions made by NRSE and the relativistic Thompson equation according to Kahana et al. [19].

“Yes” refers to a property predicted by the theory and
 “No” is the prediction of the opposite property.

	Non-relativistic Schrödinger Equation	Relativistic Thompson Equation
Linearity	No	Yes
Divergence	No	Yes
Parallelism	Yes	Yes

When trajectories of different principal quantum numbers N but all other quantum numbers fixed are plotted together, they appear parallel. We call this property “parallelism.”

2.1.2 Construction of Regge Trajectories

The starting point for constructing a meson Regge trajectory is the meson assignment table in RPP (Table 13.2 on p. 110 of Ref. [25]). We fix I and flavor by selecting particles from a single column. From this column, we isolate different trajectories by fixing N and spin-parity when we select particles with consecutive values of J . For example, the 1^1S_0 , 1^1P_1 and 1^1D_2 states constitute an $N = 1$ singlet trajectory; 1^3P_0 and 1^3D_1 the $N = 1$ first triplet; 1^3P_1 and 1^3D_2 the $N = 1$ second triplet; 1^3S_1 , 1^3P_2 , 1^3D_3 , and 1^3F_4 the $N = 1$ third triplet; 2^3S_1 and 2^3P_2 the $N = 2$ third triplet and so on. We use the experimental error instead of the width to measure the accuracy of the mass of a meson. The width measures the imaginary part of the complex energy while the experimental error indicates the accuracy of the measurement of the mass at the resonance peak. In case the mass of both the neutral and charged mesons are reported, the mass is taken to be the average of the three. For example, the mass of $\pi(138)$ is taken to be the average mass of $\pi^0(135)$ and $\pi^\pm(140)$. Similarly the error of mass is also taken to be the average of the errors of the two corresponding masses. This scheme does not pose any serious ambiguity because the masses and the errors of the neutral and charged mesons are usually quite close (the difference in mass is usually $< 1\%$ and is $\sim 3.5\%$ in the worst case) and hence do not change our conclusions. The error of mass square, dM^2 , is calculated from the mass M and its error dM by the relation $dM^2 = 2MdM$. The end results are 13 trajectories containing 2 particles each, 4 containing 3 particles each and 4 containing 4 particles each. Single particle trajectories are omitted from the plots. None of the $N = 1$ second triplet trajectories are plotted because most of them are single particle trajectories except the one containing K_{1B} and $K_2(1820)$, where K_{1B} is a nearly equal (45°) mixture of $K_1(1270)$ and $K_1(1400)$. Since some of these trajectories contained unconfirmed mesons, not all of them are used in this paper.

The bold face entries in the assignment table refer to the mesons which are confirmed by experiments. The regular typeface entries correspond to those which are omitted from the summary table because of work in progress. For example, one of the regular typeface entries in the assignment table, $f_4(2220)$, is listed as $f_J(2220)$ in the summary table because J may assume a value of either 2 or 4 depending on the final confirmation by experiments. There are other similar undetermined quantities in the meson data. This paper takes the conservative approach by using only the

bold face (confirmed) data contained in the RPP meson assignment table.

The baryon Regge trajectories are constructed from the RPP baryon assignment table (Table 13.4 on p. 112 of Ref. [25]). Baryons are categorized into 4 different confidence levels according to their likelihood of existence. Confidence level 1 is assigned to the baryons which are deemed the least likely to exist and level 4 the most likely to exist. The baryon assignment table contains only the level 3 and 4 particles. These are the baryons we will analyze in this paper.

The baryon assignment table uses a set of slightly different quantum numbers, such as J^P , (D, L_N^P) and S . As before, J is the total angular momentum, P the parity, L the orbital angular momentum and S the spin. The new quantum number D is the dimensionality of the symmetry group and has the value of either 56 or 70. These numbers come from the dimensionalities of the irreducible representations of flavor-spin $SU(6)$, i.e. $\mathbf{6} \otimes \mathbf{6} \otimes \mathbf{6} = \mathbf{56}_S \oplus \mathbf{70}_M \oplus \mathbf{70}_M \oplus \mathbf{20}_A$ where the subscript S stands for “symmetric”, A for “asymmetric” and M for “mixed symmetry.” N is the “band” which gives the number of excitation quanta. The construction of a baryon Regge trajectory is similar to that of the meson in that all quantum numbers except J are fixed along a trajectory. In other words, D , S , flavor, strangeness and isospin are constant along a baryon Regge trajectory. Only L is allowed to vary. N changes with L in the same integer steps so that a change in N is the same as a change in L . Hence we can ignore the consideration of N .

Regge recurrences are separated by 2 units of J . In the case of mesons, we can plot two trajectories together in some cases because the cross channel forces between them vanish. It is known as the “exchange degeneracy” (EXD) [13] which arises out of the cross channel forces which split $a(l, k)$ into even (+) and odd (−) signatures as $a_{\pm}(l, k)$. The separation of the even and odd signatures correspond to the two different Regge trajectories. If the cross channel forces vanish (as in the case of mesons), the even and odd signatures coincide and the even and odd trajectories overlap. It means $\alpha_+ = \alpha_-$ and $\beta_+ = \beta_-$. These are called the EXD conditions. When the EXD conditions apply, the even and odd parity mesons can be plotted along the same trajectories. In the case of baryons, the cross channel forces persist. Therefore the even and odd parity baryons cannot be plotted together in the same trajectories. The EXD criteria enable us to pick out 3 trajectories of 3 baryons each and 2 trajectories of 2 baryons each from the baryon assignment table. These selections are achieved by isolating

a column (e.g. the $N(939)$ – $N(2220)$ column) and picking all the particles with the same D , S and P (e.g. $N(939)$, $N(1680)$ and $N(2220)$). Once a trajectory is picked from the first column, corresponding entries of the following columns also constitute baryon Regge trajectories. The spectroscopic notation for baryons is $L_{2I,2J}$. The N and Λ trajectories are made up of the P_{11} , F_{15} , H_{19} states and the Δ trajectory is made up of the P_{33} , F_{37} , H_{311} states.

2.2 Linearity

Linearity means that all the particles of a Regge trajectory must lie on the straight line $M^2 = \alpha J + \beta$. In graphical analysis, non-linearity can be detected by simple inspection in only extreme cases. Linearity on the other hand is more difficult to judge. Therefore we devise a method called the “zone test” to facilitate this judgment.

2.2.1 Zone Test

We test linearity by the “zone test” on Regge trajectories with 3 or more particles. A test zone of an experimental Regge trajectory is defined to be the area bounded by the error bars of the first and the last particles and the straight lines joining them. Figs. 1–6 illustrate these test zones (regions enclosed by the dotted lines). A zone contains all the possible straight lines crossing the error bars of the first and the last particles. A Regge trajectory can be a straight line if the error bars of all other particles intersect the zone. In most cases, intersections are easily discernible by inspection. If ambiguity ever arises in borderline cases, an exact numerical version of the zone test is used.

Suppose we are given a sequence of N mesons and their values of mass square with errors, $\{M_i^2 \pm dM_i^2\}$. We calculate the equation of the straight line connecting $M_1^2 + dM_1^2$ and $M_N^2 + dM_N^2$ and then the equation of the line connecting $M_1^2 - dM_1^2$ and $M_N^2 - dM_N^2$. These two lines define the boundaries of the zone. For each J , we can calculate the bounds to be intersected by the error bar to qualify as a linear Regge trajectory. For a 3-particle trajectory in which the particles are labelled (1, 2, 3), the lower and upper bounds at $J = 2$ are calculated as

$$lb(3, 2) = \frac{(M_1^2 - dM_1^2) + (M_3^2 - dM_3^2)}{2},$$

$$ub(3, 2) = \frac{(M_1^2 + dM_1^2) + (M_3^2 + dM_3^2)}{2}, \quad (6)$$

where $lb(3, 2)$ stands for the lower bound and $ub(3, 2)$ the upper bound of particle 2 along a 3-particle trajectory. Similarly, we can calculate the bounds of particles 2 and 3 along a 4-particle trajectory as

$$lb(4, 2) = \frac{2(M_1^2 - dM_1^2) + (M_4^2 - dM_4^2)}{3},$$

$$ub(4, 2) = \frac{2(M_1^2 + dM_1^2) + (M_4^2 + dM_4^2)}{3}. \quad (7)$$

$$lb(4, 3) = \frac{(M_1^2 - dM_1^2) + 2(M_4^2 - dM_4^2)}{3},$$

$$ub(4, 3) = \frac{(M_1^2 + dM_1^2) + 2(M_4^2 + dM_4^2)}{3}. \quad (8)$$

We can generalize these results for particle i along an n -particle trajectory as

$$lb(N, i) = \frac{(N - i)(M_1^2 - dM_1^2) + (i - 1)(M_N^2 - dM_N^2)}{N - 1},$$

$$ub(N, i) = \frac{(N - i)(M_1^2 + dM_1^2) + (i - 1)(M_N^2 + dM_N^2)}{N - 1}. \quad (9)$$

This numerical method is useful for checking linearity when simple inspection is inconclusive.

2.2.2 Conclusions from Zone Test

All of the data points in all of the graphs in this paper are shown with error bars. If the error bars are invisible in the plots, it simply means that the error bars are smaller than the symbols of the associated data points. We use the zone test to check linearity by simple inspection in Figs. 1–6. At least one of the error bars of the intermediate particles fails to intersect the test zone in all of the figures except Fig. 3.

Figs. 1–2 illustrate a group of meson Regge trajectories of the $N = 1$, $S = 0$ singlet states and varying J corresponding to the 1^1S_0 , 1^1P_1 and 1^1D_2 states. Both trajectories fail the zone test and are non-linear. The π trajectory has a decreasing slope.

In Figs. 3–6, trajectories of the $N = 1$, $S = 1$ third triplet states with varying J corresponding to the 1^3S_1 , 1^3P_2 , 1^3D_3 , and 1^3F_4 states are plotted. Trajectories in Figs. 4 and 6 fail the zone test by simple inspection. In Fig. 3, the error bars of both $a_2(1320)$ and $\rho_3(1690)$ appear to intersect the zone at the lower boundary. In this case, the numerical version of the zone test is used. The error bars of both particles must intersect the bounds to support linearity. The bounds in the case of $a_2(1320)$ are $(lb, ub)(4, 2) = (1.73, 1.78) \text{ GeV}^2$ which intersect the error bar, $(1.7358, 1.7390) \text{ GeV}^2$. The bounds for $\rho_3(1690)$ are $(lb, ub)(4, 3) = (2.87, 2.96) \text{ GeV}^2$ which also intersect the error bar, $(2.843, 2.876) \text{ GeV}^2$. The numerical test supports the existence of a straight line intersecting all the error bars of the particles along this trajectory. The ω trajectory has an increasing slope while both the ϕ and K^* trajectories have decreasing slopes.

The zone test for baryon trajectories are illustrated in Figs. 7–9. The N and Δ trajectories in Figs. 7 and 9 clearly satisfy the zone test by simple inspection. The Λ trajectory in Fig. 8 is shown to be non-linear by the numerical zone test. In summary, 6 of 8 trajectories with 3 or more particles each are shown to be non-linear. Polynomial fits of the trajectories are included in the figure captions for reference only.

2.3 Divergence

Divergence seems to be a property of the Regge trajectories in the early Chew-Frautschi plots and is also a prediction of the numerical calculations by Kahana et al [19]. Divergence is defined to be the conjunction of two properties: (1) non-intersection and (2) fanning out.

We check divergence by plotting families of meson Regge trajectories with the same isospin and spin-parity in Figs. 10–15. It is observed that non-linear trajectories of similar masses intertwine. In general, Regge trajectories are not evenly separated in a graph. Some trajectories can be obscured when many of them are plotted over a large mass range on the same graph. We adopt a numeration scheme which allows us to identify the obscured trajectories in separate plots. For example, the group denoted as 1–3 in Fig. 11 is magnified as trajectories 1–3 in Fig. 12. Divergence is clearly violated in Fig. 14 when trajectories intersect. Due to the large error bars,

divergence in Fig. 12, the determination of the properties of these meson trajectories is inconclusive.

Although individual meson trajectories do not fan out, it can be seen in Figs. 10, 11, 13 and 15 that groups of them diverge on a global level. We also notice that these groups can be labelled according to mass difference. In general, the mass of the intersecting trajectories does not differ significantly. On the other hand, divergent trajectories have large mass difference. For example, in Fig. 10, the π , K and η trajectories have small mass difference and form a group of intersecting trajectories. The D and D_S trajectories also form a group with small mass difference. These two groups of trajectories diverge globally. In summary, trajectories of small mass difference do not diverge but those of large mass difference fan out in our plots. In the case of baryon Regge trajectories, there are insufficient data to test divergence. Divergence is shown to be plausible in Figs. 16 and 17.

2.4 Parallelism

Parallelism refers to the property that Regge trajectories of different values of N (which are otherwise identical) are parallel. Two trajectories are parallel if the dynamics are similar. There is no *a priori* reason why parallelism must hold. There are only two ϕ trajectories with $N = 1$ and $N = 2$ which qualify for this test. Fig. 18 shows that the two trajectories appear to be parallel. However these trajectories consist of only 2 or 3 mesons each. It is not clear how they will behave at $J > 2$. The error of $f_2(2010)$ is also quite large compared to the separation of the two trajectories. In conclusion, the status of parallelism as a candidate for a property of Regge trajectories is still uncertain.

2.5 Summary

The linearity of Regge trajectories is clearly violated in Figs. 1, 2, 4 and 6 by simple inspection but is supported by the numerical zone test in Fig. 3. Divergence is not observed on an individual basis. On the other hand, divergence of groups of trajectories of small mass difference is observed on a global level. Due to insufficient data, parallelism is inconclusive.

Currently there are a variety of models predicting both linear and non-linear Regge trajectories. In general, almost all theories [1, 2, 24, 26, 27, 29, 30] agree that meson Regge trajectories are linear in the small J limit. Our plots contradict these predictions. Secondly, all non-linear Regge trajectories models predict trajectories with either increasing or decreasing slopes exclusively, but not both [1, 24, 28]. Our plots show that meson Regge trajectories of both kinds exist. Therefore data rule out all the models that predict non-linear meson Regge trajectories with strictly increasing or decreasing slopes. In the end, data rule out all current meson Regge trajectories models because they are faced with at least one of the problems mentioned above.

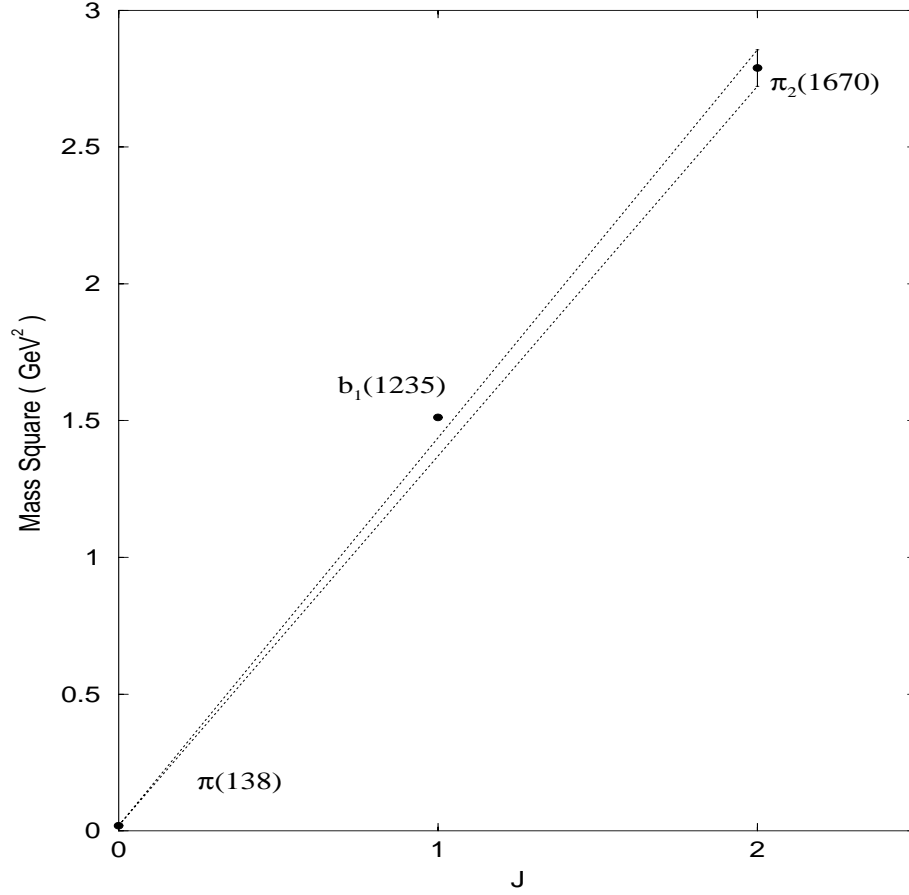


Figure 1: Meson Regge trajectory of the $N = 1, S = 0$ singlet states. $b_1(1235)$ fails to intersect the zone. The polynomial fit is $M^2 = -0.1077J^2 + 1.6003J + 0.019$ (GeV²). The mass of $\pi(138)$ is taken to be the average of the masses of $\pi^0(135)$ and $\pi^\pm(140)$. Although there is a 6.5 % difference between the mass squares of $\pi^0(135)$ and $\pi^\pm(140)$, the test zone is virtually unchanged by this small difference because of the large mass squared of the other two mesons on the trajectory. The zone test suggests that the π trajectory is non-linear.

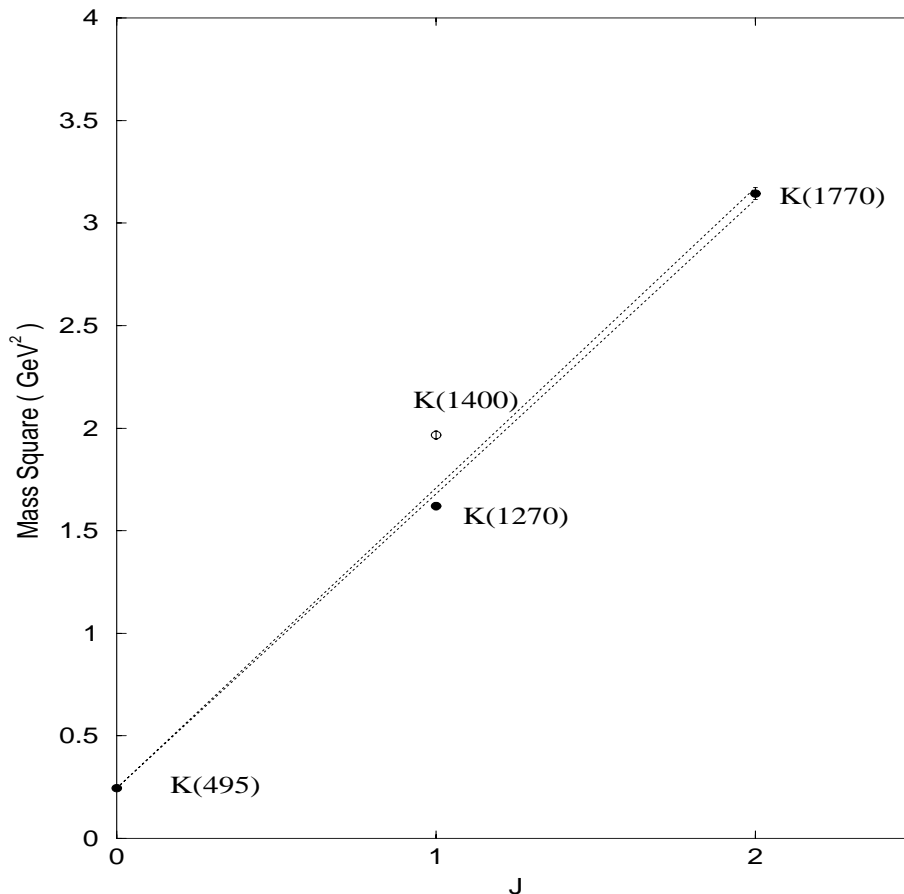


Figure 2: Meson Regge trajectory of the $N = 1$, $S = 0$ singlet states. The RPP assignment table lists K_{1B} as a nearly equal mixture of $K(1270)$ and $K(1400)$. In the graph above, we plot both constituent mesons at $J = 1$ for the sake of completeness. Neither $K(1270)$, $K(1400)$ nor their average satisfies the zone test by simple inspection. The polynomial fit of $K(495)$, $K(1270)$ and $K(1770)$ is $M^2 = 0.0737J^2 + 1.3018J + 0.245$ (GeV²).

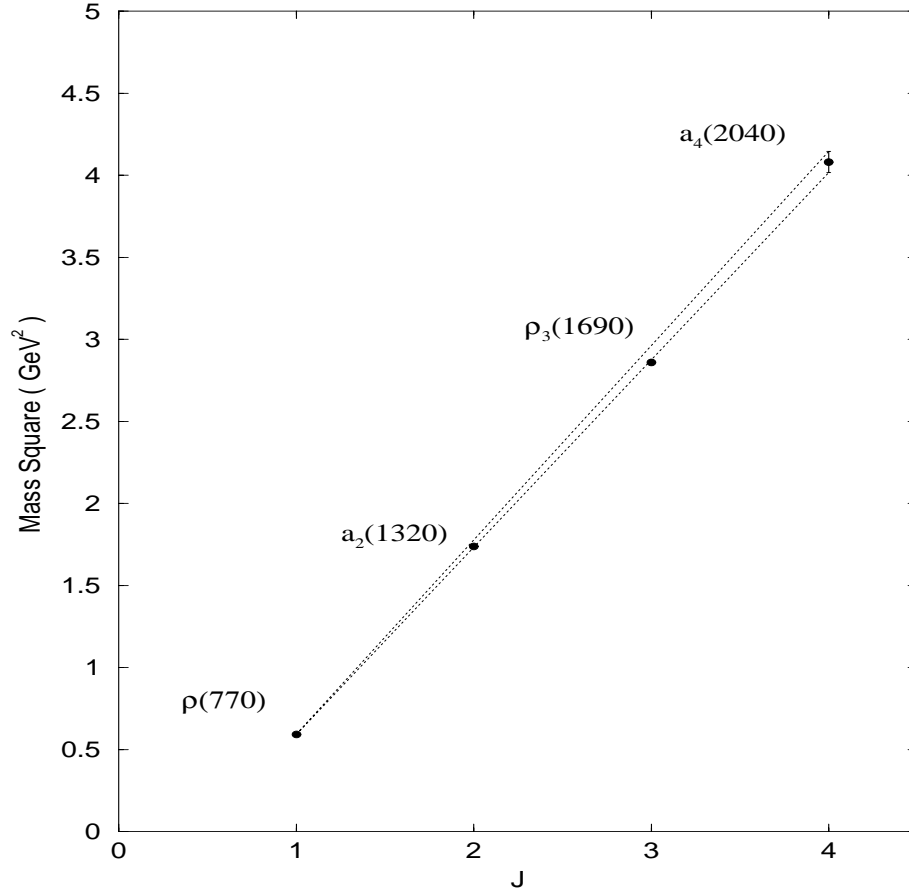


Figure 3: Meson Regge trajectory of the $N = 1$, $S = 1$ third triplet states. Both $a_2(1320)$ and $\rho_3(1690)$ intersect the zone and hence this trajectory passes the zone test. Linearity is supported by the numerical zone test. The polynomial fit is $M^2 = 0.0191J^2 + 1.0629J - 0.4831$ (GeV²). The negative vertical intercept corresponds to a non-sense pole because $J < 1$ is not allowed in an $S = 1$ state.

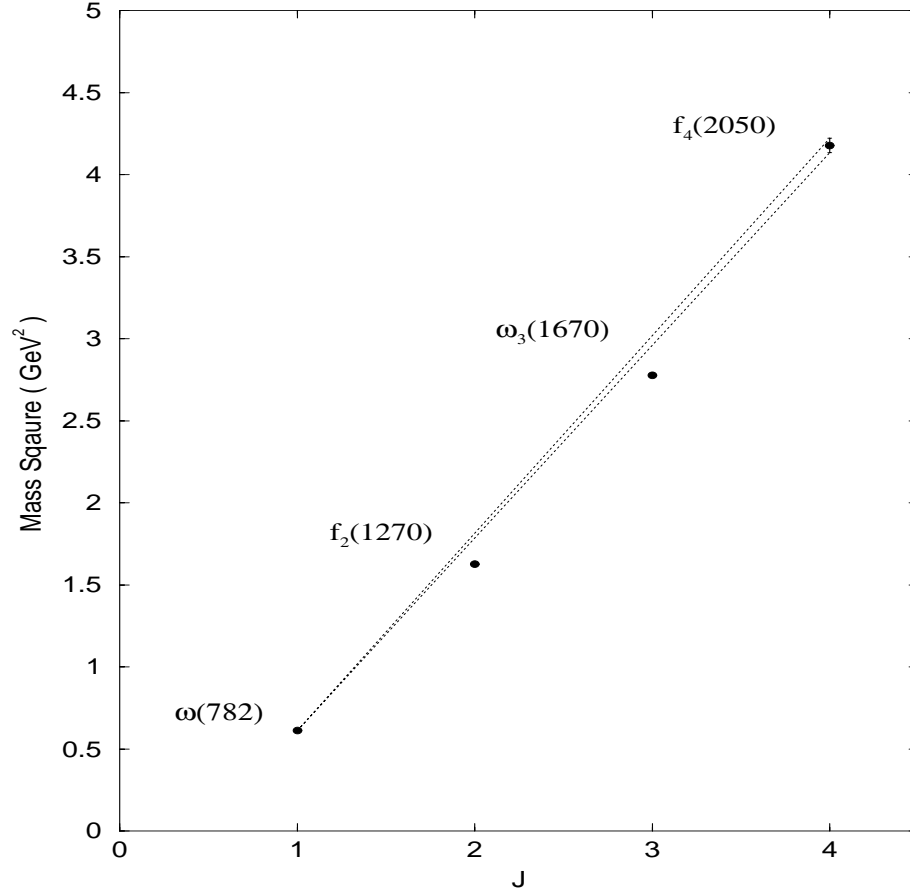


Figure 4: Meson Regge trajectory of the $N = 1$, $S = 1$ third triplet states. Both $f_2(1270)$ and $\omega_3(1670)$ fail to intersect the zone. The polynomial fit is $M^2 = 0.0962J^2 + 0.7042J - 0.1837 (\text{GeV}^2)$.

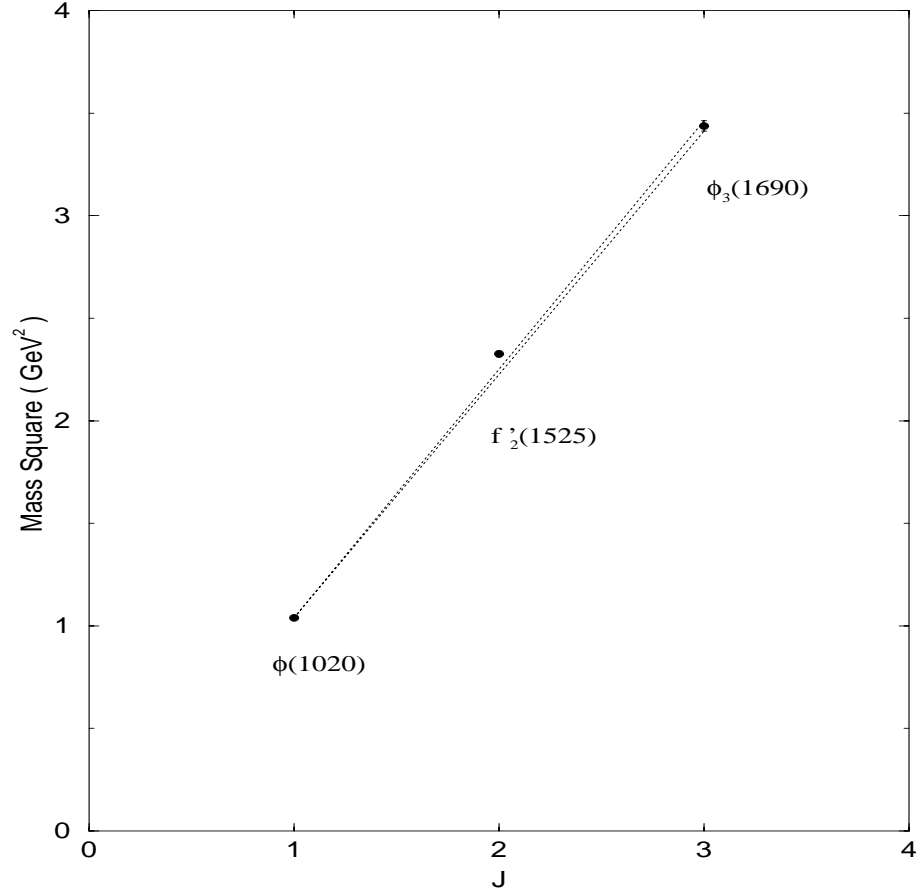


Figure 5: Meson Regge trajectory of the $N = 1$, $S = 1$ third triplet states. $f'_2(1525)$ fails to intersect the zone. The polynomial fit is $M^2 = -0.0879J^2 + 1.5505J - 0.4234 (\text{GeV}^2)$.

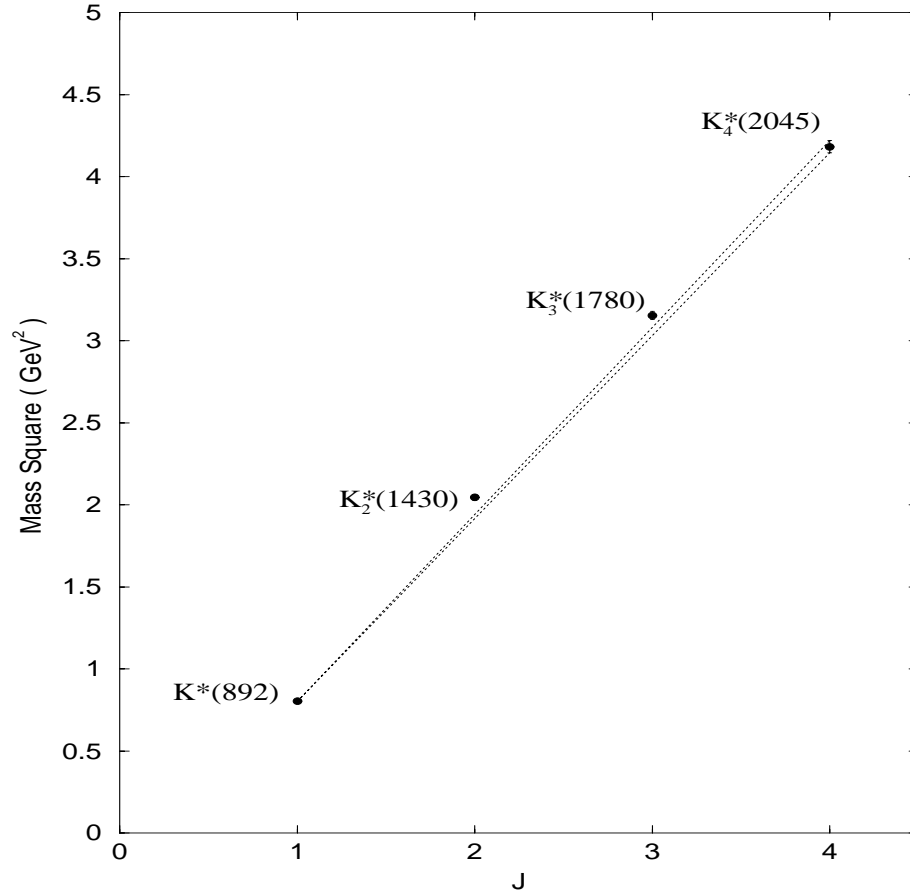


Figure 6: Meson Regge trajectory of the $N = 1$, $S = 1$ third triplet states. Both $K_2^*(1430)$ and $K_3^*(1780)$ fail to intersect the zone. The polynomial fit is $M^2 = -0.0535J^2 + 1.3922J - 0.5331$ (GeV²).

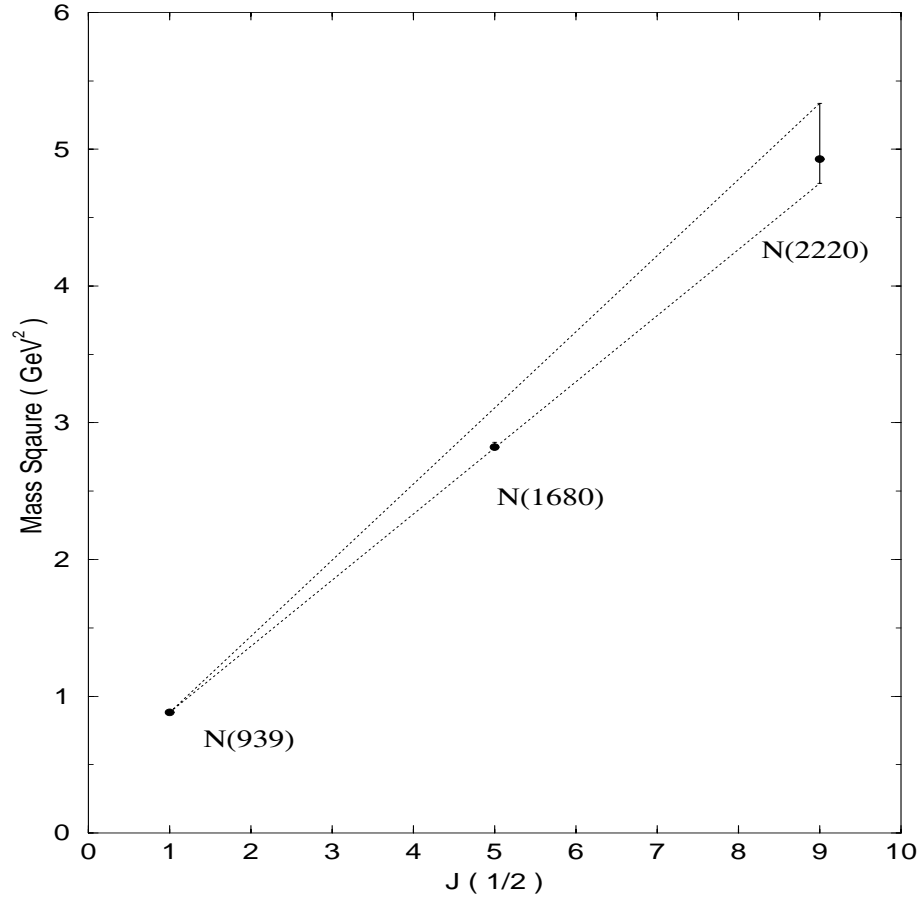


Figure 7: Baryon Regge trajectory of $S = 1/2$, $P = +$ and $I = 1/2$ octet states. $N(1680)$ satisfies the zone test by simple inspection. The polynomial fit is $M^2 = 0.0207J^2 + 0.9081J + 0.4223$ (GeV).

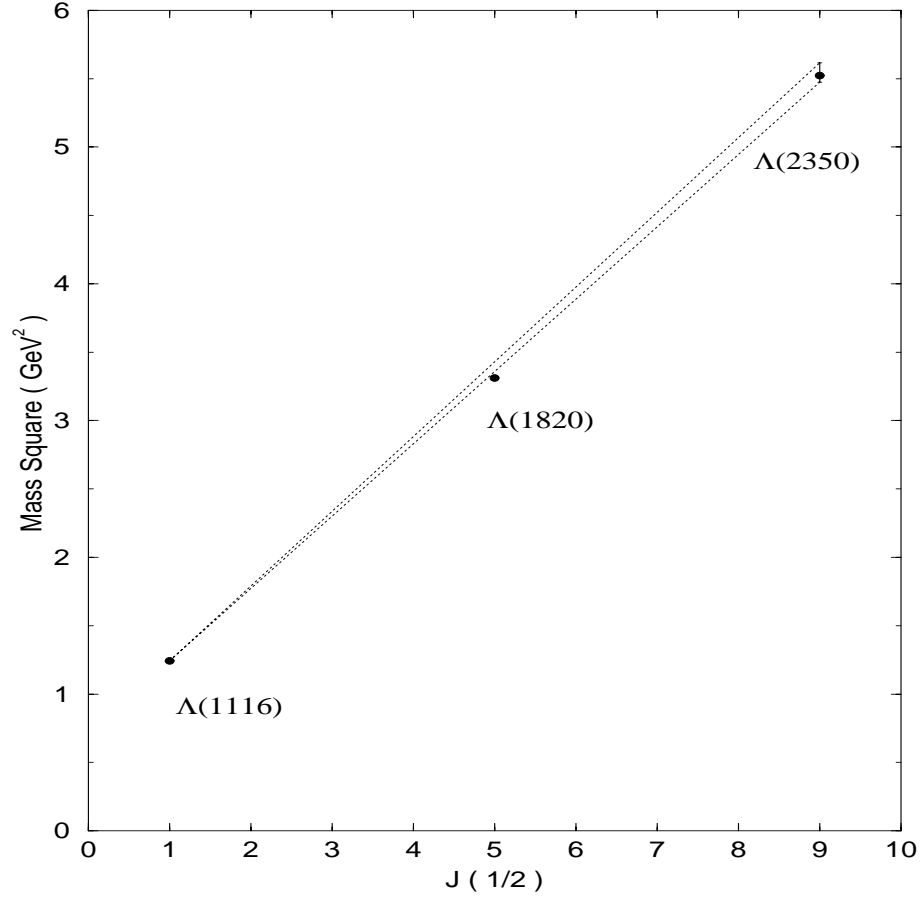


Figure 8: Baryon Regge trajectory of $S = 1/2$, $P = +$ and $I = 0$ octet states. $\Lambda(1820)$ has a bound of $(lb, ub)(3, 2) = (3.360, 3.431) \text{ GeV}^2$ which does not intersect the experimental bound of $(3.294, 3.331) \text{ GeV}^2$. $\Lambda(1820)$ fails the numerical zone test. The polynomial fit is $M^2 = 0.0180J^2 + 0.9797J + 0.7524 \text{ (GeV)}$.

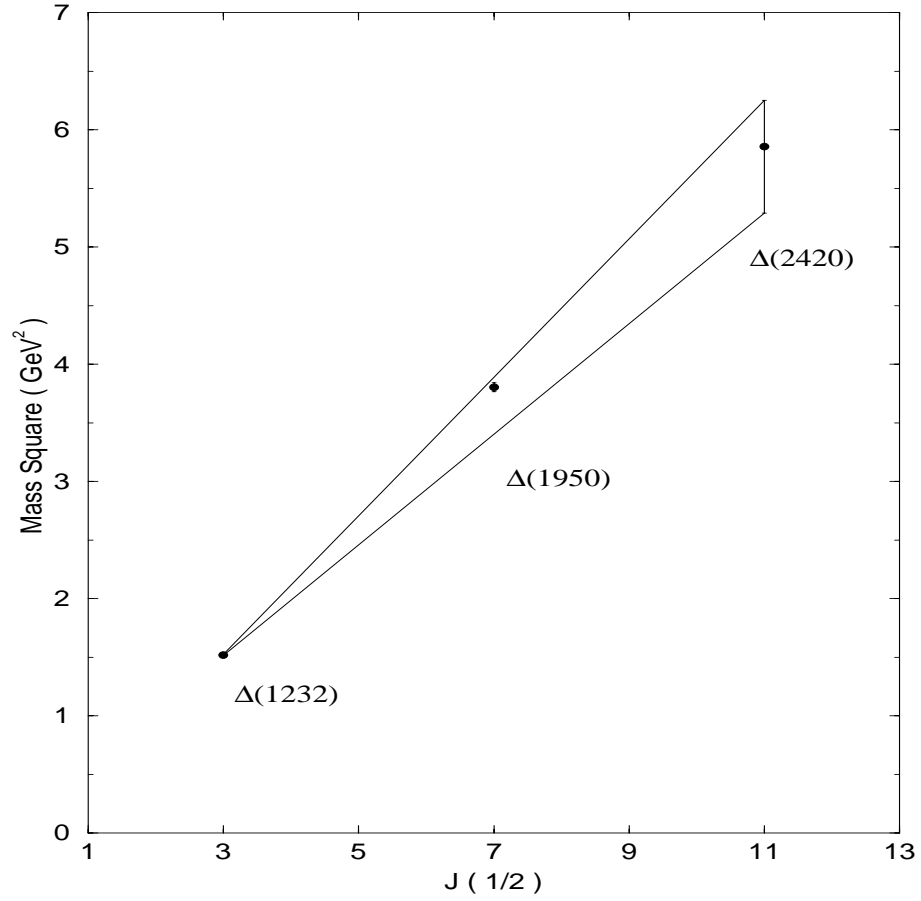


Figure 9: Baryon Regge trajectory of $S = 3/2$, $P = +$ and $I = 3/2$ decuplet states. $\Delta(1950)$ satisfies the zone test due to the large error of $\Delta(2420)$. The polynomial fit is $M^2 = -0.029J^2 + 1.2875J - 0.3480$ (GeV).

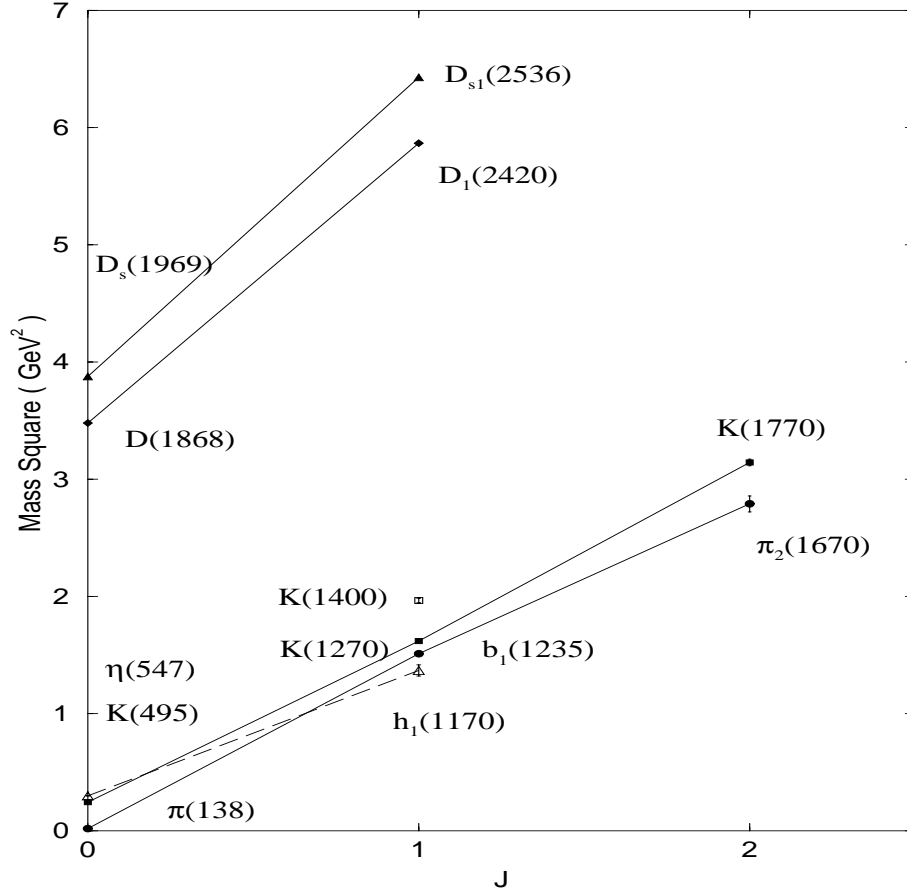


Figure 10: Meson Regge trajectories of the $N = 1$, $S = 0$ singlet states. The series consists of the 1^1S_0 , 1^1P_1 and 1^1D_2 states. The trajectories include those illustrated in Figs. 1 and 2 as well as the D mesons. The D and D_s mesons form a group and the K and light unflavored mesons η and π form another. Global divergence is observed among groups of trajectories of large mass difference but local divergence is violated when the η trajectory (denoted by the dotted line) intersects the K and π trajectories.

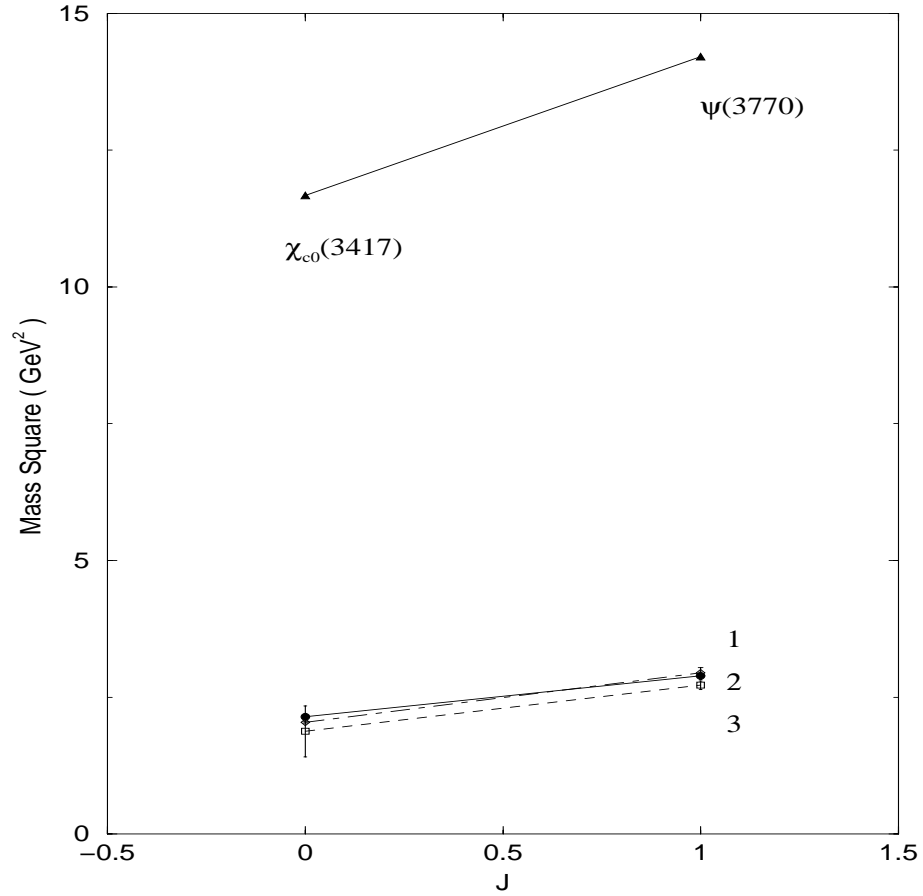


Figure 11: Meson Regge trajectories of the $N = 1$, $S = 1$ first triplet states. The series consists of the 1^3P_0 and 1^3D_1 states. The trajectories labelled 1–3 are magnified in Fig. 12. Global divergence is observed here.

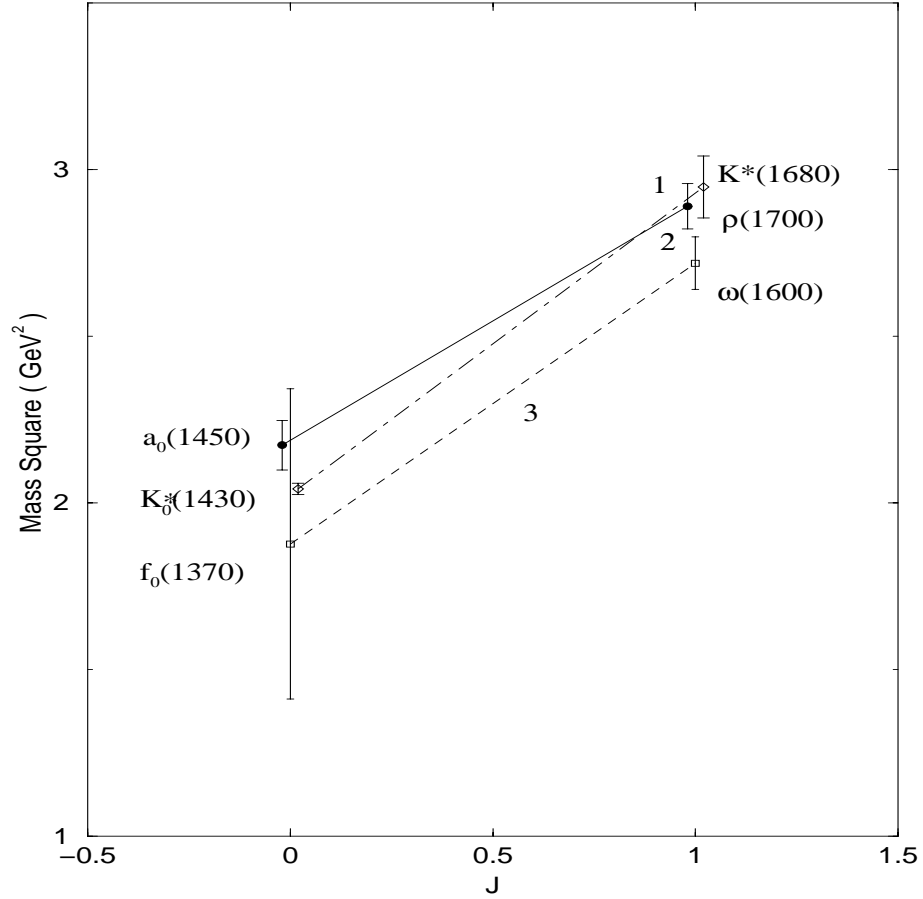


Figure 12: Meson Regge trajectories of the $N = 1$, $S = 1$ first triplet states. The series consists of the 1^3P_0 and 1^3D_1 states. The trajectories 1–3 are the magnifications of a subset of Fig. 11. Trajectories 1 and 2 are shifted horizontally slightly to separate the error bars. Divergence is inconclusive because of the large error bars. The actual mass of $K^*(1680)$ is 1717 MeV which causes it to appear higher than $\rho(1700)$ in the graph.

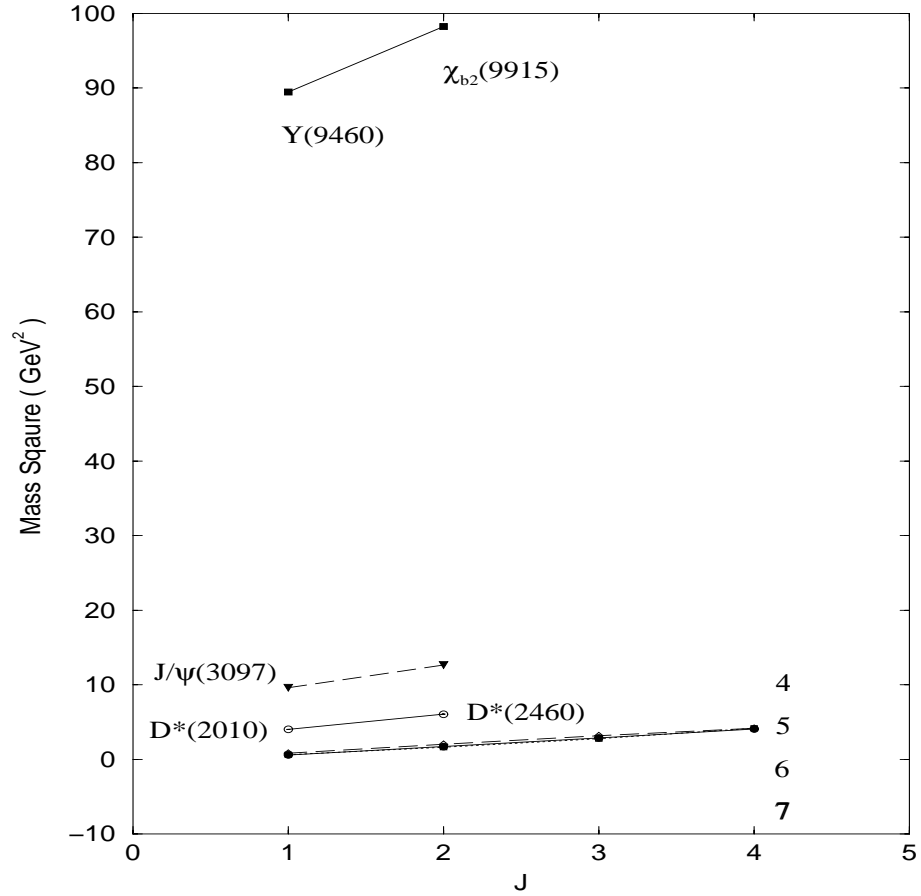


Figure 13: Meson Regge trajectories of the $N = 1$, $S = 1$ third triplet states. The series consists of the 1^3S_1 , 1^3P_2 , 1^3D_3 , and 1^3F_4 states. The group of trajectories labelled 4–7 are magnified in Fig. 14. Global divergence is observed.

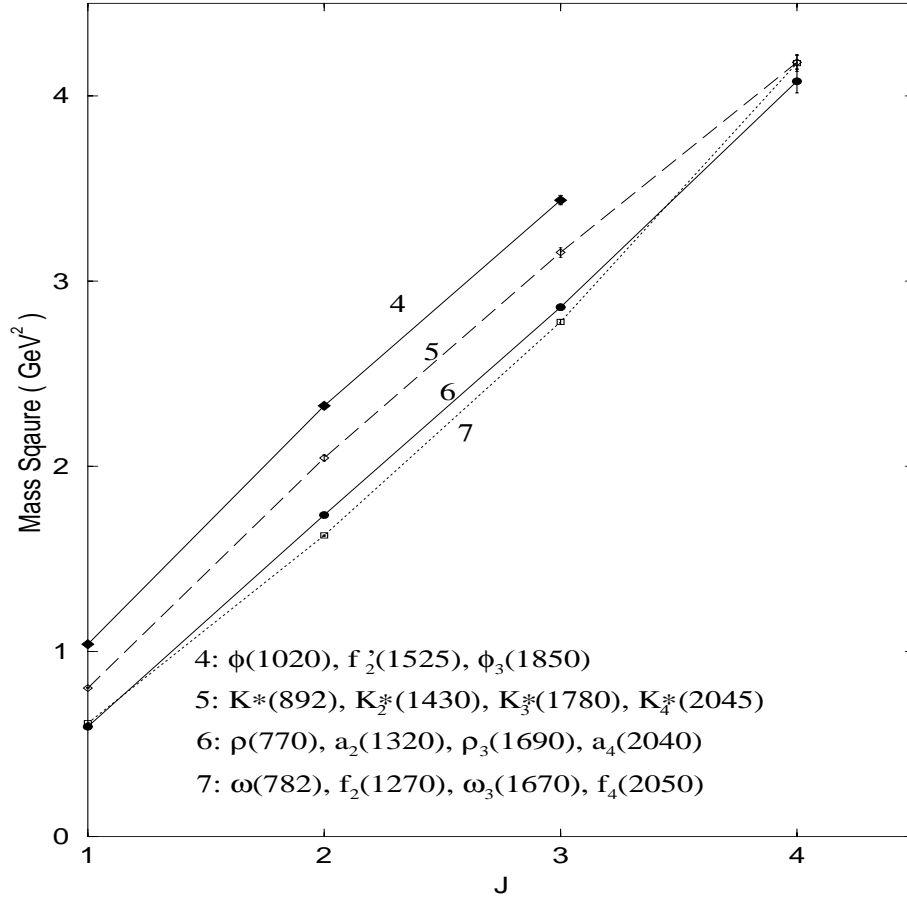


Figure 14: Meson Regge trajectories of the $N = 1$, $S = 1$ third triplet states. The series consists of the 1^3S_1 , 1^3P_2 , 1^3D_3 , and 1^3F_4 states. The trajectories 4–7 are magnifications of a subset of the trajectories in Fig. 13 and are the same trajectories as in Figs. 3–6. Divergence is violated by these trajectories.

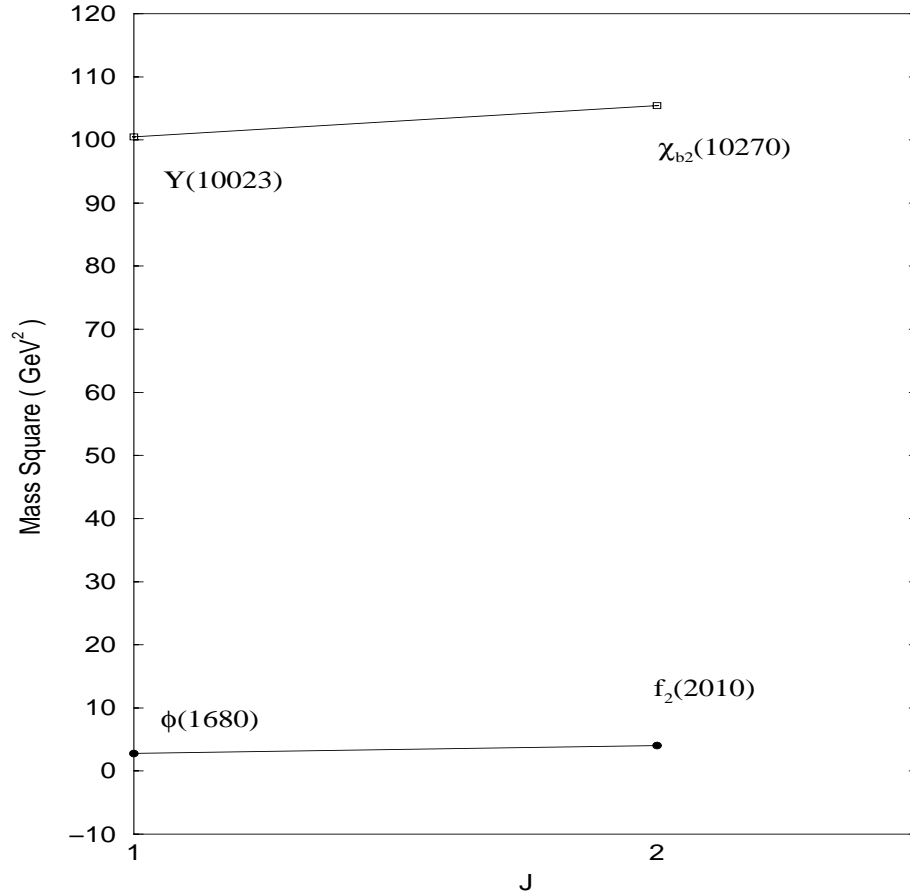


Figure 15: Meson Regge trajectories of the $N = 2$, $S = 1$ third triplet states. The series consists of the 2^3S_1 and 2^3P_2 states. Divergence is observed.

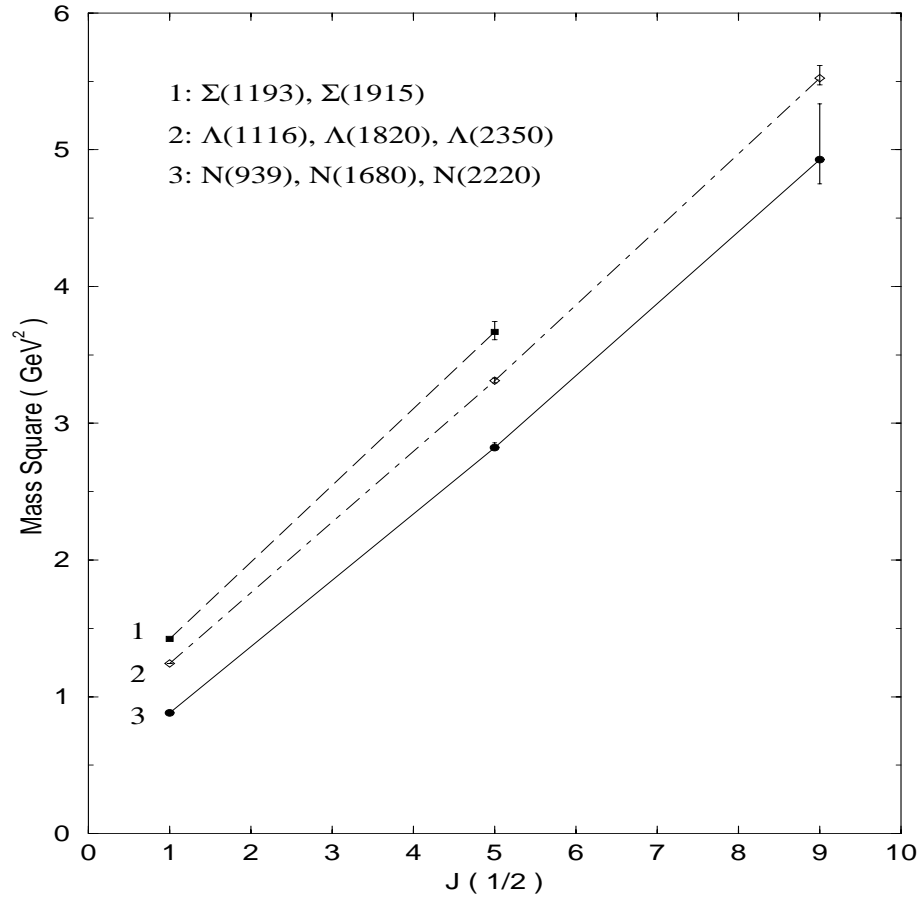


Figure 16: Baryon Regge trajectories of $P = +$ octet states. Due to the scarcity of data and the large error of $N(2220)$, divergence is plausible but inconclusive.

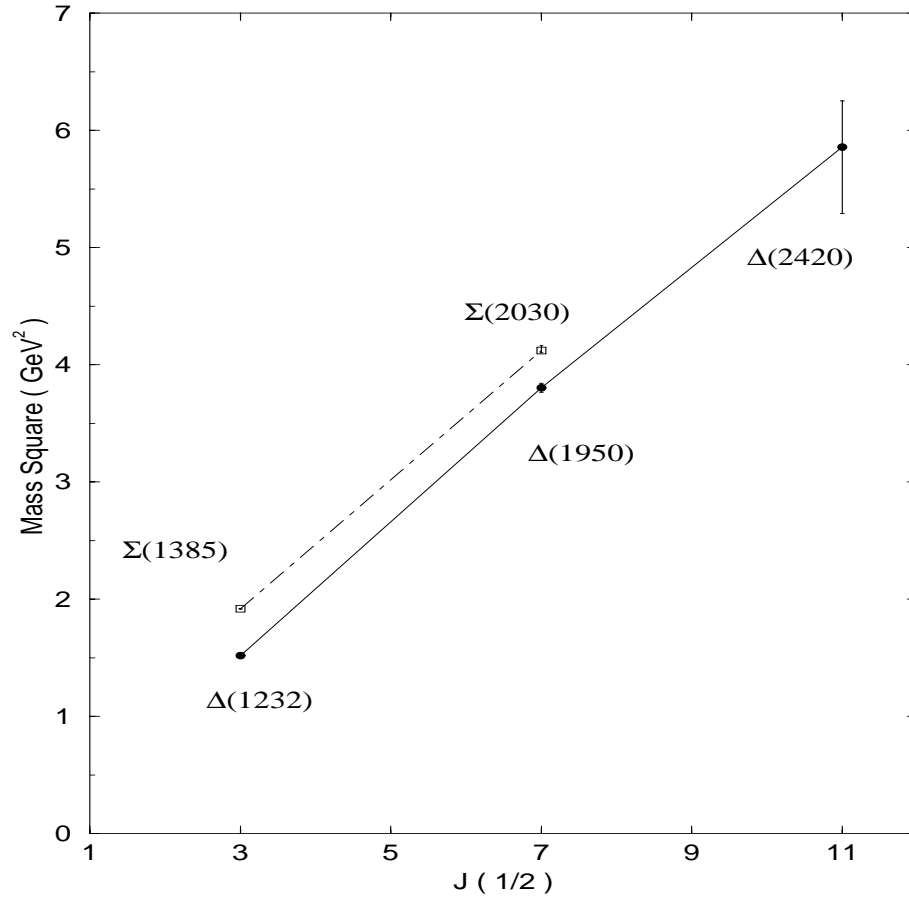


Figure 17: Baryon Regge trajectories of $P = +$ decuplet states. Due to the scarcity of data and the large error of $\Delta(2420)$, divergence is plausible but inconclusive.

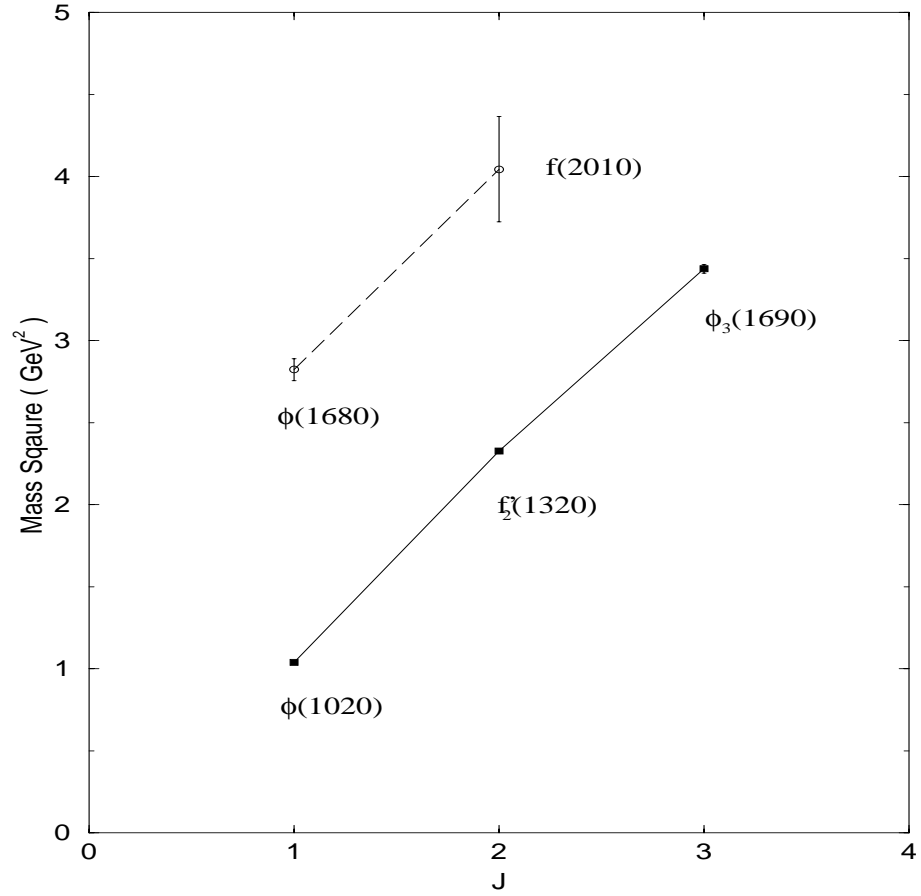


Figure 18: Meson Regge trajectories of the $N = 1, 2, S = 1$ third triplet states. The series consists of the $1^3S_1, 1^3P_2, 2^3S_1$ and 2^3P_2 states. The $N = 1$ states are denoted by solid lines and $N = 2$ states by long-dashed lines. Parallelism is inconclusive due to the large error bar of $f(2010)$.

Chapter 3

Nystrom Plus Correction Method

A new method is presented for solving the momentum-space Schrödinger equation with a linear potential. The Lande-subtracted momentum space integral equation can be transformed into a matrix equation by the Nystrom method. The method produces only approximate eigenvalues in the cases of singular potentials such as the linear potential. The eigenvalues generated by the Nystrom method can be improved by calculating the numerical errors and adding the appropriate corrections. The end results are more accurate eigenvalues than those generated by the basis function method. The method is also shown to work for a relativistic equation such as the Thompson equation.

The momentum space Schrödinger equation has a singular kernel for the Coulomb and linear potentials. The Coulomb singularity is removed with the Lande subtraction method [31, 32]. Previous work [33, 34, 35] showed how to remove the singularity from the linear potential using a subtraction method with basis functions. A problem with this method is that one must guess a suitable set of basis functions in advance. In this paper, we show that Nystrom method [37] can solve the same problem more simply and accurately. We begin with a review of the basis function method. Then we introduce the Nystrom method and apply it to the s-state momentum space Schrödinger equation with a linear potential. We use our new numerical results to show that the Nystrom plus correction method is more accurate than the basis function method. At the end, we generalize the Nystrom method to higher angular momentum quantum

numbers ($l > 0$).

3.1 The Basis Function Method

We begin this paper with a discussion of the basis function method to give the proper theoretical motivation. We shall use the simplest momentum space Schrödinger equation to illustrate the principles of the numerical methods, which is the s-state equation.

The momentum space Schrödinger equation is related to an integral equation of the Fredholm type

$$\int K(p, p') \phi(p') dp' = \lambda \phi(p). \quad (10)$$

Suppose that the wavefunction ϕ can be expanded in a set of basis functions $\{g_i\}$, such that

$$\phi(p) = \sum_{i=1}^N C_i g_i(p), \quad (11)$$

where C_i are constant coefficients. Substitute Eq. [11] into Eq. [10] to obtain

$$\sum_{i=1}^N \int K(p, p') C_i g_i(p') dp' = \lambda \sum_{i=1}^N C_i g_i(p). \quad (12)$$

Now multiply both sides of Eq. [12] with $g_j(p)$ and integrate over p to symmetrize the equation over i and j ,

$$\sum_{i=1}^N C_i \underbrace{\int \int K(p, p') g_i(p') g_j(p) dp' dp}_{A_{ij}} = \lambda \sum_{i=1}^N C_i \underbrace{\int g_i(p) g_j(p) dp}_{B_{ij}}, \quad (13)$$

and the result is a matrix equation,

$$\sum_{i=1}^N A_{ij} C_i = \lambda \sum_{i=1}^N B_{ij} C_i, \quad (14)$$

where C_i is the eigenvector and λ the eigenvalue. The indices i and j correspond to the quadrature points p and p' . N represents the number of mesh points. In the case of the momentum space Schrödinger equation with a Coulomb or linear potential, the

kernel \mathbf{A} is singular. A simple example is the momentum space Schrödinger equation with a linear potential in the S -state [33, 35],

$$\frac{p^2}{2\mu} \phi_{n0}(p) + \frac{\lambda_L}{\pi p^2} \int_0^\infty \underbrace{\left[\frac{\eta^2}{p'p} Q_0''(y) + Q_0'(y) \right]}_{V_0^L(p,p')} \phi_{n0}(p') dp' = E_{n0} \phi_{n0}(p), \quad (15)$$

where $y = (p^2 + p'^2)/2p'p$,

$$Q_0'(y) = p'p \left[\frac{1}{(p+p')^2 + \eta^2} - \frac{1}{(p-p')^2 + \eta^2} \right], \quad (16)$$

and

$$\frac{\eta^2}{p'p} Q_0''(y) = \eta^2 (p^2 + p'^2 + \eta^2) \left[\frac{1}{(p+p')^2 + \eta^2} - \frac{1}{(p-p')^2 + \eta^2} \right]^2. \quad (17)$$

Lande subtraction [33, 35, 36] involves subtracting a zero term

$$\int_0^\infty \left[\frac{\eta^2}{p'p} Q_0''(y) + Q_0'(y) \right] dp' = 0 \quad (18)$$

from Eq. [15] such that

$$\frac{p^2}{2\mu} \phi_{n0}(p) + \frac{\lambda_L}{\pi p^2} \int_0^\infty \left[\frac{\eta^2}{p'p} Q_0''(y) + Q_0'(y) \right] [\phi_{n0}(p') - \phi_{n0}(p)] dp' = E_{n0} \phi_{n0}(p). \quad (19)$$

Using Eqs. [16,17], the integral in Eq. [19] for $p > 0$ in the limit of $y \rightarrow 1$ can be shown to equal

$$\lim_{\eta \rightarrow 0} \lim_{p \rightarrow p'} \frac{\lambda_L}{\pi} \left[2\eta^2 \left(\frac{1}{(p-p')^2 + \eta^2} \right)^2 - \frac{1}{(p-p')^2 + \eta^2} \right] (p-p')^2 \frac{d\phi_{n0}}{dp} = 0. \quad (20)$$

The order of the limits in Eq. [20] is important. The reverse order will lead to the nonsensical result $\int Q_0'(y) dp' = 0$. Next, in the limit of $p, p' \rightarrow 0$, $(p+p')^2 = (p-p')^2$. By substituting this equality into Eqs. [16,17], it can be shown again that the integral in Eq. [19] vanishes for $p \rightarrow 0$ at $y = 1$. At the end, the integral vanishes at $y = 1$, $\forall p$. Away from the singularities, both integrands in the integral of Eq. [19] are finite. By taking $\eta \rightarrow 0$, the first integrand vanishes. The final form of Eq. [19] is

$$\frac{p^2}{2\mu} \phi_{n0}(p) + \frac{\lambda_L}{\pi p^2} \int_0^\infty Q_0'(y) [\phi_{n0}(p') - \phi_{n0}(p)] dp' = E_{n0} \phi_{n0}(p), \quad (21)$$

where $Q'_0(y) = 1/(1 - y^2)$. As mentioned before, ϕ is expanded in basis functions, followed by integrating Eq. [21] over p to generate a matrix equation. The basis functions used in previous publications [33, 35] are

$$g_i^A(p) = \exp\left[\frac{-p^2 i^2}{M}\right] \quad (22)$$

and

$$g_i^B(p) = \frac{1}{(i/M)^2 + p^4} \quad (23)$$

respectively, where M is the maximum number of basis functions used. M has a maximum because the code crashes when too many basis functions are used. The basis functions $g_i^A(p)$ and $g_i^B(p)$ have $M = 18$.

The singularity of the kernel is a major challenge in solving the integral equation with a linear potential. It was shown [33] that a simple pole remains even after subtraction. The role of the basis functions is to make possible the evaluation of the Cauchy principal value of the subtracted integral using the Sloan method [38]. To illustrate the Sloan method, we suppose that $f(x)$ has a simple pole such that

$$f(x) = \frac{g(x)}{x} \quad (24)$$

where $g(x)$ is regular. The Cauchy principal value of the subtracted integral of $f(x)$ can be evaluated if the range of integration is symmetric. For example, the numerical integration of

$$\int_{-1}^1 \frac{g(x) - g(0)}{x} dx \quad (25)$$

yields the Cauchy principal value because the point $x = 0$ is skipped when quadrature points are generated in the symmetric interval $(-1, 1)$. The subtraction term has zero contribution since

$$\int_{-1}^1 \frac{1}{x} dx = 0. \quad (26)$$

The purpose of this term is to justify the existence of the Cauchy principle value and to reduce numerical errors. In order to apply the Sloan method to Eq. [21], the integration variable is transformed from p to x such that x is centered at zero and its range is symmetric.

In the case of the Coulomb potential, the kernel has a logarithmic singularity,

$$Q_0(y) = \frac{1}{2} \ln \left| \frac{y+1}{y-1} \right|, \quad (27)$$

which is completely removed by Lande subtraction [31, 33] because no simple pole remains after the subtraction.

The key to the success of the basis function method is the availability of a suitable set of basis functions for a particular problem. Unfortunately there is no *a priori* reason why the same set of basis functions will work in every situation. For this reason, it may be advantageous to have a method (such as the Nystrom method) that does not depend on a choice of the basis functions.

3.2 The Nystrom Method

In general, an integral equation of the Fredholm type

$$G(p)\phi(p) + \int_0^\infty F(p, p') \phi(p') dp' = \lambda \phi(p) \quad (28)$$

can be rewritten as a matrix equation as

$$\sum_{j=1}^N K_{ij} \phi_j \equiv \sum_{j=1}^N (G_{ii} + F_{ij}) \phi_j = \lambda \phi_i, \quad (29)$$

where K_{ij} is the kernel and i and j are now indices corresponding to p and p' . Instead of integrating over p from 0 to ∞ , we integrate over x from -1 to 1. Transform x_i to p_i by the transformation

$$p(x) = \tan \left(\frac{1+x}{4} \pi \right). \quad (30)$$

The mesh points x_i and the weights wt_i are generated by the gaussian quadrature rule using the routine `gauleg` from *Numerical Recipes* [37]. In order to integrate along $x \in [-1, 1]$ instead of $p \in [0, \infty)$, Eq. [28] is transformed as

$$G(x)\phi(x) + \int_{-1}^1 F(x, x') \phi(x') \frac{dp'}{dx'} dx' = \lambda \phi(x) \quad (31)$$

Changing the dummy variable inside the integral and substituting the differentiation of Eq. [30] with

$$dp = \frac{\pi}{4} \sec^2 \left(\frac{1+x}{4} \pi \right) dx = \frac{\pi}{4} (1+p^2) dx \quad (32)$$

gives

$$\frac{p_i^2}{2\mu} \phi_i + \frac{\lambda_L}{4p_i^2} \int_{-1}^1 Q'_0(y \neq 1) [\phi_j - \phi_i] \sec^2 \left(\frac{1+x_j}{4} \pi \right) dx_j = E \phi_i. \quad (33)$$

Eq. [33] can now be written as a matrix equation,

$$\begin{aligned} \frac{p_i^2}{2\mu} \phi_i + \frac{\lambda_L}{4p_i^2} \sum_{j=1}^N Q'_0(y \neq 1) \phi_j \sec^2 \left(\frac{1+x_j}{4} \pi \right) wt_j \\ - \frac{\lambda_L}{4p_i^2} \phi_i \sum_{k=1}^N Q'_0(y \neq 1) \sec^2 \left(\frac{1+x_k}{4} \pi \right) wt_k = E \phi_i. \end{aligned} \quad (34)$$

The left hand side of Eq. [34] is the kernel times the eigenvector and the right hand side is the eigenvalue times the eigenvector. The sum over k is independent of the eigenvector, which is just a scalar. The terms on the left that have only one index i belong to the diagonal elements K_{ii} . The terms with mixed indices i and j make up the off-diagonal elements, K_{ij} . More explicitly, the matrix elements of the kernel are

$$K_{ii} = \frac{p_i^2}{2\mu} - \frac{\lambda_L}{4p_i^2} \sum_k Q'_0(y \neq 1) (1+p_k^2) wt_k, \quad (35)$$

$$K_{ij} = \frac{\lambda_L}{4p_i^2} Q'_0(y) (1+p_j^2) wt_j, \quad (i \neq j). \quad (36)$$

So far the kernel \mathbf{K} is asymmetric under the interchange of i and j . We can improve the stability and the efficiency of the numerical solutions by symmetrizing Eq. [34]. We do so by multiplying the equation with $p_i^2 (1+p_i^2)$. It will change the original matrix equation

$$\mathbf{K} \cdot \mathbf{x} = \lambda \mathbf{x} \quad (37)$$

to an equivalent matrix equation

$$\mathbf{K}' \cdot \mathbf{x} = \lambda \mathbf{C} \cdot \mathbf{x}, \quad (38)$$

where \mathbf{C} is a diagonal matrix and $\mathbf{K}' = \mathbf{C} \cdot \mathbf{K}$. If \mathbf{C} is positive definite, meaning

$$\mathbf{x}^T \cdot \mathbf{C} \cdot \mathbf{x} \geq 0, \quad \forall \text{ vectors } \mathbf{x}, \quad (39)$$

then \mathbf{C} can be Cholesky-decomposed as

$$\mathbf{C} = \mathbf{L} \cdot \mathbf{L}^T, \quad (40)$$

where \mathbf{L} is a unique lower triangular matrix. The reason for performing Cholesky decomposition is that the new matrix

$$\mathbf{K}'' \equiv \mathbf{L}^{-1} \cdot \mathbf{K}' \cdot (\mathbf{L}^{-1})^T \quad (41)$$

is real symmetric and yields the same eigenvalues as Eq. [38]. In the case of $C_{ii} = p_i^2 (1 + p_i^2)$, \mathbf{C} is guaranteed to be positive definite. After symmetrization, Eq. [35] does not change ($K''_{ii} = K_{ii}$) while Eq. [36] becomes

$$K''_{ij} = \frac{\lambda_L}{4p_i p_j} Q'_0(y) \sqrt{(1 + p_i^2)(1 + p_j^2) w_i w_j}, \quad (i \neq j). \quad (42)$$

The eigenvalues of \mathbf{K}'' can be calculated by using standard packages such as EISPAK. In this paper, we use the `tred2` and `tqli` routines in *Numerical Recipes* [37].

3.3 The Correction Method

Maung, Norbury and Kahana [33, 35] have shown that the subtraction method does not completely remove the singularity at $y = 1$. There is a residual simple pole term

$$-\frac{4\lambda_L}{\pi} \frac{d\phi_{n0}}{dp} \int_0^\infty \frac{p'^2}{(p' + p)^2(p' - p)} dp' \quad (43)$$

remaining after the subtraction. The basis function method evaluates the Cauchy principal value by the Sloan method as described in Section 2. The Sloan method eliminates the simple pole term by integrating symmetrically around the singularity. Symmetrical integration involves splitting the range of integration into two intervals,

$$\int_0^\infty dp' = \int_0^{2p} dp' + \int_{2p}^\infty dp'. \quad (44)$$

The singularity at $p = p'$ is contained in the first term on the right hand side of Eq. [44] which is assigned a symmetric transformation rule $(dp'/dx)_1$. The second term generally has a different transformation rule $(dp'/dx)_2$ because it is mapping

between two different sets, namely $(2p, \infty) \rightarrow (1, M]$ (for some real number M), such that

$$\int_0^\infty dp' \rightarrow \int_{-1}^1 \left(\frac{dp'}{dx'} \right)_1 dx' + \int_1^M \left(\frac{dp'}{dx'} \right)_2 dx'. \quad (45)$$

Notice that the division of the range of integration moves with p . If two transformation rules are used with a moving division, each row (column) of the kernel has a different way to map $[0, \infty)$ to $[-1, M]$. But the eigenvector $\phi(p)$ must be mapped to ϕ_i in a unique way. This mismatch between the mappings of the kernel and the eigenvector does not affect the basis function method (see Eq. [2.24] of reference [33])

$$\begin{aligned} & \sum_{i=1}^N C_i \left[\int_0^\infty \frac{p^4}{2\mu} g_j(p) g_i dp + \frac{\lambda_L}{\pi} \int_0^\infty \int_0^\infty Q'_0(y) g_j(p) [g_i(p') - g_i(p)] dp' dp \right] \\ = & E \sum_{i=1}^N C_i \int_0^\infty p^2 g_j(p) g_i(p) dp \end{aligned} \quad (46)$$

because the eigenvector C_i is an N -tuple of the coefficients of the basis function expansion of the wavefunction $\phi(p)$ and is independent of the transformation rules. In the case of the Nystrom method, the problem is real, at least for the range of integration that we are interested in. Therefore we cannot evaluate the Cauchy principal value by symmetric integration in the Nystrom method. In other words, a new method is needed to treat the errors arising from the simple pole term.

So far the error term Eq. [43] is not included in the Nystrom kernel in our derivation and is contributing to the errors of the eigenvalues. Since the error term Eq. [43] involves $d\phi/dp$, we associate it with the error of the wavefunction

$$\Delta\phi = \Delta p \frac{d\phi}{dp} \sim \frac{1}{N} \frac{d\phi}{dp}, \quad (47)$$

where the mesh size Δp has an N^{-1} dependence. This fact leads to an estimate of the N dependence of the error of the eigenvalue, ΔE . Let the approximate eigenvector to be ϕ' and the approximate eigenvalue E' . It is reasonable to say that an approximate kernel K acting on an approximate eigenvector ϕ' yields an approximate eigenvalue E' as in

$$K\phi' = E'\phi' \quad (48)$$

$$\Rightarrow K(\phi + \Delta\phi) = (E + \Delta E)(\phi + \Delta\phi). \quad (49)$$

It is easy to see that

$$\begin{aligned}
 \Delta E &\simeq (K - E) \frac{\Delta \phi}{\phi} \\
 &= \left(\frac{K - E}{\phi} \right) \frac{d\phi}{dp} \Delta p \\
 &= \epsilon \frac{1}{N}
 \end{aligned} \tag{50}$$

It is safe to assume that $(K - E)d\phi/dp \ll 1$. ϕ^{-1} can be interpreted as the normalization. The product of all of the pseudo-constants is labelled as the coefficient ϵ . The approximate eigenvalue E' produced in the background of Eq. [43] is related to the true eigenvalue E by

$$E'_n = E_n + \epsilon f_n(N), \tag{51}$$

where n is the principal quantum number, ϵ a constant and $f_n(N)$ is a function approximately equals to N^{-1} . In general, $f_n(N)$ varies slightly depending on the type of integral equation and the potential. As a first order approximation, assume that

$$f_n(N) = N^{-1-\alpha(n-1)}. \tag{52}$$

The exponent of Eq. [52] is a first order Taylor series expansion of some negative unity function around $n = 1$. The constant α is always taken to be small. More particularly, choose an α such that the variance of E_n and ϵ and χ^2 are minimized in the linear fit. Finally the refinement of an eigenvalue involves generating a set of E'_n for various N by the Nystrom method and then extrapolating E_n by a χ^2 linear fit in the graph of E_n versus $f_n(N)$. In the case of Eq. [21], $\alpha = 0.004$ is an optimal choice. The numerical results are explained in Section 6.

The order of the Nystrom algorithm is derived from those of `tred2` and `tqli`, which is $\mathcal{O}(N^2)$ [37], compared with the basis function's $\mathcal{O}(M^2N)$, which comes from the product of the size of the matrix M^2 and the number of integration mesh points. N is typically around 1000 and M is 20. The basis function method is generally more efficient than the Nystrom method. However, for any given set of basis functions, the accuracy of the eigenvalues cannot be improved arbitrarily by increasing the number of basis functions because M is bounded from above due to numerical errors. The prospect of improving the accuracy of the basis function algorithm depends on the availability of a set of more suitable basis functions for a specific problem. In the case

of the Nystrom plus correction method, accuracy is optimized automatically by the correction scheme. The numerical results obtained by the Nystrom and basis function methods are quoted with optimal accuracy in this paper.

3.4 Exact S-state Solution

The eigenvalue of Eq. [21] can be solved exactly in configuration space. We shall use the analytic results to check our numerical results. The non-relativistic Schrödinger equation can be written as

$$\left(\frac{d^2}{dr^2} + \frac{2}{r} \frac{d}{dr} \right) R - 2\mu[\lambda_L r - E] R = 0. \quad (53)$$

Let $S \equiv r R$, then Eq. [53] can be simplified as

$$\frac{d^2}{dr^2} S - 2\mu[\lambda_L r - E] S = 0. \quad (54)$$

Define a new variable

$$x \equiv \left(\frac{2\mu}{\lambda_L^2} \right)^{\frac{1}{3}} [\lambda_L r - E], \quad (55)$$

such that Eq. [53] can be transformed as

$$S'' - xS = 0, \quad (56)$$

which is the Airy equation. The solution which satisfies the boundary condition $S \rightarrow 0$ as $x \rightarrow \infty$ is the Airy function $\text{Ai}(x)$. It is easy to show that the eigen-energy formula is

$$E_n = -x_n \left(\frac{\lambda_L^2}{2\mu} \right)^{\frac{1}{3}}, \quad (57)$$

where x_n is the n -th zero of the Airy function counting from $x = 0$ along $-x$. In reference [35], the values $\lambda_L = 5$ and $\mu = 0.75$ are used. In this case, the eigen-energy formula is

$$E_n = -2.554364772 x_n. \quad (58)$$

3.5 Numerical Results for the S-state

The accuracy of the Nystrom plus correction method is sensitive to the range of N . In this paper, increments of 100 in the range of $100 \leq N \leq 1400$ are used. The reason for this choice is that there are not enough spacings between the eigenvalues for $N < 100$ and for $N > 1500$ the numerical noise begins to corrupt the monotonic convergent behavior of the eigenvalues. The correct eigenvalues are extrapolated from these numerical data by a χ^2 linear fit as described in Section 4. The exact S -state eigenvalues are tabulated against the numerical results obtained by the basis function method and the Nystrom plus corrections method in Table [1]. It shows that the numerical results obtained by the Nystrom method plus corrections are more accurate than the results obtained by the basis function method.

The kernel written for the non-relativistic Schrödinger equation can be easily generalized to that of the relativistic 2-body Thompson equation in the center-of-mass frame by the replacement

$$\frac{p^2}{2\mu} \rightarrow 2 \left(\sqrt{p^2 + m^2} - m \right), \quad (59)$$

where μ is the reduced mass and m is the mass of each of the two equal mass elementary particles. The numerical results obtained using the Thompson equation is compared against those using the non-relativistic Schrödinger equation in Table [2] calculating to 2 decimal places. Our new results are exactly the same as the previous results obtained in reference [33] that uses basis functions $g_i^A(p)$ from Eq. [22].

3.6 $l \neq 0$ Kernels

The $l \neq 0$ kernels for the linear and Coulomb potentials contain the Legendre function of the second kind $Q_l(y)$ and its derivative respectively. There are several mathematical issues that need to be addressed before constructing the $l \neq 0$ kernels. First of all, the definition of

$$y \equiv \frac{p^2 + p'^2}{2p'p} = \frac{1}{2} \left(\frac{p}{p'} + \frac{p'}{p} \right) \quad (60)$$

is easily seen to yield $y > 1$ for $p, p' > 0$. In reference [33], Maung *et al.* use the Legendre identity

$$\begin{aligned} Q_l(y) &= P_l(y)Q_0(y) - w_{l-1}(y), \\ w_{l-1}(y) &= \sum_{m=1}^l \frac{1}{m} P_{l-m}(y)P_{m-1}(y), \end{aligned} \quad (61)$$

which is valid for $-1 \leq y \leq 1$ [39, 40] but can be extended to $y > 1$ by analytic continuation [41]. $Q'_l(y)$ is easily obtained by straightforward differentiation. The derivative of Legendre polynomial can be calculated from one of the recurrence formulas,

$$\frac{dP_l(y)}{dy} = y \frac{dP_{l-1}(y)}{dy} + lP_{l-1}(y), \quad (62)$$

which can be computed numerically by a recursive call. The Legendre function can be generated by modifying the routine `plgndr` in *Numerical Recipes* [37] to allow $y > 1$. The accuracy of Eq. [61] and its derivatives are generally sufficient. Slightly more accurate results can be obtained by the explicit evaluation of the Neumann integral,

$$Q_l(y) = \frac{1}{2} \int_{-1}^1 \frac{1}{(y-t)} P_l(t) dt, \quad (63)$$

with derivative

$$Q'_l(y) = -\frac{1}{2} \int_{-1}^1 \frac{1}{(y-t)^2} P_l(t) dt. \quad (64)$$

The first few $Q_l(y)$ are

$$Q_0(y) = \frac{1}{2} \ln \frac{y+1}{y-1}, \quad (65)$$

$$Q_1(y) = \frac{1}{2} y \ln \frac{y+1}{y-1} - 1, \quad (66)$$

$$Q_2(y) = \frac{1}{4} (3y^2 - 1) \ln \frac{y+1}{y-1} - \frac{3}{2} y, \quad (67)$$

$$Q_3(y) = \frac{1}{4} (5y^3 - 3y) \ln \frac{y+1}{y-1} - \frac{5}{2} y^2 + \frac{2}{3}, \quad (68)$$

$$Q_4(y) = \frac{1}{16} (35y^4 - 30y^2 + 3) \ln \frac{y+1}{y-1} - \frac{35}{8} y^3 + \frac{55}{24} y, \quad (69)$$

$$Q_5(y) = \frac{1}{16} (63y^5 - 70y^3 + 15y) \ln \frac{y+1}{y-1} - \frac{63}{8} y^4 + \frac{49}{8} y^2 - \frac{8}{15}. \quad (70)$$

$Q'_l(y)$ can be obtained by the direct differentiation of $Q_l(y)$, such that

$$Q'_0(y) = \frac{1}{1-y^2}, \quad (71)$$

$$Q'_1(y) = \frac{y}{1-y^2} - \frac{1}{2} \ln \frac{y-1}{y+1}, \quad (72)$$

$$Q'_2(y) = \frac{1}{1-y^2} - \frac{3}{2} y \ln \frac{y-1}{y+1} - 3, \quad (73)$$

$$Q'_3(y) = \frac{y}{1-y^2} - \frac{15y^2-3}{4} \ln \frac{y-1}{y+1} - \frac{15}{2} y, \quad (74)$$

$$Q'_4(y) = \frac{1}{1-y^2} - \frac{35y^3-15y}{4} \ln \frac{y-1}{y+1} - \frac{35}{2} y^2 + \frac{5}{3}, \quad (75)$$

$$Q'_5(y) = \frac{y}{1-y^2} - \frac{315y^4-210y^2+15}{16} \ln \frac{y-1}{y+1} - \frac{315}{8} y^3 + \frac{105}{8} y. \quad (76)$$

As $y \rightarrow \infty$, it is easily seen that $Q_0(y) = Q'_0(y) \rightarrow 0$. This limit is true for all $Q_l(y)$ and $Q'_l(y)$ from applying the L'Hopital rule. Unfortunately straightforward numerical calculation of $Q_l(y)$ and $Q'_l(y)$ by using Eqs. [65-76] leads to serious numerical errors as $y \rightarrow \infty$. At the same time, it is observed that the numerical integration of Eq. [63,64] are reasonably accurate in the same regime. Therefore the two representations are combined to minimize numerical error by using the Neumann integrals for $y > y_0$ and the explicit formulas for $y \leq y_0$. Our codes use $y_0 = 50$.

The subtracted momentum space NRSE with a linear potential is given in reference [33], which can be simplified as

$$\begin{aligned} & \frac{p^2}{2\mu} \phi_{nl}(p) + \frac{\lambda_L}{\pi p^2} \int_0^\infty Q'_l(y) \phi_{nl}(p') dp' - \frac{\lambda_L}{\pi p^2} \phi_{nl}(p) \int_0^\infty Q'_0(y) dp' \\ & - \frac{\lambda_L}{\pi p} \frac{l(l+1)}{2} \phi_{nl}(p) \int_0^\infty \frac{Q_0}{p'} dp' + \frac{\lambda_L \pi}{p} \frac{l(l+1)}{4} \phi_{nl}(p) = E_{nl} \phi_{nl}(p). \end{aligned} \quad (77)$$

The matrix elements of a symmetric kernel for arbitrary l are

$$\begin{aligned} K_{ii} &= \frac{p_i^2}{2\mu} - \frac{\lambda_L}{4p_i^2} \sum_k Q'_0(y \neq 1) (1+p_k^2) wt_k, \\ & - \frac{\lambda_L}{4p_i} \frac{l(l+1)}{2} \sum_k \frac{Q_0(y \neq 1)}{p_k} (1+p_k^2) wt_k + \frac{\lambda_L \pi}{4p_i} l(l+1) \\ & - \frac{\lambda_L}{4p_i^2} w'_l(1) (1+p_i^2) wt_i \end{aligned} \quad (78)$$

$$K_{ij} = \frac{\lambda_L}{4p_i p_j} Q'_l(y) \sqrt{(1+p_i^2)(1+p_j^2)} wt_i wt_j, \quad (i \neq j). \quad (79)$$

Despite our method to control numerical noise, numerical errors still manifest themselves in the form of spurious large negative eigenvalues for $l \geq 8$. Fortunately the rest of the positive eigenvalues are accurate. Some sample eigenvalues for $0 \leq l \leq 5$ are shown in Table [3] which also compares the eigenvalues generated by both the p -space and r -space codes. The r -space eigenvalues are calculated by solving NRSE using the relaxation method [43].

The Lande-subtraced momentum space NRSE equation with a Coulomb potential is also given in reference [33] and is simplified as

$$\begin{aligned} \frac{p^2}{2\mu} \phi_{nl}(p) + \frac{\lambda_C}{\pi p} \int_0^\infty Q_l(y) \phi_{nl}(p') p' dp' \\ - \frac{\lambda_C}{\pi} p \phi_{nl}(p) \int_0^\infty \frac{Q_0(y)}{p'} dp' + \frac{\lambda_C \pi}{2} p \phi_{nl}(p) = E_{nl} \phi_{nl}(p). \end{aligned} \quad (80)$$

The kernel of a Coulomb potential can be symmetrized the same way as that of a linear potential. The matrix elements are

$$\begin{aligned} K_{ii} = \frac{p_i^2}{2\mu} - \frac{\lambda_C}{4} p_i \sum_k \frac{Q_0(y \neq 1)}{p_k} (1+p_k^2) wt_k + \frac{\lambda_C \pi p_i}{2} \\ - \frac{\lambda_C}{4} w_l(1) (1+p_i^2) wt_i \end{aligned} \quad (81)$$

$$K_{ij} = \frac{\lambda_C}{4} Q_l(y) \sqrt{(1+p_i^2)(1+p_j^2)} wt_i wt_j, \quad (i \neq j). \quad (82)$$

The correction method which we have developed for the linear potential cannot be used in the Coulomb case. The only available technique of refining the eigenvalues of a Coulomb potential is by the way of increasing the number of mesh steps N . Some sample eigenvalues are shown in Table [4]. Since both the linear and Coulomb potentials can be symmetrized using the same formalism, we can easily splice the two kernels together to calculate the eigenvalues of the Cornell (linear plus Coulomb) potential

$$V(r) = \frac{\lambda_C}{r} + \lambda_L r. \quad (83)$$

It is not surprising that the correction method derived for the linear potential may also work for the Cornell potential because we expect that the error of the Cornell

potential is dominated by the error of the linear potential term. But it is a surprise that the correction method works more accurately with the Cornell potential than the linear potential as evidenced by vanishingly small variance and χ^2 .

3.7 Summary

The basis function method requires *a priori* knowledge of the eigenfunctions in order to pick out an appropriate set of basis functions. The advantage of the Nystrom method is that no such prior knowledge of the eigenfunctions is needed. The kernel constructed by the Nystrom method is also much simpler than that by the basis function method. The eigenfunctions can be generated by the same Nystrom routines that compute the eigenvalues. The Nystrom plus correction is more accurate than the basis function method in the cases studied in this paper. In other words, the new method has all of the advantages—elegance, accuracy and versatility. In addition, the kernel of the relativistic and non-relativistic equation of motion with the Coulomb and linear potential can be symmetrized in exactly the same manner. It allows the calculation of the eigenvalues of a Cornell potential readily. Since the Nystrom method can be generalized for higher l 's, we can use it to calculate the Regge trajectories. Since the Thompson equation which we have solved is a 2-body equation, we can use it to analyze the experimental meson Regge trajectories [44]. This will be pursued in later work.

Table 1: Comparisons of eigen-energies in GeV of the non-relativistic Schrödinger equation with a linear potential between the Nystrom method and the basis Function (BF) method. The basis functions being referred to here are $g_i^B(p) = [(i/M)^2 + p^4]^{-1}$. The values of $l = 0$, $\lambda_L = 5$ GeV and $\mu = 0.75$ GeV are used.

n	Nystrom				BF	Exact
	$N = 100$	$N = 700$	$N = 1400$	Corrected		
1	5.899211	5.961921	5.967339	5.972379	5.972	5.972379
2	10.268443	10.417386	10.430047	10.442010	10.443	10.442114
3	13.767781	14.054263	14.078517	14.101276	14.104	14.101524
4	16.784747	17.258395	17.297500	17.335360	17.335	17.335728
5	19.467512	20.177458	20.234722	20.291708	20.293	20.292215
6	21.891635	22.887999	22.967933	23.046820	23.053	23.047142
7	24.101339	25.435892	25.541743	25.646532	25.648	25.646268
8	26.124257	27.851711	27.986463	28.121481	27.947	28.120787
9	27.977844	30.156480	30.323418	30.493311	30.194	30.488938
10	29.672260	32.366010	32.568895	32.778297	33.340	32.769375

Table 2: Comparisons of the ratios of Eigen-energies E_{n+1}/E_1 using the Thompson equation (TE) and the non-relativistic Schrödinger equation (NRSE) using $l = 0$ and $\lambda_L = 0.2 \text{ GeV}^2$. Mass is measured in GeV.

n	TE	NRSE	Mass
1	1.72	1.75	1.5
2	2.30	2.36	1.5
3	2.80	2.90	1.5
1	1.67	1.75	0.5
2	2.18	2.36	0.5
3	2.62	2.90	0.5
1	1.63	1.75	0.3
2	2.11	2.36	0.3
3	2.51	2.90	0.3

Table 3: Eigen-energies in GeV of the non-relativistic Schrödinger equation in momentum space (pNRSE) compared with those in the configuration space (rNRSE) and the relativistic Thompson equation in momentum space (TE). The r -space Thompson equation result is not available. The values of $n = 1$, $\lambda_L = 5$ GeV and $\mu = 0.75$ GeV are used.

l	pNRSE			Corrected	rNRSE
	$N = 100$	$N = 700$	$N = 1400$		Approx.
0	5.899211	5.961921	5.967339	5.972379	5.9719
1	8.528725	8.577713	8.582413	8.586002	8.5850
2	10.823099	10.847533	10.849675	10.851526	10.8514
3	12.917124	12.904221	12.902815	12.902117	12.9020
4	14.874248	14.812422	14.805462	14.801358	14.9790
5	16.730585	16.606651	16.597636	16.586361	16.5845
TE					
l	$N = 100$	$N = 700$	$N = 1400$	Corrected	NA
0	5.859885	5.914287	5.919054	5.923117	
1	8.164379	8.202282	8.205185	8.208610	
2	10.053574	10.067261	10.068464	10.069762	
3	11.700322	11.680163	11.678063	11.676817	
4	13.185124	13.121767	13.116634	13.111239	
5	14.553134	14.437612	14.427702	14.418173	

Table 4: Eigen-energies in eV of the hydrogen atom according to the non-relativistic Schrödinger equation with $n = 1$.

l	$N = 100$	$N = 1400$	$N = 3000$	Exact
0	-25.286631	-13.600349	-13.598508	-13.598289
1	-4.579043	-3.400415	-3.399659	-3.399572
2	-1.463504	-1.511499	-1.510980	-1.510921
3	-0.634523	-0.850358	-0.849940	-0.849893
4	-0.329730	-0.544332	-0.543972	-0.543932

Chapter 4

The Lund Model of String Fragmentation

String fragmentation models such as the Lund Model fit experimental particle production cross sections very well in the high energy limit. This paper gives an introduction of the massless relativistic string in the Lund Model and shows how it can be modified with a simple assumption to produce formulas for meson production cross sections for space radiation research. The results of the string model is compared against inclusive pion production data from proton-proton collision experiments.

4.1 Introduction

The Lund model is a $(1 + 1)$ massless relativistic string fragmentation model which will be modified with a simple assumption in this paper to produce formulas for meson particle production cross sections for HZETRN. The idea of modelling hadronic systems with strings went back to the 1960's [45]. The general skepticism on the extra dimensions predicted by string theory and the advent of QCD in the 1970's put string theory out of commission for the next decade. Interests in string theory rekindled in the 1980's when Green and Shwarz showed that string theory is anomaly-free and probably finite to all orders in perturbation theory. Today many advances in string theory have been made on the theoretical front. Despite all the excitement string

theory has generated in the high energy theory community, there is no evidence that string theory will make any low-energy limit prediction to be tested by experiments in the near future. Supersymmetry and superstring may be testable by experiments in the TeV scale but perhaps not directly relevant to the focus of space radiation research in the GeV scale. The interest lies mostly in the low-energy limit of a non-supersymmetric string theory, with the possible exception of understanding the Greisen-Zatsepin-Kuzmin (GZK) cutoff in the ultrahigh-energy cosmic ray spectrum using TeV strings [46].

String fragmentation has been a work horse in analyzing high energy particle production. N. Isgur proposed a fluxtube model in which the color force field is thought as a string-like object [47, 48]. B. Andersson implemented the idea of string fragmentation formally in the Lund Model [49, 50, 51] which is implemented in the JETSET and Pythia Monte-Carlo programs [52]. If a Monte-Carlo cross section program is put into a target code, it will not run in a short time. Therefore we need simple parameterizations of cross section formulas, which is the aim of the present work. In this paper, we first give a review of the original Lund Model and expand some of the derivations of reference [49]. Later we show how to modify the Lund Model by inserting a simple assumption to generate formulas for meson production cross sections.

Appendix A defines the basic kinematic notations. Appendix B explains the basic concepts of the Lund Model and derives the invariant amplitude formulas. The formulas in the appendices are taken from reference [49] chapters 6-8. This work merely serves to focus on a subsection of reference [49] relevant to our discussion and expands the derivations. Section 4.2 of this paper explains a new idea on how to use a simple ansatz to obtain formulas for production cross sections in the Lund Model.

4.2 Cross Section Formulas

The basic result of the Lund Model is the “Area Law” which is summarized as [49]

$$dP_{ext} = ds \frac{dz}{z} (1-z)^a e^{-b\Gamma}, \quad (84)$$

$$dP_{int} = \prod_{j=1}^n N d^2 p_{0j} \delta^+(p_{0j}^2 - m^2) \delta \left(p_{rest} - \sum_{j=1}^n p_{0j} \right) e^{-bA_{rest}}, \quad (85)$$

and are derived in appendix B. The symbols Γ and A_{rest} are Lorentz invariant kinematic variables. Γ defines the surface of constant proper time along which the string is broken. Traditionally the Lund Model results in Eqs. (84) and (85) are incorporated into Monte Carlo simulation programs such as JETSET and PYTHIA to compute cross sections. Since the goal of the HZETRN program is to derive simple cross section formulas for the cross sections, numerical calculations are not wanted. In this section, some simple assumptions are made to derive analytical results.

Eq. (85) resembles the quantum mechanical result

$$d\sigma = d\Omega(s; p_{01}, \dots, p_{0n}) |\mathcal{M}|^2, \quad (86)$$

and [25]

$$d\sigma = \frac{(2\pi)^4}{4\sqrt{(p_1 \cdot p_2)^2 - m_1^2 m_2^2}} \delta^4 \left(p_1 + p_2 - \sum_{i=3}^{n+2} p_i \right) \prod_{i=3}^{n+2} \frac{d^3 p_i}{(2\pi)^3 2E_i} |\mathcal{M}|^2. \quad (87)$$

By analogy, it is assumed that [49]

$$|\mathcal{M}|^2 = e^{-bA_{rest}}. \quad (88)$$

In principle, $A_{total} = \Gamma + A_{rest}$ can also be used in Eq. (88) in place of A_{rest} . In this case, the only difference is a proportionality constant $\exp(-b\Gamma)$ in the invariant amplitude $|\mathcal{M}|^2$. Hence the assumption in Eq. (88) is the simplest. The string breaks up along a surface of constant proper time Γ which is determined by the distribution [49]

$$H(\Gamma) = C \Gamma^a e^{-b\Gamma}. \quad (89)$$

By setting $dH/d\Gamma = 0$, it is easy to show that the maximum of $H(\Gamma)$ is [49]

$$\Gamma_{max} = \frac{a}{b}. \quad (90)$$

The mean proper time is [49]

$$\langle \Gamma \rangle = \frac{\int_0^\infty \Gamma H(\Gamma) d\Gamma}{\int_0^\infty H(\Gamma) d\Gamma} = \frac{a+1}{b}. \quad (91)$$

The fact that the constants a and b are constants in Γ as shown in appendix B does not exclude the possibility that they are functions of rapidity. Since string fragmentation

is a stochastic process which occurs over a surface of constant proper time on the average, $\langle \Gamma \rangle$ is expected to be an absolute constant. It means that

$$a = a_0 f(y) - 1, \quad (92)$$

$$b = b_0 f(y). \quad (93)$$

for some function of rapidity $f(y)$. The goal of a consistent string theory is to calculate a_0 , b_0 and $f(y)$ analytically. Such will be the topic of a subsequent paper. In this paper, it is simply assumed that

$$f(y) = \frac{2m_T \sinh y}{\sqrt{s'}} = \frac{2p_z}{\sqrt{s'}} \approx x, \quad (94)$$

where $m_T = \sqrt{m^2 + p_T^2}$. The kinematic identities of Eq. (94) are taken from reference [25]. The ansatz $f(y) = x$ is motivated by *a posteriori* considerations when fitting experimental data. The theoretical derivation of this operational assumption will be a topic of future works. In NASA space radiation research, cosmic particles are highly energetic. The production is mostly forward. In the center-of-mass frame, the longitudinal momentum is labelled p_z and the total energy of the colliding particles is $\sqrt{s'}$. According to the Fermi Golden rule,

$$\frac{d\sigma}{dx} \sim |\mathcal{M}|^2. \quad (95)$$

Together with Eqs. (93) and (94), the differential cross section is found to be

$$\frac{d\sigma}{dx} = A e^{-Bx}, \quad (96)$$

for some constants A and B . This prediction is consistent with experimental data as shown in Figures 19 and 20.

The spectral distribution can be obtained from the cross section formula in reference [53]

$$\frac{d\sigma}{dE} = 2\pi p \int_0^{\theta_{max}} d\theta E \frac{d^3\sigma}{dp^3} \sin \theta. \quad (97)$$

By using approximations $p_z \approx E$ and $x \sim p_z/\sqrt{s}$ in the high energy limit and Eq. (95) in conjunction of Eq. (97), the spectral distribution is found to be

$$\begin{aligned} \frac{d\sigma}{dE} &\sim 2\pi(1 - \cos \theta_{max}) p_z |\mathcal{M}|^2 \\ &= c E e^{-kE}, \end{aligned} \quad (98)$$

where c and k are constants. Unfortunately there is no experimental data on $d\sigma/dE$ for pion production in proton-proton scattering. Blattnig *et al.* produced a parameterized spectral distribution by integrating $E d^3\sigma/dp^3$ [53] which will be compared to analytical results in a later paper.

4.3 Summary

The Monte-Carlo programs JETSET and PYTHIA cannot be used in HZETRN due to excessive running time. Parametrizations of cross section formulas are needed. The new idea is to make simple assumptions within the Lund Model framework to obtain analytic meson production cross section formulas. Our purpose is not to produce any parameterization. To this end, all of the fits in this work have parameters that are simply hand-picked for the sake of illustrating the correctness of the qualitative aspects of cross sections predicted by string theory. Figures 19 and 20 clearly demonstrate the success of the fits. A major assumption of this paper is that a and b in Eq. (89) are not constants as proposed in the original Lund Model but are functions of rapidity. This assumption allows us to obtain the correct qualitative features of the cross sections without resorting to a Monte-Carlo simulation. At the present, the functions a and b are adjusted to fit the data.

4.4 Future Work

The exact forms of the parameters a and b Eqs. (92) and (93) for various types of production will be calculated from non-supersymmetric string theory, such as the QCD string model [65]. The concept of confinement by a string is quantified in terms of the minimal area law of the Wilson loop. QCD string models also include the gluonic degrees of freedom. The constants A and B in Eq. (96) and the constants c and k in Eq. (98) will also be calculated from string theory. The $(1+1)$ Lund Model cannot give angular dependence which will be important for low p_z . Future work in string phenomenology hopefully can include the angular dependence of the cross sections near the threshold by extending the model to $(3+1)$ or higher dimensions. Production formulas will also be extracted from JETSET and PYTHIA to be used in HZETRN.

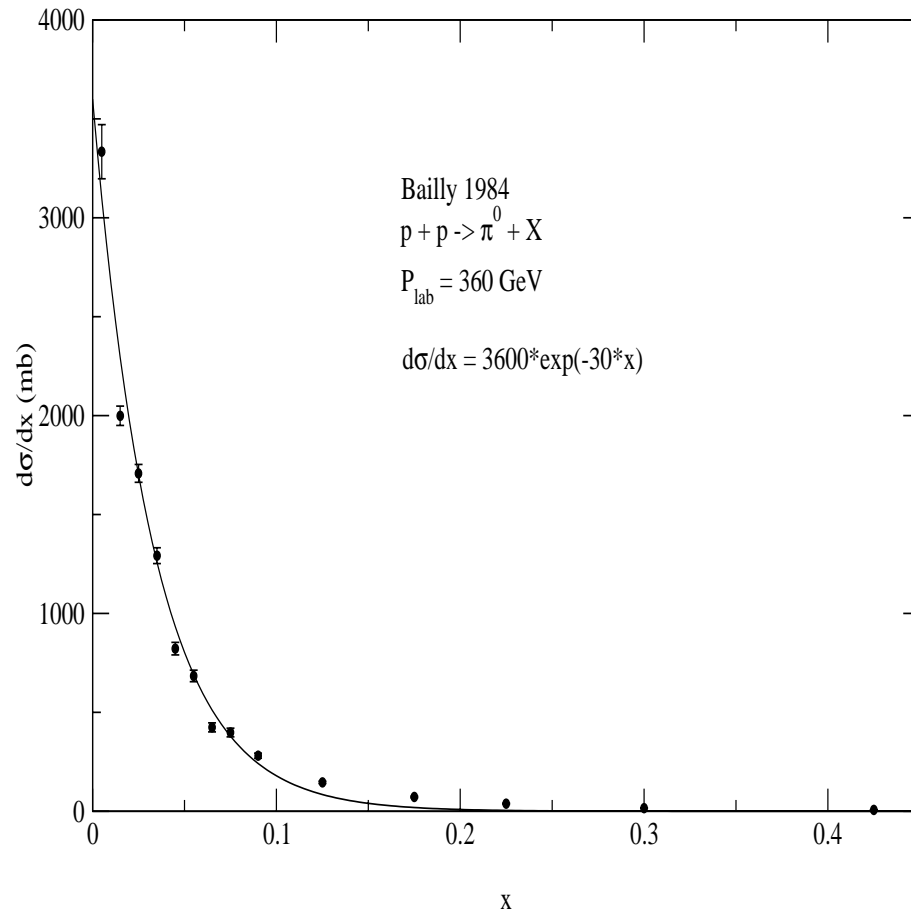


Figure 19: Comparison between experimental $d\sigma/dx$ and the string model result. The constants used in the exponential function are chosen to fit the data and are not parameterizations. The data are published by Bailly *et al.* in *Zeitschrift für Physik*, **C22**, 119 (1984).

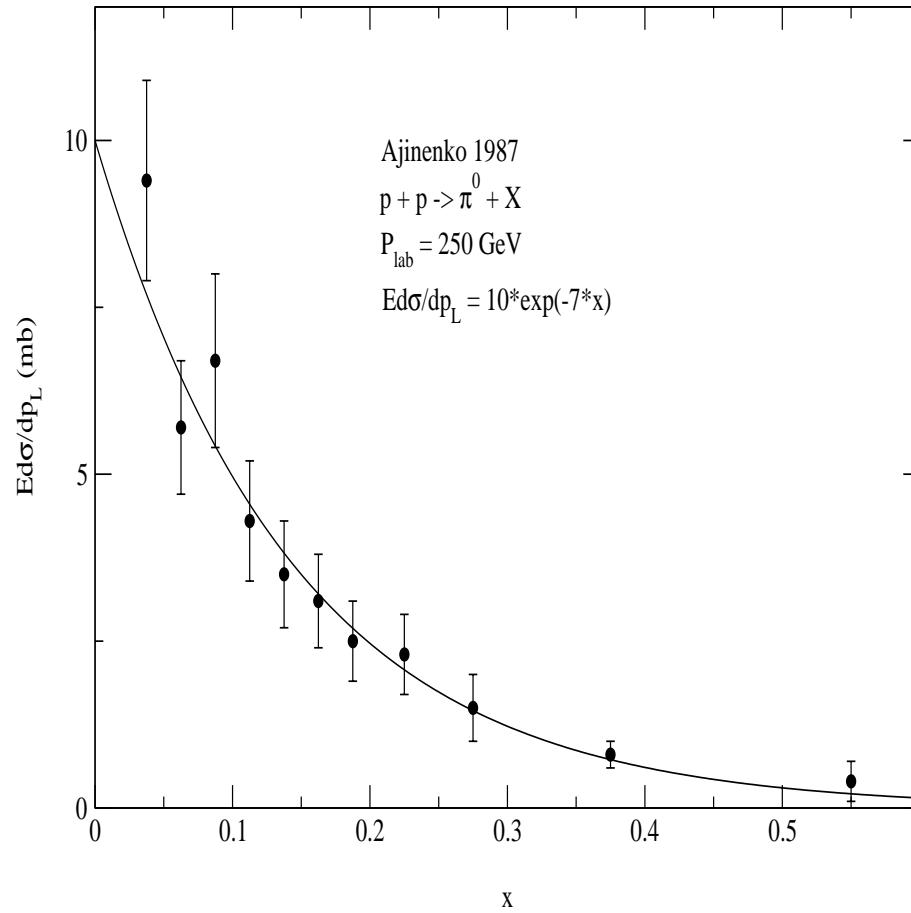


Figure 20: Comparison between experimental $E d\sigma/dp_L$ and the string model result. The constants used in the exponential function are chosen to fit the data and are not parameterizations. The data are published by Ajinenko *et al.* in *Zeitschrift für Physik*, **C35**, 7 (1987).

Chapter 5

Hadron Production Formulas

Meson production cross sections from proton-proton (pp), proton-nucleus (pA) and nucleus-nucleus (AA) collisions are needed in the NASA space radiation transport code called HZETRN. This chapter first review Feynman-Field parton model of hadron production and then use it as a stepping stone for the construction of a modern counterpart using strings, solitons and instantons.

5.0.1 The Feynman-Field Model

Feynman and Field calculated the invariant production cross section formula using perturbative QCD by incorporating the structure functions (or pardon distribution functions), $f_{A/a}(x_a, Q^2)$, obtained from DIS experiments and the fragmentation functions, $D_q^h(z, Q^2)$, parameterized from data. The cross section formula

$$E \frac{d^3\sigma}{dp^3} = \frac{1}{\pi} \sum_{a,b} \int_{x_a^{min}}^1 dx_a \int_{x_b^{min}}^1 dx_b f_{A/a}(x_a, Q^2) f_{B/b}(x_b, Q^2) D_c^h(z_c, Q^2) \frac{1}{z_c} \frac{d\hat{\sigma}}{d\hat{t}}, \quad (99)$$

with

$$x_a^{min} = \frac{x_1}{1 - x_2}, \quad (100)$$

$$x_b^{min} = \frac{x_a x_2}{x_a - x_1}, \quad (101)$$

is derived explicitly in Appendix C.

A lot of effort has been invested in finding the best parameterizations of $E d^3\sigma/dp^3$ to speed up the HZETRN code [53]. This work takes a different approach by calculating the cross sections from fundamental theories. On the practical side of the consideration, it is hoped that the Monte Carlo integration scheme is a fast enough technology to calculate Eq. (99) in the NASA transport code. To this end, the time proven Monte Carlo integration package VEGAS is being tested. VEGAS uses a mixed strategy combining importance and stratified sampling. The details of this method can be founded in references [37, 54]. In order to save space, the explanation is limited to the inputs used in VEGAS as follow.

$$ndim = 2, \quad (102)$$

$$ncall = 5000, \quad (103)$$

$$itmx = 5, \quad (104)$$

$$nprn = 0, \quad (105)$$

$$xl[1] = regn[1] = \frac{x_1}{1 - x_2}, \quad (106)$$

$$xl[2] = regn[2] = \frac{x_2}{1 - x_1}, \quad (107)$$

$$xu[1] = regn[3] = 1.0, \quad (108)$$

$$xu[2] = regn[4] = 1.0. \quad (109)$$

The dimensional of the integration is $ndim$. The number of random calls in the Monte Carlo integration is $ncall$. The maximum number of iterations is $itmx$. The flag $nprn$ controls the initial conditions of the grids. In this case, $nprn = 0$ signals a cold start. The random sampling is confined to an n -dimensional rectangular box. In Lepage's original paper, the coordinates of the "lower left corner" are labelled as $xl[i]$, and those of the "upper right corner" are $xu[i]$. For a 2-dimensional integral, $i \in \{1, 2\}$. *Numerical Recipes* adapted Lepage's code [37] and puts $xl[i]$ and $xu[i]$ in an array labelled $regn[j]$ where $j \in \{1, \dots, 2*ndim\}$. The integrand of Eq. (99) is represented by the function `fxn` and is expressed in pseudo code as

```
if (x_b < x_a*x2/(x_a-x1)) return 0;
else (sum all the terms in the integrand);
```

The inclusive cross section of $pp \rightarrow \pi^0 X$ is chosen to test the Monte Carlo integration method. The most accurate parameterization of the parton distributions of proton is

given by the CTEQ6 package [55]. The CTEQ6 routine is computationally expensive and therefore will not be used in the final hadron code. However its accuracy is ideal for benchmarking the distribution functions to be constructed later. The QCD running coupling constant, $\alpha_s(Q^2)$, used in the code is the renormalized coupling constant described in Appendix C. A typical value of $\Lambda = 0.4$ GeV is used inside $\alpha_s(Q^2)$. The internal scattering cross sections of the reactions $q_i\bar{q}_i \rightarrow gg$ and $gg \rightarrow gg$ are excluded from the integral because gluons do not fragment into hadrons. The fragmentation functions used for this initial simulation are the original functions of Feynman and Field [56]. For the $pp \rightarrow \pi^0 X$ reaction, the fragmentation functions are

$$D_u^{\pi^0}(z) = D_d^{\pi^0}(z) = \left[\frac{\beta}{2} + \beta^2 \left(\frac{1-z}{z} \right) \right] (n+1)(1-z)^n, \quad (110)$$

$$D_s^{\pi^0}(z) = \beta^2 \left(\frac{1-z}{z} \right) (n+1)(1-z)^n, \quad (111)$$

$$D_d^{\pi^-}(z) = D_u^{\pi^+}(z) = \left[\beta + \beta^2 \left(\frac{1-z}{z} \right) \right] (n+1)(1-z)^n, \quad (112)$$

$$D_s^{\pi^\pm}(z) = D_d^{\pi^+}(z) = D_u^{\pi^-}(z) = \beta^2 \left(\frac{1-z}{z} \right) (n+1)(1-z)^n, \quad (113)$$

where $\beta = 0.4$. The distributions of c , b and t quarks are sufficiently low that

$$D_c^h(z) = D_b^h(z) = D_t^h(z) = 0, \quad (114)$$

for any hadron h . Feynman fixed $n = 2$ in his original paper. In this work, n is a parameter freely adjusted to fit the data. There is a subtlety involved in summing all the parton contributions over a and b in Eq. (99) that is related to the relative probabilistic nature of the parton distributions. The best way to explain it is by the way of an analogy. Suppose there is a room A occupied by 7 boys and 5 girls. The ratio of boys to girls in that room is 7:5. Suppose there is another room B of 14 boys and 10 girls. The ratio is also 7:5, or $\frac{7}{12} : \frac{5}{12}$ in normalized format. If a clerk wants to know the number of children in a room B , it is not enough to know the ratio of boys to girls. He must also be given a integral multiplicative constant. In this case, 2 times 7:5 or 24 times $\frac{7}{12} : \frac{5}{12}$ gives the correct head counts which is 14:10. In either case, an integral multiplicative constant must be provided. A similar situation arises in counting the number of partons in a hadron. The parton distributions are

normalized to unity so that they give only the relative distributions of the partons. The parton distributions give only the ratios of the partons in a hadron but not their numbers. In order to sum over a and b partons in Eq. (99) correctly, one must be provided with an integral multiplicative constant for each of the hadrons A and B . These multiplicative integral constants cannot be known *a priori* but are determined *a posteriori* by fitting data. In other words, Eq. (99) can be modified as

$$E \frac{d^3\sigma}{dp^3} = \frac{N_A N_B}{\pi} \sum_{\{a,b\}} \int_{x_a^{min}}^1 dx_a \int_{x_b^{min}}^1 dx_b \times f_{A/a}(x_a, Q^2) f_{B/b}(x_b, Q^2) D_c^h(z_c, Q^2) \frac{1}{z_c} \frac{d\hat{\sigma}}{d\hat{t}}, \quad (115)$$

where N_A and N_B are the multiplicative constants of $f_{A/a}(x_a, Q^2)$ and $f_{B/b}(x_b, Q^2)$ respectively and $\sum_{\{a,b\}}$ is the sum over the parton *types* instead of the sum over the partons *per se*. If $A = B$, the overall multiplicative constant, $N_A N_B$, is an integer square. If $A \neq B$, the overall constant, $N_A N_B$, is still an integer. In the case of fitting the pQCD calculations to experimental data of the $pp \rightarrow \pi^0 X$ reaction, a factor of 100 is missing if one simply sums over the parton types. It implies that the multiplicative constant for the parton distributions of a proton is $N_p = 10$.

Figures 21 and 22 illustrate the features of $E d^3\sigma/dp^3$ plotted against p_T . The plots show that the invariant cross section is visibly suppressed at high p_T for low \sqrt{s} and $\theta_{cm} \neq 90^\circ$. The suppression will eventually manifest itself at sufficiently high p_T regardless of the value of \sqrt{s} . However it is not yet clear whether these suppressions are real or just an artifact of pQCD. The scarcity of experimental data in these regions does not help to answer this question. The fits of the Feynman-Field model versus experimental data will be shown in the next section.

5.0.2 Parameterized Cross Section Formulas

Monte Carlo integration is the fastest numerical integration scheme available. But nothing will be faster than an explicit analytic formula. The NASA HZETRM code needs analytic formulas for the hadron production cross sections to optimize its speed. The Monte Carlo routine typically takes 3 or 4 seconds to compute a cross section on a Pentium3 1-GHz machine and is unsuitable for use in HZETRM. On the other hand, the explicit computation of the parton model integrals is a daunting task if in

principle tractable at all. These constraints lead to the development of the present parameterization scheme. The form of parameterized cross section formulas is taken to be

$$E \frac{d^3\sigma}{dp^3}(\sqrt{s}, p_T, \theta_{cm} = 90^\circ) = A \sum_{i=1}^3 e^{-\left(\frac{\alpha_i}{\sqrt{s}} + \beta_i\right)(p_T-1) - a_i\sqrt{s} - b_i}, \quad (116)$$

where the scale factor

$$A = E \frac{d^3\sigma}{dp^3}(\sqrt{s}, p_T = 1, \theta_{cm} = 90^\circ), \quad (117)$$

and the parameters α_i , β_i , a_i and b_i are determined jointly by experimental data and pQCD Monte Carlo calculations. The threshold $p_T = 1$ is set by the **CTEQ6** package. For this reason, his parameterization is meaningful only for $p_T > 1$. The rapidity distributions of hadron production is typically symmetric around $y = 0$. From [57]

$$\eta = -\ln[\tan(\theta/2)] = \frac{1}{2} \ln \left[\frac{\sqrt{m_T^2 \cosh^2 y - m^2 + m_T \sinh y}}{\sqrt{m_T^2 \cosh^2 y - m^2 - m_T \sinh y}} \right] \quad (118)$$

and

$$y = \frac{1}{2} \ln \left(\frac{E + p_z}{E - p_z} \right), \quad (119)$$

it can be easily shown that $y = 0$, $x_L = p_z/(p_z)_{max} = 0$ and $\theta_{cm} = 90^\circ$ are the same statements. Many experiments average the data over a range of y or x_L symmetric around zero. In these cases, the average center-of-momentum angle, $\bar{\theta}_{cm}$, would be 90° , which is assumed in the present parameterization. Hadron productions in space radiation problems are mostly in the forward direction or equivalently $\theta = 0$. For this reason, HZETRN is a one dimensional code in such a way that the angular dependence of the parameterized cross section formula is not explicitly needed. Figures 23-25 show the fits of the parameterized cross sections with pQCD calculations and experimental data at $\bar{\theta}_{cm} = 90^\circ$. The parameters are tabulated in Table 5. A guess at the angular dependence of the invariant cross section is

$$E \frac{d^3\sigma}{dp^3}(\sqrt{s}, p_T, \theta_{cm} = 90^\circ) = A \sum_{i=1}^3 e^{-\left(\frac{\alpha_i}{\sqrt{s}} + \beta_i\right)(p_T-1) - (a_i\sqrt{s} - b_i)\mathcal{T}}, \quad (120)$$

where $\mathcal{T} = \tan(\theta/2)$. A sample graph of the fit between the present parameterization and data with angular dependence is shown in Figure 26. The suppressions at relatively high p_T generated by the Feynman-Field model as shown in Figures 24, 25 and

26 are not parameterized. Experimental data do not favor these suppressions and the present parameterization fits data quite well. Until more experimental data are made available in the high p_T regions, the ambiguity of the discrepancies between the Feynman-Field model and the present parameterization has to be settled by further theoretical research.

The parameters in Table 5 are obtained by fitting experimental and pQCD Monte Carlo data by hand. Curve-fitting algorithm such as the Levenberg-Marquardt does not work well because the present model generate singular matrices in the code that crash the program. At this point, there is not a cleverer method to find these parameters automatically. When the parameters are obtained by hand, at least 2 data sets of $E d^3\sigma/dp^3$ versus p_T at different energies with $p_T > 1$ and $\bar{\theta}_{cm} = 90^\circ$ are needed for the purpose of linear regression analysis. Once the parameters are obtained, a third data set at yet another energy is needed to test the accuracy of the parameterization. These constraints limit the applicability of the present parameterization to those hadrons measured with copious data, such as the pions. It is the reason why the present analysis has not yet included other hadrons.

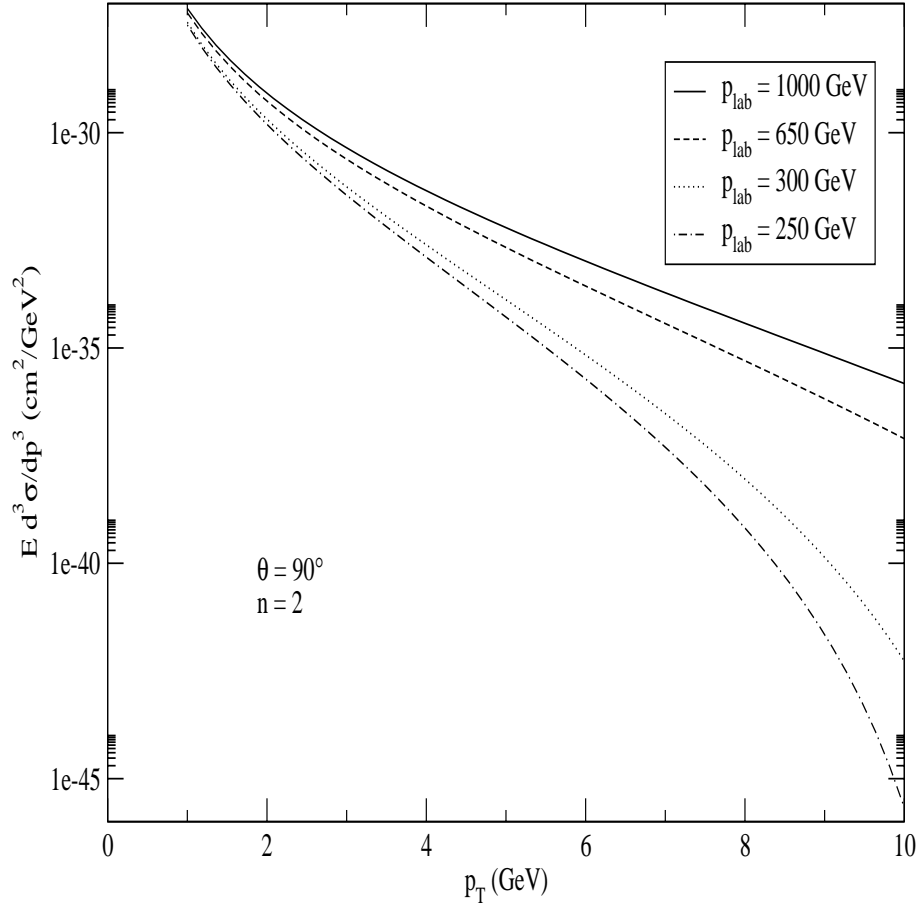


Figure 21: A sample plot of the Feynman-Field model for $pp \rightarrow \pi^+ X$ at different energies. The plot shows that the invariant cross section is suppressed at low \sqrt{s} and high p_T .

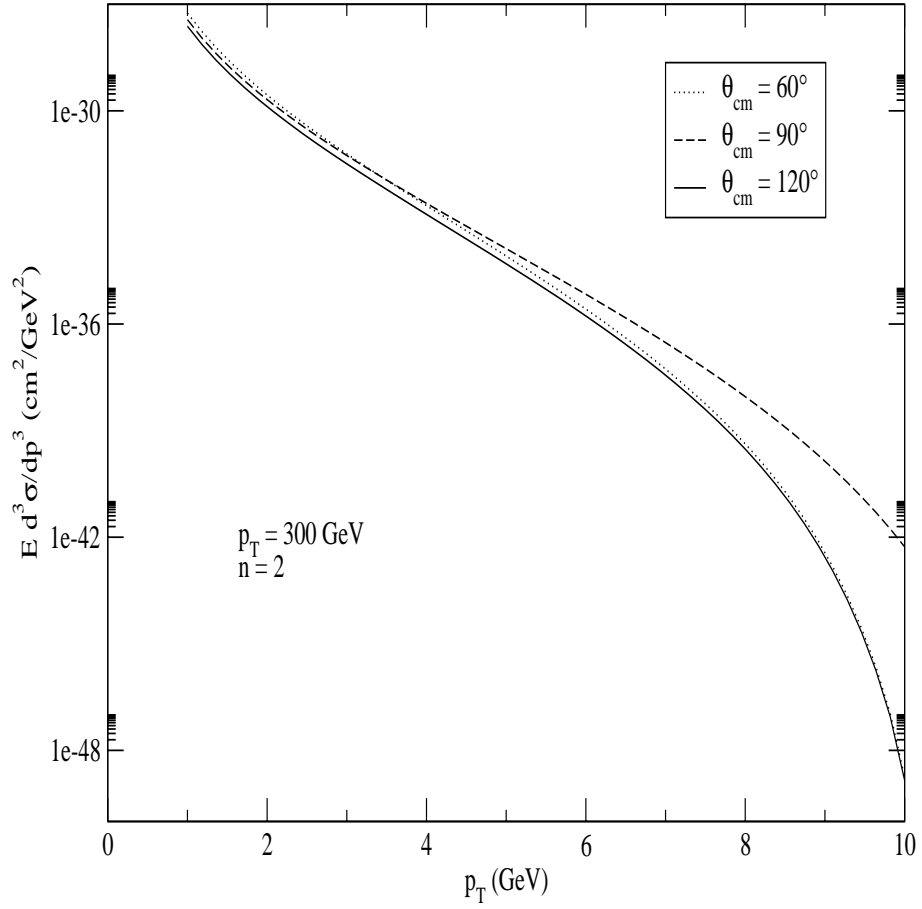


Figure 22: A sample plot of the Feynman-Field model for $pp \rightarrow \pi^+ X$ at different angles. The plot shows that the invariant cross section is symmetric around $\theta_{cm} = 90^\circ$ and is suppressed at high p_T for $\theta_{cm} \neq 90^\circ$.

Table 5: Parameters of the parameterized cross section formulas.

	π^0	π^+	π^-
A	4e-28	3e-28	3.4e-28
α_1	64.32	58.82	64.29
β_1	0.3793	0.5324	0.4414
a_1	0.1082	0.0679	0.087
b_1	0.196	2.524	1.455
α_2	55.93	58.82	51.02
β_2	2.112	1.982	2.184
a_2	0.0249	0.0023	0.0178
b_2	0.6053	1.777	1.103
α_3	55.93	0.0	0.0
β_3	4.112	6.0	6.0
a_3	-0.0104	-0.001	-0.0011
b_3	0.777	0.2129	0.1871

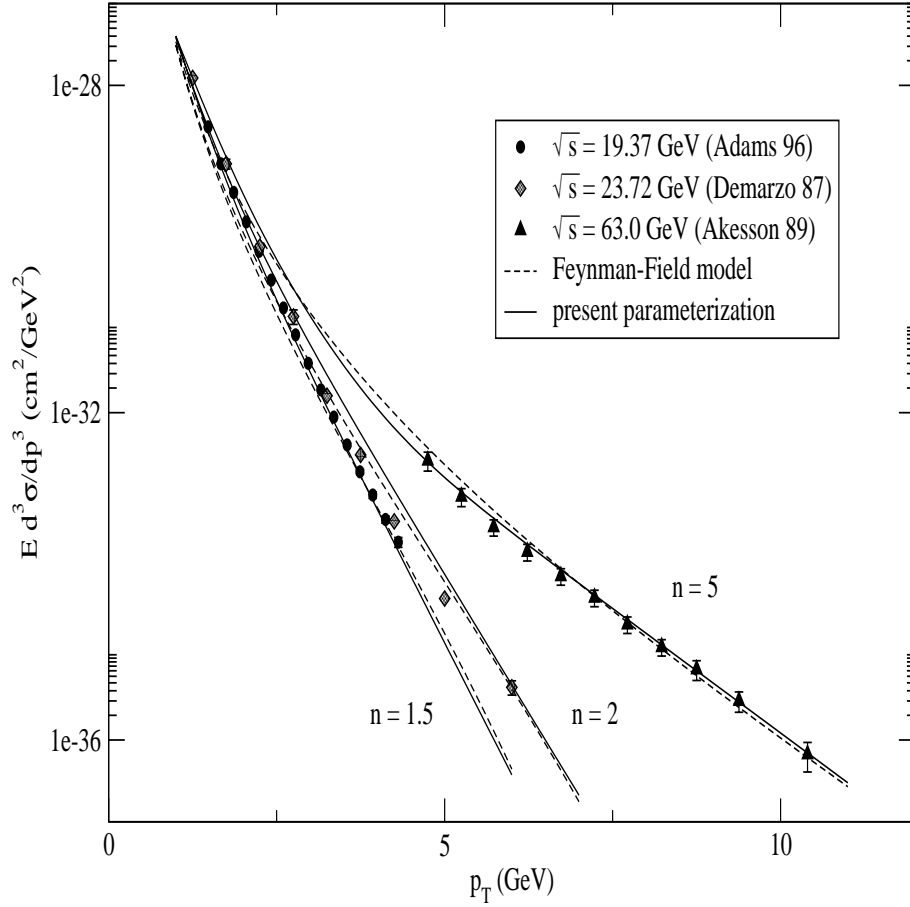


Figure 23: Comparisons of pQCD and parameterized cross sections with $pp \rightarrow \pi^0 X$ experimental data at $\bar{\theta}_{cm} = 90^\circ$. The parameter n in fragmentation functions of the Feynman-Field model are adjusted freely as shown in the graph to fit the data. The references of the data sets Adams 96, Demarzo 87 and Akesson 89 are PR D53 4747 (1996), PR D36 16 (1987) and CERN-EP/89-98 (Aug 1989) respectively.

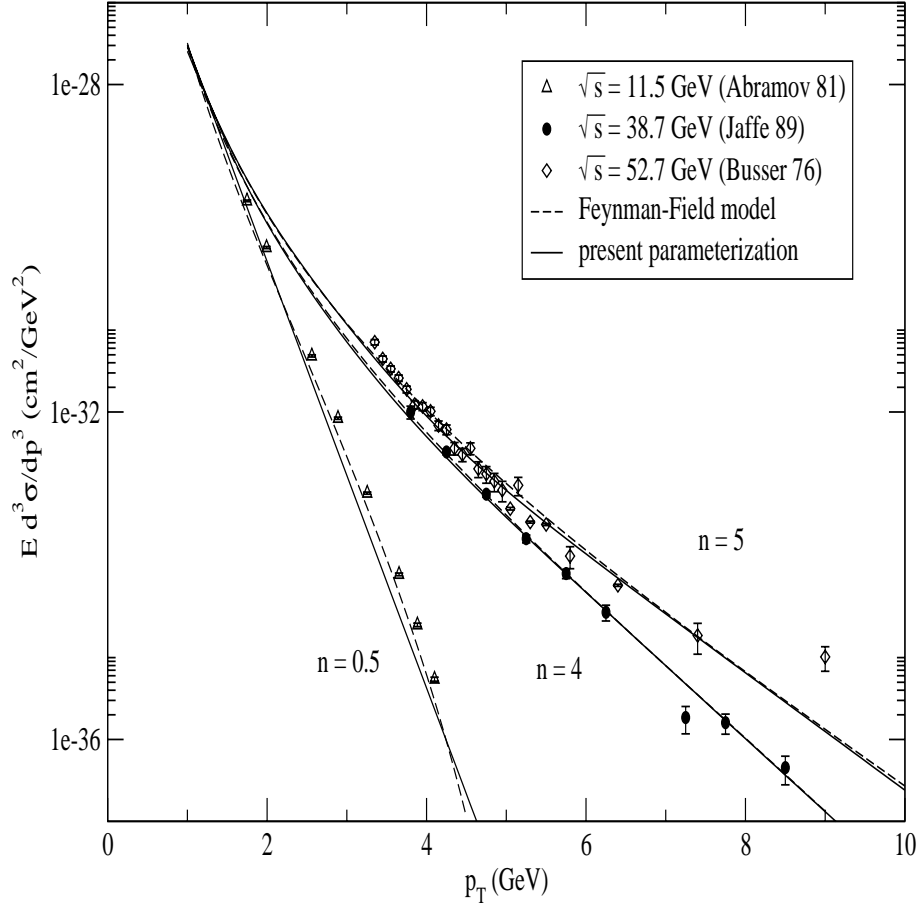


Figure 24: Comparisons of pQCD and parameterized cross sections with $pp \rightarrow \pi^+ X$ experimental data at $\bar{\theta}_{cm} = 90^\circ$. The parameter n in fragmentation functions of the Feynman-Field model are adjusted freely as shown in the graph to fit the data. The references of the data sets Abramov 81, Jaffe 89 and Busser 76 are ZETFP 33 304 (1981), PR D40 2777 (1989) and NP B1061 (1976) respectively.

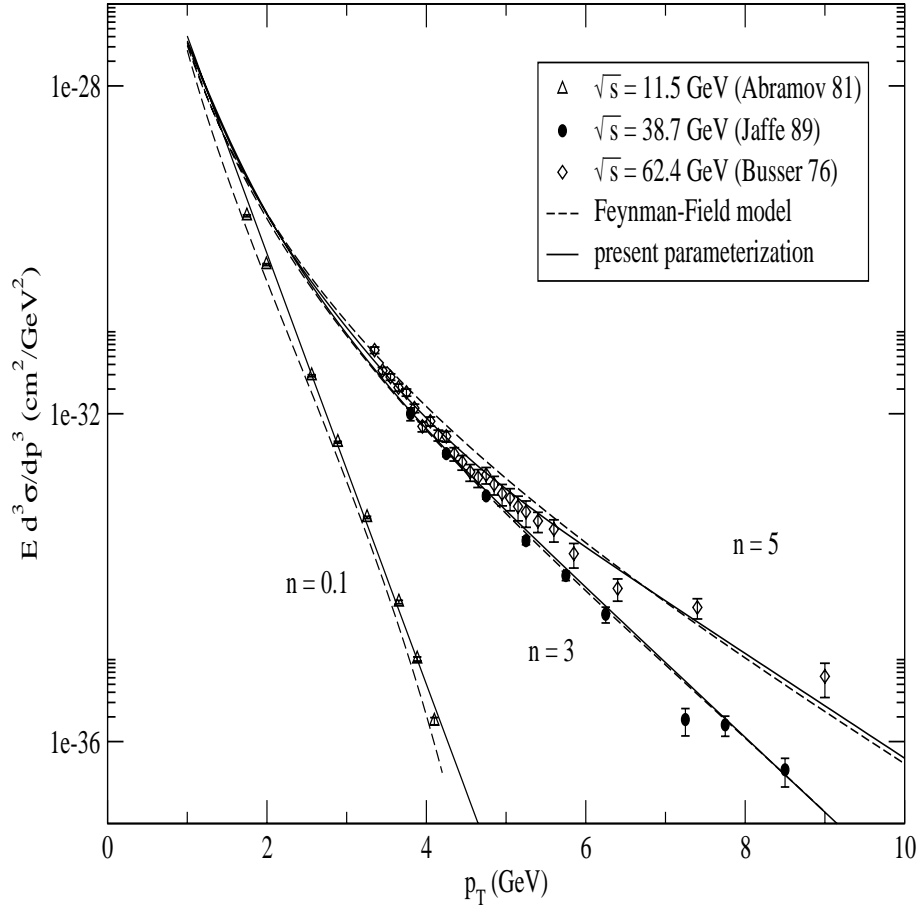


Figure 25: Comparisons of pQCD and parameterized cross sections with $pp \rightarrow \pi^- X$ experimental data at $\bar{\theta}_{cm} = 90^\circ$. The parameter n in fragmentation functions of the Feynman-Field model are adjusted freely as shown in the graph to fit the data. The references of the data sets Abramov 81, Jaffe 89 and Busser 76 are ZETFP 33 304 (1981), PR D40 2777 (1989) and NP B1061 (1976) respectively.

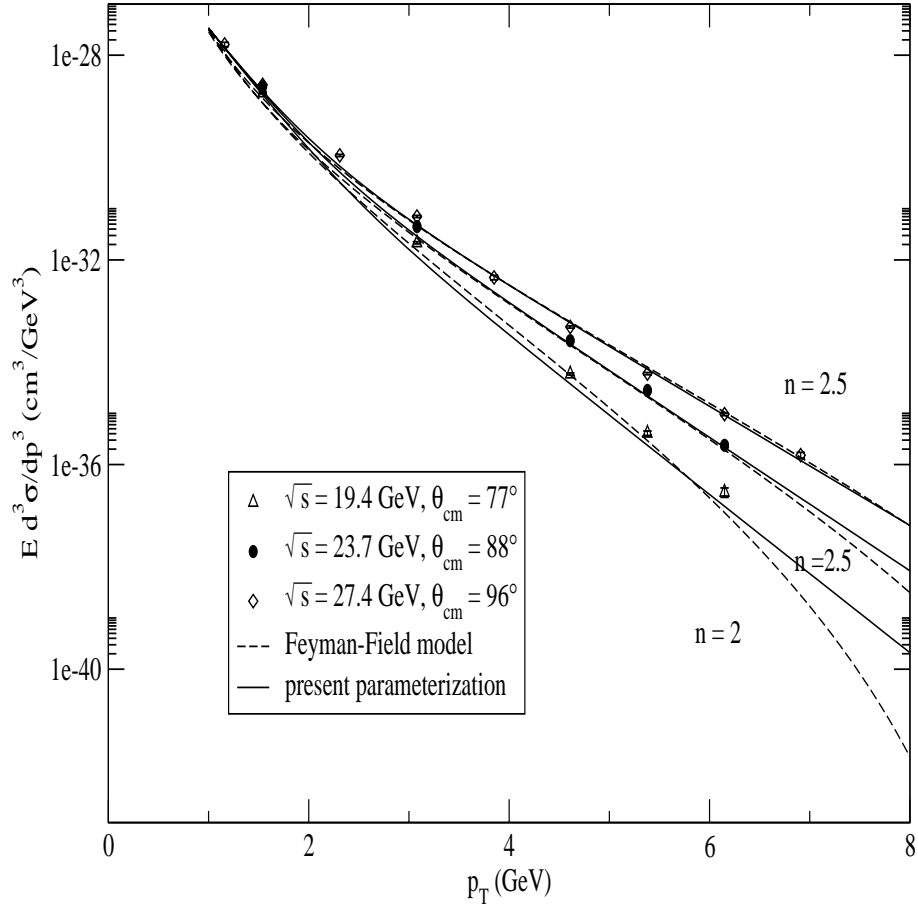


Figure 26: Comparisons pQCD and parameterized cross sections with $pp \rightarrow \pi^+ X$ experimental data at various energies and angles. The parameter n in fragmentation functions of the Feynman-Field model are adjusted freely as shown in the graph to fit the data. The experimental data set is produced by Antreasyan and published in PRL 38, 112 (1977).

Appendix A

MKN Theory of Bound States

A.1 NRSE in Momentum Space

Non-relativistic Schrödinger equation (NRSE) in configuration space has been solved exactly for some potentials, such as the Coulomb and simple harmonic oscillator potentials. NRSE with a linear potential can be solved analytically for the S -state only as we will show later. For $l > 0$, we resort to numerical methods. NRSE r -space codes are commonly known to be conditionally unstable [58, 59], while the momentum space codes do not have the same problem. The momentum space code has an additional advantage of being easily adaptable to relativistic equations. NRSE in momentum space takes the form

$$\frac{p^2}{2\mu} \phi(\mathbf{p}) + \int V(\mathbf{q}) \phi(\mathbf{p}') dp' = E \phi(\mathbf{p}), \quad (121)$$

where $\mathbf{q} = \mathbf{p} - \mathbf{p}'$.

Proof:

NRSE in momentum space can be derived from its configuration space counterpart

$$-\frac{\hbar^2}{2\mu} \nabla^2 \psi(\mathbf{x}) + V(\mathbf{x}) \psi(\mathbf{x}) = E \psi(\mathbf{x}) \quad (122)$$

by Fourier transform. First we define the following:

$$\phi(\mathbf{p}) = \int \psi(\mathbf{x}) e^{i\mathbf{k}\cdot\mathbf{x}} d^3x, \quad (123)$$

$$\psi(\mathbf{x}) = \int \phi(\mathbf{p})e^{-i\mathbf{k}\cdot\mathbf{x}}d^3p, \quad (124)$$

$$\mathbf{p} = \hbar\mathbf{k}, \quad (125)$$

and ignore factors of 2π in Fourier and inverse Fourier transforms. As usual, we assume periodic boundary condition or $\nabla\phi = \phi = 0$ at infinity. We Fourier-transform Eq. [122] term by term. The term on the right hand side of Eq. [122] is obtained simply by Eq. [123]. The first term involves $\nabla^2\psi$ and is transformed as

$$\begin{aligned} & \int \nabla^2\psi(\mathbf{x})e^{i\mathbf{k}\cdot\mathbf{x}}d^3x \\ &= \int \nabla\psi(\mathbf{x})e^{i\mathbf{k}\cdot\mathbf{x}}\cdot d\mathbf{S} - \int \nabla\psi(\mathbf{x})\cdot\nabla e^{i\mathbf{k}\cdot\mathbf{x}}d^3x \\ &= -i\mathbf{k}\cdot\int e^{i\mathbf{k}\cdot\mathbf{x}}\nabla\psi(\mathbf{x})d^3x \\ &= -i\mathbf{k}\cdot\left[\int\psi(\mathbf{x})e^{i\mathbf{k}\cdot\mathbf{x}}d\mathbf{S} - \int\psi(\mathbf{x})\nabla e^{i\mathbf{k}\cdot\mathbf{x}}d^3x\right] \\ &= -i\mathbf{k}\cdot\left[-i\mathbf{k}\int\psi(\mathbf{x})e^{i\mathbf{k}\cdot\mathbf{x}}d^3x\right] \\ &= -k^2\phi(\mathbf{p}). \end{aligned} \quad (126)$$

The second term involves $V(\mathbf{x})\psi(\mathbf{x})$. With Eq. [124], the second term of Eq. [122] is transformed as

$$\begin{aligned} \int V(\mathbf{x})\psi(\mathbf{x})e^{i\mathbf{k}\cdot\mathbf{x}}d^3x &= \int V(\mathbf{x})\left[\int\phi(\mathbf{p}')e^{-i\mathbf{k}'\cdot\mathbf{x}}d^3p'\right]e^{i\mathbf{k}\cdot\mathbf{x}}d^3x \\ &= \int\int V(\mathbf{x})\phi(\mathbf{p}')e^{i(\mathbf{k}-\mathbf{k}')\cdot\mathbf{x}}d^3x d^3p' \\ &= \int d^3p'\phi(\mathbf{p}')\int d^3x V(\mathbf{x})e^{i(\mathbf{k}-\mathbf{k}')\cdot\mathbf{x}} \\ &= \int V(\mathbf{p}-\mathbf{p}')\phi(\mathbf{p}')d^3p' \end{aligned} \quad (127)$$

At last, Eqs. [123], [126] and [127] are all needed to Fourier transform Eq. [122] into Eq. [121]. The proof is complete.

In this paper, we attempt to re-derive the results previously obtained by Maung *et al.* [33] in 1993. The power law potential in r space is given by

$$V^N(r) = \begin{cases} 0 & r < 0 \\ \lambda_N \lim_{\eta \rightarrow 0} r^N e^{-\eta r} & r \geq 0, \eta > 0 \end{cases}$$

Let $G = \hbar = c = 1$. Define $\mathbf{q} \equiv \mathbf{p} - \mathbf{p}'$. The momentum space potential can be obtained by Fourier transform.

$$V^N(\mathbf{q}) = \frac{1}{(2\pi)^3} \int_{-\infty}^{\infty} V^N(r) e^{i\mathbf{r}\cdot\mathbf{q}} d^3r \quad (128)$$

$$= \frac{\lambda_N}{(2\pi)^3} \lim_{\eta \rightarrow 0} \int_0^{\infty} \int_{-1}^1 \int_0^{2\pi} r^N e^{-\eta r} e^{irq \cos \theta} r^2 dr d\cos \theta d\phi \quad (129)$$

$$= \frac{\lambda_N}{4\pi^2} \frac{1}{iq} \lim_{\eta \rightarrow 0} \int_0^{\infty} \int_{-1}^1 r^{N+1} e^{-\eta r} e^{irq \cos \theta} dr d(\cos \theta) \quad (130)$$

$$= \frac{\lambda_N}{4\pi^2} \frac{1}{iq} \lim_{\eta \rightarrow 0} \int_0^{\infty} r^{N+1} e^{-\eta r} (e^{irq} - e^{-irq}) dr \quad (131)$$

$$= \frac{\lambda_N}{4\pi^2} \frac{1}{iq} \lim_{\eta \rightarrow 0} (-1)^{N+1} \frac{\partial^{N+1}}{\partial \eta^{N+1}} \int_0^{\infty} e^{-\eta r} (e^{irq} - e^{-irq}) dr \quad (132)$$

$$= \frac{\lambda_N}{4\pi^2} \frac{1}{iq} \lim_{\eta \rightarrow 0} (-1)^{N+1} \frac{\partial^{N+1}}{\partial \eta^{N+1}} \left[\frac{1}{\eta - iq} - \frac{1}{\eta + iq} \right] \quad (133)$$

$$= \frac{\lambda_N}{4\pi^2} \frac{1}{iq} \lim_{\eta \rightarrow 0} (-1)^{N+1} \frac{\partial^{N+1}}{\partial \eta^{N+1}} \left[\frac{2iq}{\eta^2 + q^2} \right] \quad (134)$$

The final form of the momentum space potential is

$$V^N(\mathbf{q}) = \frac{\lambda_N}{2\pi^2} \lim_{\eta \rightarrow 0} (-1)^{N+1} \frac{\partial^{N+1}}{\partial \eta^{N+1}} \left[\frac{1}{\eta^2 + q^2} \right], \quad (135)$$

where $N = -1$ corresponds to the Coulomb potential and $N = 1$ the linear potential. Together they give the Cornell potential

$$V(\mathbf{q}) \equiv V^C(\mathbf{q}) + V^L(\mathbf{q}) = V^{N=-1}(\mathbf{q}) + V^{N=1}(\mathbf{q}). \quad (136)$$

Next we want to perform a partial wave expansion of V^N . There are 3 useful formulas, the Wigner-Eckart Theorem[60]

$$\langle E'l'm'|T|Elm \rangle = \delta_{l'l} \delta_{m'm} T_l(E), \quad (137)$$

the addition of spherical harmonics

$$\sum_m Y_{lm}(\Omega) Y_{lm}^*(\Omega') = \frac{2l+1}{4\pi} P_l(\cos \theta), \quad (138)$$

and the orthogonality of spherical harmonics

$$\int d\Omega Y_{lm}^*(\Omega) Y_{l'm'}(\Omega) = \delta_{l'l} \delta_{m'm}, \quad (139)$$

which are used in deriving the following result.

$$\langle \mathbf{p} | V^N | \mathbf{p}' \rangle = \sum_{lm} \sum_{l'm'} \langle \mathbf{p} | lm \rangle \langle lm | V^N | l'm' \rangle \langle l'm' | \mathbf{p}' \rangle \quad (140)$$

$$= \sum_{lm} \sum_{l'm'} \langle p\Omega | lm \rangle \langle lm | V^N | l'm' \rangle \langle l'm' | p'\Omega' \rangle \quad (141)$$

$$= \sum_{lm} \sum_{l'm'} \langle p | \langle \Omega | lm \rangle \langle lm | V^N | l'm' \rangle \langle l'm' | \Omega' \rangle | p' \rangle \quad (142)$$

$$= \sum_{lm} \langle \Omega | lm \rangle \langle p | V_l^N | p' \rangle \langle lm | \Omega' \rangle \quad (143)$$

$$= \sum_{lm} V_l^N(p, p') Y_{lm}(\Omega) Y_{lm}^*(\Omega') \quad (144)$$

$$= \sum_l \frac{2l+1}{4\pi} V_l^N(p, p') P_l(\cos \theta) \quad (145)$$

In scattering and bound state problems, it is customary to expand the momentum space wavefunction $\phi(\mathbf{p})$ in partial waves, such that

$$\phi(\mathbf{p}) = \sum_{nlm} c_{nlm} \phi_{nl}(p) Y_{lm}(\Omega), \quad (146)$$

where c_{nlm} 's are coefficients of the expansion [p. 396 of Ref 1].

The non-relativistic Schrödinger equation in momentum space is given as

$$\left(\hat{E} - \frac{\mathbf{p}^2}{2\mu} \right) \phi(\mathbf{p}) = \int V^N(\mathbf{q}) \phi(\mathbf{p}') d^3 \mathbf{p}' \quad (147)$$

$$= \int \langle \mathbf{p} | V^N | \mathbf{p}' \rangle \phi(\mathbf{p}') d^3 \mathbf{p}' \quad (148)$$

Expand NRSE in partial waves.

$$\begin{aligned} & \left(\hat{E} - \frac{\mathbf{p}^2}{2\mu} \right) \sum_{nlm} c_{nlm} \phi_{nl}(p) Y_{lm}(\Omega) \\ &= \int p'^2 dp' d\Omega' \sum_{nlm} V_l^N(p, p') Y_{lm}(\Omega) Y_{lm}^*(\Omega') \sum_{n'l'm'} c_{n'l'm'} \phi_{n'l'}(p') Y_{l'm'}(\Omega') \end{aligned} \quad (149)$$

$$= \int p'^2 dp' \sum_{nlm} V_l^N(p, p') c_{nlm} \phi_{nl}(p') Y_{lm}(\Omega). \quad (150)$$

The nl -th terms can be separated by inspection with $\hat{E} \phi_{nl}(p) = E_{nl} \phi_{nl}(p)$. The partial wave NRSE is

$$\left(E_{nl} - \frac{p^2}{2\mu} \right) \phi_{nl}(p) = \int p'^2 dp' V_l^N(p, p') \phi_{nl}(p'). \quad (151)$$

Use the orthogonality of Legendre polynomials,

$$\int_{-1}^1 P_l(x)P_{l'}(x)dx = \frac{2}{2l+1}\delta_{ll'}, \quad (152)$$

and Eq. (145), we can calculate the potential matrix elements as follow.

$$\int_{-1}^1 \langle \mathbf{p}|V^N|\mathbf{p}' \rangle P_l(\cos \theta)d \cos \theta \quad (153)$$

$$= \sum_{l'} \frac{2l'+1}{4\pi} V_{l'}^N(p, p') \int_{-1}^1 P_l(\cos \theta)P_{l'}(\cos \theta)d \cos \theta \quad (154)$$

$$= \sum_{l'} \frac{1}{2\pi} V_{l'}^N(p, p')\delta_{ll'} \quad (155)$$

$$= \frac{1}{2\pi} V_l^N(p, p') \quad (156)$$

In order words,

$$V_l^N(p, p') = 2\pi \int_{-1}^1 V^N(\mathbf{q})P_l(\cos \theta)d \cos \theta. \quad (157)$$

Define

$$y \equiv \frac{p^2 + p'^2 + \eta^2}{2p'p}, \quad (158)$$

and use the definition of the Legendre polynomial of the second kind $Q_n(z)$,

$$Q_n(z) = \frac{1}{2} \int_{-1}^1 \frac{1}{z-t} P_n(t)dt, \quad (159)$$

we can modify Eq. (157) as

$$V_l^N(p, p') = 2\pi \int_{-1}^1 V^N(\mathbf{q})P_l(\cos \theta)d \cos \theta \quad (160)$$

$$= \frac{\lambda_N}{\pi} \lim_{\eta \rightarrow 0} \frac{\partial^{N+1}}{\partial \eta^{N+1}} \int_{-1}^1 \frac{1}{q^2 + \eta^2} P_l(\cos \theta)d \cos \theta \quad (161)$$

$$= \frac{\lambda_N}{\pi} \lim_{\eta \rightarrow 0} \frac{\partial^{N+1}}{\partial \eta^{N+1}} \int_{-1}^1 \frac{1}{p^2 + p'^2 - 2p'p \cos \theta + \eta^2} P_l(\cos \theta)d \cos \theta \quad (162)$$

$$= \frac{\lambda_N}{\pi} \lim_{\eta \rightarrow 0} \frac{\partial^{N+1}}{\partial \eta^{N+1}} \int_{-1}^1 \frac{1}{2p'p(y - \cos \theta)} P_l(\cos \theta)d \cos \theta \quad (163)$$

$$= \frac{\lambda_N}{\pi} \lim_{\eta \rightarrow 0} \frac{\partial^{N+1}}{\partial \eta^{N+1}} \frac{Q_l(y)}{p'p}. \quad (164)$$

The coulomb potential corresponds to $N = -1$ and has the form

$$V_l^C(p, p') = \frac{\lambda_C}{\pi} \lim_{\eta \rightarrow 0} \frac{Q_l(y)}{p'p}. \quad (165)$$

The linear potential corresponds to $N = 1$ and has the form

$$V_l^L = \frac{\lambda_L}{\pi} \lim_{\eta \rightarrow 0} \frac{\partial^2}{\partial \eta^2} \frac{Q_l(y)}{p'p} \quad (166)$$

$$= \frac{\lambda_L}{\pi} \lim_{\eta \rightarrow 0} \frac{\partial}{\partial \eta} \left[\frac{\eta}{(p'p)^2} Q_l'(y) \right] \quad (167)$$

$$= \frac{\lambda_L}{\pi} \lim_{\eta \rightarrow 0} \left[\frac{Q_l'(y)}{(p'p)^2} + \frac{\eta^2}{(p'p)^3} Q_l''(y) \right]. \quad (168)$$

There are 3 useful relations in terms of Legendre polynomials of the 2nd kind [40]:

$$Q_0(y) = \frac{1}{2} \ln \left| \frac{y+1}{y-1} \right|, \quad (169)$$

$$Q_l(y) = P_l(y)Q_0(y) - w_{l-1}(y), \quad (170)$$

$$w_{l-1}(y) = \sum_{m=1}^l \frac{1}{m} P_{l-m}(y) P_{m-1}(y). \quad (171)$$

The singularities of $V_l^C(p, p')$ and $V_l^L(p, p')$ come from the singularities of $Q_l(y)$ and $Q_l''(y)$. From Eq. (170), it is obvious that the singularities of $Q_l(y)$ and $Q_l''(y)$ again come from those of $Q_0(y)$, $Q_0'(y)$ and $Q_0''(y)$. In order to treat the singularities of the momentum space Cornell potential, we need to control the singularities of $Q_0(y)$, $Q_0'(y)$ and $Q_0''(y)$ first and foremost. Substitute Eq. (158) into Eq. (169), we have

$$Q_0(y) = \frac{1}{2} \ln \left[\frac{(p+p')^2 + \eta^2}{(p-p')^2 + \eta^2} \right]. \quad (172)$$

Differentiating Eq. (172) yields

$$Q_0'(y) = \frac{1}{2} \frac{\partial}{\partial y} \ln \left| \frac{y+1}{y-1} \right| \quad (173)$$

$$= \frac{1}{2} \left[\frac{1}{y+1} - \frac{1}{y-1} \right] \quad (174)$$

$$= \frac{1}{1-y^2} \quad (175)$$

$$= p'p \left[\frac{1}{(p+p')^2 + \eta^2} - \frac{1}{(p-p')^2 + \eta^2} \right] \quad (176)$$

Differentiating again gives

$$Q_0''(y) = \frac{2y}{(1-y^2)^2} \quad (177)$$

$$= \frac{p^2 + p'^2 + \eta^2}{p'p} \left[p'p \left(\frac{1}{(p+p')^2 + \eta^2} - \frac{1}{(p-p')^2 + \eta^2} \right) \right]^2, \quad (178)$$

or

$$\frac{\eta^2}{p'p} Q_0''(y) = \eta^2 (p^2 + p'^2 + \eta^2) \left[\frac{1}{(p+p')^2 + \eta^2} - \frac{1}{(p-p')^2 + \eta^2} \right]^2. \quad (179)$$

There are two useful identities which we want to prove:

$$\int_0^\infty \frac{1}{p'} Q_0(y, \eta = 0) dp' = \frac{\pi^2}{2}, \quad (180)$$

$$\int_0^\infty \left[\frac{\eta^2}{p'p} Q_0''(y) + Q_0'(y) \right] dp' = 0. \quad (181)$$

Proof:

The integral in Eq. [180] is derived as follow:

$$\int_0^\infty \frac{1}{p'} Q_0(y, \eta = 0) dp' \quad (182)$$

$$= \frac{1}{2} \int_0^\infty \frac{1}{p'} \ln \left(\frac{p+p'}{p-p'} \right)^2 dp' \quad (183)$$

$$= \frac{1}{2} \left[\int_0^a \frac{1}{x} \ln \left(\frac{x+a}{x-a} \right)^2 dx + \int_a^\infty \frac{1}{x} \ln \left(\frac{x+a}{x-a} \right)^2 dx \right] \quad (184)$$

$$= \int_a^\infty \frac{1}{x} \ln \left(\frac{a+x}{a-x} \right) dx + \int_a^\infty \frac{1}{x} \ln \left(\frac{x+a}{x-a} \right) dx \quad (185)$$

$$= - \int_\infty^0 \frac{1}{ae^{-u}} \ln \left(\frac{a+ae^{-u}}{a-ae^{-u}} \right) ae^{-u} du + \int_0^\infty \frac{1}{ae^u} \ln \left(\frac{ae^u+a}{ae^u-a} \right) ae^u du \quad (186)$$

$$= 2 \left[\int_0^\infty \ln \left(\frac{1+e^{-u}}{1-e^{-u}} \right) du \right] \quad (187)$$

$$= 2 \left[\int_0^\infty \ln(1+e^{-u}) du - \int_0^\infty \ln(1-e^{-u}) du \right] \quad (188)$$

$$= 2 \left[\frac{\pi^2}{12} + \frac{\pi^2}{6} \right] \quad (189)$$

$$= \frac{\pi^2}{2} \quad (190)$$

The results of Eq. [189] come from relations BI((256))(10) and BI((256))(11) in Gradshteyn and Ryzhik [61].

Eq. [176] has 4 simple poles: $\alpha = p + i\eta$, α^* , $\beta = -p + i\eta$ and β^* . $Q'_0(y)$ can be rewritten as

$$Q'_0(y) = p'p \left[\frac{-1}{(p' - \alpha)(p' - \alpha^*)} + \frac{1}{(p' - \beta)(p' - \beta^*)} \right] \quad (191)$$

The contour integral $\oint Q'_0(y)dz$ over the upper complex plane has 2 residues: $Res(\alpha)$ and $Res(\beta)$. Use the formula $Res(z_0) = \lim_{z \rightarrow z_0} (z - z_0)f(z)$ to calculate these residues,

$$Res(\alpha) = \lim_{p' \rightarrow \alpha} p'p \left[\frac{-1}{p' - \alpha^*} + \frac{p' - \alpha}{(p' - \beta)(p' - \beta^*)} \right] \quad (192)$$

$$= -p(p + i\eta) \left[\frac{1}{2i\eta} + 0 \right] \quad (193)$$

$$= -\frac{p(p + i\eta)}{2i\eta}, \quad (194)$$

$$Res(\beta) = \lim_{p' \rightarrow \beta} p'p \left[\frac{-(p' - \beta)}{(p' - \alpha)(p' - \alpha^*)} + \frac{1}{(p' - \beta^*)} \right] \quad (195)$$

$$= p(-p + i\eta) \left[0 + \frac{1}{2i\eta} \right] \quad (196)$$

$$= \frac{p(-p + i\eta)}{2i\eta}, \quad (197)$$

$$Res(\alpha) + Res(\beta) = -\frac{p(p + i\eta)}{2i\eta} + \frac{p(-p + i\eta)}{2i\eta} \quad (198)$$

$$= -\frac{p^2}{i\eta}. \quad (199)$$

Since the contour at infinity is zero and $Q'_0(y)$ along the real axis is symmetric around the origin, we obtain

$$\int_0^\infty Q'_0(y) dp' = \frac{1}{2} \oint Q'_0(y) dz \quad (200)$$

$$= \frac{1}{2} \left(2\pi i \sum Res \right) \quad (201)$$

$$= -\frac{\pi p^2}{\eta}. \quad (202)$$

$(\eta^2/p'p)Q_0''(y)$ has the same poles as $Q_0'(y)$ but of order 2. Residues of order m are calculated by the formula

$$Res(z_0) = \lim_{z \rightarrow z_0} \frac{1}{(m-1)!} \frac{d^{m-1}}{dz^{m-1}} (z - z_0)^m f(z). \quad (203)$$

Again we can simplify the algebra by rewriting Eq. [181] as

$$\frac{\eta^2}{p'p} Q_0''(y) = \eta^2 (p^2 + p'^2 + \eta^2) \left[\frac{-1}{(p' - \alpha)(p' - \alpha^*)} + \frac{1}{(p' - \beta)(p' - \beta^*)} \right]^2. \quad (204)$$

The residues are

$$\begin{aligned} & Res(\alpha) \\ &= \lim_{p' \rightarrow \alpha} \frac{d}{dp'} \eta^2 (p^2 + p'^2 + \eta^2) \left[\frac{-1}{(p' - \alpha^*)} + \frac{p' - \alpha}{(p' - \beta)(p' - \beta^*)} \right]^2 \end{aligned} \quad (205)$$

$$= \eta^2 \left\{ 2(p + i\eta) \left[\frac{-1}{2i\eta} \right]^2 + 4p(p + i\eta) \left[\frac{-1}{2i\eta} \right] \left[\frac{1}{(2i\eta)^2} + \frac{1}{2p(2p + 2i\eta)} \right] \right\} \quad (206)$$

$$= \frac{\eta^2}{2} \left\{ -\frac{p}{\eta^2} - \frac{i}{\eta} + \frac{p^2}{i\eta^3} + \frac{p}{\eta^2} - \frac{1}{i\eta} \right\} \quad (207)$$

$$= \frac{p^2}{2i\eta}, \quad (208)$$

$$\begin{aligned} & Res(\beta) \\ &= \lim_{p' \rightarrow \beta} \frac{d}{dp'} \eta^2 (p^2 + p'^2 + \eta^2) \left[\frac{-(p' - \beta)}{(p' - \alpha)(p' - \alpha^*)} + \frac{1}{p' - \beta^*} \right]^2 \end{aligned} \quad (209)$$

$$= \eta^2 \left\{ 2(p - i\eta) \left[\frac{1}{2i\eta} \right]^2 + 4p(p - i\eta) \left[\frac{1}{2i\eta} \right] \left[\frac{-1}{(2i\eta)^2} + \frac{1}{2p(-2p + 2i\eta)} \right] \right\} \quad (210)$$

$$= \frac{\eta^2}{2} \left\{ \frac{p}{\eta^2} - \frac{i}{\eta} + \frac{p^2}{i\eta^3} - \frac{p}{\eta^2} - \frac{1}{i\eta} \right\} \quad (211)$$

$$= \frac{p^2}{2i\eta}. \quad (212)$$

Hence the sum of residues is

$$Res(\alpha) + Res(\beta) = \frac{p^2}{2i\eta} + \frac{p^2}{2i\eta} \quad (213)$$

$$= \frac{p^2}{i\eta} \quad (214)$$

Since $(\eta^2/p'p)Q_0''(y)$ is symmetric around the origin, we can integrate along the same contour as before and obtain

$$\int_0^\infty \frac{\eta^2}{p'p} Q_0''(y) dp' = \frac{1}{2} \oint \frac{\eta^2}{pz} Q_0''(y) dz \quad (215)$$

$$= \frac{1}{2} \left(2\pi i \sum Res \right) \quad (216)$$

$$= \frac{\pi p^2}{\eta}. \quad (217)$$

From these results, it is obvious that Eq. [181] is true. The proof is complete.

A simple example is the momentum space Schrödinger equation with a linear potential in the S -state [33, 35],

$$\frac{p^2}{2\mu} \phi_{n0}(p) + \frac{\lambda_L}{\pi p^2} \int_0^\infty \underbrace{\left[\frac{\eta^2}{p'p} Q_0''(y) + Q_0'(y) \right]}_{V_0^L(p,p')} \phi_{n0}(p') dp' = E_{n0} \phi_{n0}(p), \quad (218)$$

where $y = (p^2 + p'^2)/2p'p$. Lande subtraction [33, 35] involves subtracting a zero term

$$\int_0^\infty \left[\frac{\eta^2}{p'p} Q_0''(y) + Q_0'(y) \right] dp' = 0 \quad (219)$$

from Eq. [218] such that

$$\frac{p^2}{2\mu} \phi_{n0}(p) + \frac{\lambda_L}{\pi p^2} \int_0^\infty \left[\frac{\eta^2}{p'p} Q_0''(y) + Q_0'(y) \right] [\phi_{n0}(p') - \phi_{n0}(p)] dp' = E_{n0} \phi_{n0}(p). \quad (220)$$

Using Eqs. [176,179], the integral in Eq. [220] for $p > 0$ in the limit of $y \rightarrow 1$ can be shown to equal

$$\lim_{\eta \rightarrow 0} \lim_{p \rightarrow p'} \frac{\lambda_L}{\pi} \left[2\eta^2 \left(\frac{1}{(p-p')^2 + \eta^2} \right)^2 - \frac{1}{(p-p')^2 + \eta^2} \right] (p-p')^2 \frac{d\phi_{n0}}{dp} = 0. \quad (221)$$

The order of the limits in Eq. [221] is important. The reverse order will lead to the nonsensical result $\int Q_0'(y) dp' = 0$. Next, in the limit of $p, p' \rightarrow 0$, $(p+p')^2 = (p-p')^2$. By substituting this equality into Eqs. [176,179], it can be shown again that the integral in Eq. [220] vanishes for $p \rightarrow 0$ at $y = 1$. At the end, the integral vanishes at $y = 1$, $\forall p$. Away from the singularities, both integrands in the integral of Eq. [220]

are finite. By taking $\eta \rightarrow 0$, the first integrand vanishes. The final form of Eq. [220] is

$$\frac{p^2}{2\mu} \phi_{n0}(p) + \frac{\lambda_L}{\pi p^2} \int_0^\infty Q'_0(y) [\phi_{n0}(p') - \phi_{n0}(p)] dp' = E_{n0} \phi_{n0}(p), \quad (222)$$

where $Q'_0(y) = 1/(1-y^2)$.

The momentum space NRSE with a coulomb potential is given as

$$\frac{p^2}{2\mu} \phi_{nl}(p) + \frac{\lambda_C}{\pi p} \int_0^\infty P_l(y) \frac{Q_0(y)}{p'} \phi_{nl}(p') p'^2 dp' - \frac{\lambda_C}{\pi p} \int_0^\infty w_{l-1}(y) \phi_{nl}(p') p' dp' = E_{nl} \phi_{nl}(p). \quad (223)$$

Use Eq. [180] to subtract out the logarithmic singularity and obtain

$$\begin{aligned} \frac{p^2}{2\mu} \phi_{nl}(p) + \frac{\lambda_C}{\pi p} \int_0^\infty P_l(y) \frac{Q_0(y)}{p'} \left[p'^2 \phi_{nl}(p') - \frac{p^2 \phi_{nl}(p)}{P_l(y)} \right] dp' + \frac{\lambda_C}{\pi p} \left[\frac{\pi^2}{2} p^2 \phi_{nl}(p) \right] \\ - \frac{\lambda_C}{\pi p} \int_0^\infty w_{l-1}(y) \phi_{nl}(p') p' dp' = E_{nl} \phi_{nl}(p). \end{aligned} \quad (224)$$

Before we perform Lande subtraction on the NRSE with a confining potential, we need the identity

$$P'_l(1) = \frac{l(l+1)}{2}. \quad (225)$$

Proof:

We use the recursion relation $xP'_x - P'_{l-1}(x) = lP_l(x)$, the equality $P_l(1) = 1$ to obtain the following relations:

$$\begin{aligned} P'_l(1) - P'_{l-1}(1) &= l \\ P'_{l-1}(1) - P'_{l-2}(1) &= l-1 \\ &\vdots \\ P'_2(1) - P'_1(1) &= 2 \\ P'_1(1) - P'_0(1) &= 1. \end{aligned} \quad (226)$$

Add these relations and use $P_0(x) = 1$ or $P'_0(x) = 0$, we prove Eq. [225]. Next we want to examine the singularities of $Q'_l(y)$ and $Q''_l(y)$. Differentiating Eq. [170] once and twice, we have

$$Q'_l = P'_l Q_0 + P_l Q'_0 - w'_{l-1}, \quad (227)$$

$$Q''_l = P''_l Q_0 + 2P'_l Q'_0 + P_l Q''_0 - w''_{l-1}. \quad (228)$$

$\eta^2 P_l'' Q_0$, $\eta^2 P_l' Q_0'$ and $\eta^2 w_{l-1}''$ vanish in the limit of $\eta \rightarrow 0$. The momentum space confining potential is

$$V_l^L(p', p) = \frac{\lambda_L}{\pi} \lim_{\eta \rightarrow 0} \left\{ P_l(y) \left[\frac{\eta^2}{(p'p)^3} Q_0''(y) + \frac{Q_0'(y)}{(p'p)^2} \right] + \frac{P_l'(y) Q_0(y) - w_{l-1}'(y)}{(p'p)^2} \right\}. \quad (229)$$

Lastly, perform Lande subtraction and use Eq. [225]. Take the limit of $\eta = 0$, we derive the momentum space NRSE with a confining potential as

$$\begin{aligned} & \frac{p^2}{2\mu} \phi_{nl}(p) + \frac{\lambda_L}{\pi p^2} \int_0^\infty P_l(y) Q_0'(y) \left[\phi_{nl}(p') - \frac{\phi_{nl}(p)}{P_l(y)} \right] dp' \\ & + \frac{\lambda_L}{\pi p^2} \int_0^\infty P_l'(y) \frac{Q_0(y)}{p'} \left[p' \phi_{nl}(p') - \frac{l(l+1)p \phi_{nl}(p)}{2 P_l'(y)} \right] dp' \\ & + \frac{\lambda_L}{\pi p^2} \frac{l(l+1)}{2} \left[\frac{\pi^2}{2} p \phi_{nl}(p) \right] + \frac{\lambda_L}{\pi p^2} \int_0^\infty w_{l-1}'(y) \phi_{nl}(p') dp' = E_{nl} \phi_{nl}(p). \end{aligned} \quad (230)$$

A.2 Exact Solution of NRSE with a Linear Potential

In the next section, we are going to solve the NRSE numerically with a linear potential. In this section, we will solve the same equation exactly so that we can use the analytic results to check their numerical counterparts. The Hamiltonian equation can be written as

$$\left(\frac{d^2}{dr^2} + \frac{2}{r} \frac{d}{dr} \right) R - 2\mu[\lambda_L r - E] R = 0. \quad (231)$$

Let $S \equiv r R$, then Eq. [231] can be simplified as

$$\frac{d^2}{dr^2} S - 2\mu[\lambda_L r - E] S = 0. \quad (232)$$

If we define as new variable

$$x \equiv \left(\frac{2\mu^2}{\lambda_L} \right)^{\frac{1}{3}} [\lambda_L r - E], \quad (233)$$

Eq. [233] can be transformed as

$$S'' - xS = 0, \quad (234)$$

which is the Airy equation. The solution which satisfies the boundary condition of $S \rightarrow 0$ as $x \rightarrow \infty$ is the Airy function $\text{Ai}(x)$. Fig. [27] illustrates the graph of the Airy function. By noticing that $S \equiv rR$ vanishes at $r = 0$, we infer that $S(r = 0)$ must coincide with a zero of $\text{Ai}(x)$. It is made possible by letting the eigen-energy act as a horizontal shift which shifts the origin to the left along the x -axis. If S is plotted against r instead of x , S will vanish at the origin if E_n is chosen appropriately. This conclusion leads to the eigen-energy formula

$$E_n = -x_n \left(\frac{\lambda_L^2}{2\mu} \right)^{\frac{1}{3}}, \quad (235)$$

where x_n is the n -th zero of the Airy function counting from $x = 0$ along $-x$.

In Norbury *et. al.*'s [35] paper, the values $\lambda_L = 5$ and $\mu = 0.75$ are used. The eigen-energy formula is

$$E_n = -2.554364772 x_n. \quad (236)$$

Table 6 lists the zeros of the Airy function and the corresponding exact eigen-energies.

A.3 Summary

The p -space formalism shown in this paper can be applied to any arbitrary potential in principle although only the cases of $n = -1, 1$ in r^n are considered in this paper. More complicated potentials require the calculation of integrals involving other powers of r . The potential involving the coupling constant $\alpha(r)$ in QCD near the asymptotic freedom region is such an example. In these cases, we may need to rely on numerical integration to evaluate the integrals of the Lande subtraction terms.

Table 6: Zeros of the Airy function and the corresponding eigen-energies in GeV for $l = 0$, $\mu = 0.75$ GeV, $\lambda_L = 5$ GeV.

n	x_n	E_n
1	-2.33810741	5.972379202
2	-4.08794944	10.44211404
3	-5.52055983	14.10152355
4	-6.78670809	17.33572806
5	-7.94413359	20.29221499
6	-9.02265085	23.04714148
7	-10.04017434	25.64626764
8	-11.00852430	28.11978666
9	-11.93601556	30.48893766
10	-12.82877675	32.76937540

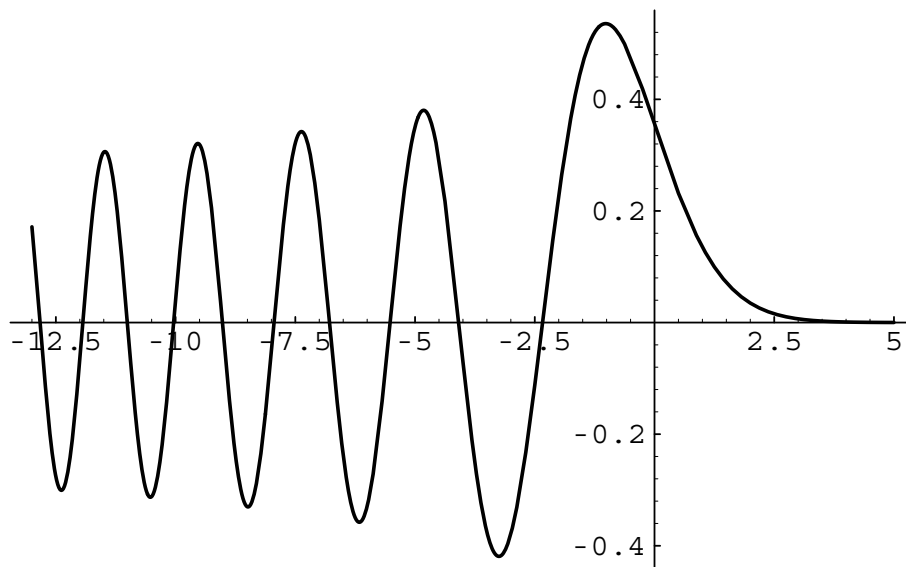


Figure 27: The graph of the Airy function—The zeros are all negative. Since $S = r R$, S must be zero at the origin $r = 0$. The eigen-energy acts like a horizontal shift which shifts the origin back to a zero.

Appendix B

The Area Law of the Lund Model

B.1 Kinematics

The quark-antiquark pair of a meson is massless in the string model. In this case, the concept of the mass of a meson is associated with the mass of the string field and not the quarks. Massless quarks move at the speed of light. It is not a surprising result given the fact that string theory predicts that the ends of open strings move at the speed of light either by imposing a Neumann boundary condition for open strings [63] or by solving the classical equations of motion [64]. In the highly relativistic problems, the light-cone coordinates are the natural choice. In the $(1 + 1)$ case, Lorentz transformations can be written as

$$\begin{pmatrix} E' \\ p' \end{pmatrix} = \begin{pmatrix} \gamma & -\gamma v \\ -\gamma v & \gamma \end{pmatrix} \begin{pmatrix} E \\ p \end{pmatrix} \equiv \begin{pmatrix} \cosh y & -\sinh y \\ -\sinh y & \cosh y \end{pmatrix} \begin{pmatrix} E \\ p \end{pmatrix}, \quad (237)$$

$$\begin{pmatrix} t' \\ x' \end{pmatrix} = \begin{pmatrix} \gamma & -\gamma v \\ -\gamma v & \gamma \end{pmatrix} \begin{pmatrix} t \\ x \end{pmatrix} \equiv \begin{pmatrix} \cosh y & -\sinh y \\ -\sinh y & \cosh y \end{pmatrix} \begin{pmatrix} t \\ x \end{pmatrix}, \quad (238)$$

where γ is the Lorentz factor

$$\gamma = \frac{1}{\sqrt{1 - v^2}}. \quad (239)$$

These equations imply

$$\gamma = \cosh y_p, \quad (240)$$

$$\gamma v = \sinh y_p, \quad (241)$$

$$v = \tanh y_p. \quad (242)$$

The energy and momentum of a particle can now be written as

$$E = \gamma m = m \cosh y_p, \quad (243)$$

$$p = \gamma m v = m \sinh y_p. \quad (244)$$

The boosted energy E_b and the boosted 1-momentum p_b are given as

$$\begin{aligned} E_b &= \gamma(E - v p) \\ &= m(\cosh y_p \cosh y - \sinh y_p \sinh y) \\ &= m \cosh(y_p - y), \end{aligned} \quad (245)$$

$$\begin{aligned} p_b &= \gamma(p - v E) \\ &= m(\sinh y_p \cosh y - \cosh y_p \sinh y) \\ &= m \sinh(y_p - y). \end{aligned} \quad (246)$$

The relativistic velocity addition formula is simple in light-cone coordinates [49],

$$v' = \tanh y' = \frac{v - v_b}{1 - v_b v} = \tanh(y - y_b), \quad (247)$$

illustrating the additivity of rapidity,

$$y = y' + y_b. \quad (248)$$

This simplification motivates the definition of rapidity

$$y_p = \frac{1}{2} \ln \left(\frac{1 + v}{1 - v} \right) = \frac{1}{2} \ln \left(\frac{E + p}{E - p} \right). \quad (249)$$

Momenta along the light-cone can be defined as [49]

$$p_+ = E + p = m \cosh y_p + m \sinh y_p = m e^{y_p}, \quad (250)$$

$$p_- = E - p = m \cosh y_p - m \sinh y_p = m e^{-y_p}. \quad (251)$$

With these definitions, boosts are simplified along the light-cone [49],

$$p'_\pm = m e^{\pm(y_p - y)} = p_\pm e^{\mp y}. \quad (252)$$

Light-cone coordinates can also be defined in configuration space as

$$t \equiv \frac{m}{\kappa} \cosh y_q, \quad (253)$$

$$x \equiv \frac{m}{\kappa} \sinh y_q, \quad (254)$$

where κ is the string constant and is used here to give t and x the correct dimension. A new subscript is adopted for y_q in configuration space to distinguish y_p in momentum space. These definitions are consistent with the requirement that $v = dx/dt = \tanh y_q$, as in Eq. (242). Similar results are obtained as in the momentum space case,

$$x_+ = t + x = \frac{m}{\kappa} \cosh y_q + \frac{m}{\kappa} \sinh y_q = \frac{m}{\kappa} e^{y_q}, \quad (255)$$

$$x_- = t - x = \frac{m}{\kappa} \cosh y_q - \frac{m}{\kappa} \sinh y_q = \frac{m}{\kappa} e^{-y_q}, \quad (256)$$

$$x'_\pm = \frac{m}{\kappa} e^{\pm(y_q - y)} = x_\pm e^{\mp y}. \quad (257)$$

B.2 Deriving the Area Law

The focus of this paper is primarily mesons. The force field between a quark-antiquark pair is presumed to be constant and confined to a flux-tube. The equation of motion of any one member of the quark-antiquark pair acted upon by a constant force is [49]

$$F = \frac{dp}{dt} = -\kappa, \quad (258)$$

where κ is the string constant. The solution of the equation is [49]

$$p(t) = p_0 - \kappa t = \kappa(t_0 - t). \quad (259)$$

From $E^2 = p^2 + m^2$, $E dE = p dp$ or

$$\frac{p}{E} = \frac{dE}{dp} \quad (260)$$

is obtained. There is also

$$p = \gamma m v = \gamma m \frac{dx}{dt} = E \frac{dx}{dt}. \quad (261)$$

Together, Eqs. (260) and (261) yield [49]

$$\frac{dx}{dt} = \frac{p}{E} = \frac{dE}{dp}, \quad (262)$$

such that [49]

$$\frac{dE}{dx} = \frac{dE}{dp} \frac{dp}{dt} \frac{dt}{dx} = \frac{dp}{dt} = -\kappa. \quad (263)$$

Its solution gives the expected QCD flux tube result [49]

$$E = \kappa(x_0 - x). \quad (264)$$

Combining Eqs. (259) and (264) and $m = 0$, the relativistic equation of state is [49]

$$m^2 = E^2 - p^2 = \kappa[(x_0 - x)^2 - (t_0 - t)^2] = 0. \quad (265)$$

Let $x_0 = t_0 = 0$, the equation of motion $|x| = t$ is obtained. The maximum kinetic energy at $x = 0$ puts an upper bound on the displacement of the particle such that $\kappa x_{max} = W$. The path of the particle is illustrated in Figure 28. The zig-zag motion of the particle is the reason for the name “yoyo state.” The quark-antiquark pair of a meson are assumed to be massless. The mass square of the meson is proportional to the area of the rectangle defined by the trajectories of the quark-antiquark pair. The period τ of the yoyo motion is [49]

$$\tau = \frac{2E_0}{\kappa}, \quad (266)$$

where E_0 is the maximum kinetic energy of each quark. In a boosted Lorentz frame, the period is transformed as [49]

$$\tau' = \tau \cosh y. \quad (267)$$

The breakup of a string occurs along a curve of constant proper time such that the process is Lorentz invariant. The Lund model assumes that the produced mesons are ranked, meaning that the production of the n -th rank meson depends on the existence of rank $n - 1$, $n - 2$, \dots , 1 mesons. A vertex V is a breakup point and the location $\kappa(x_+, x_-)$ where a quark-antiquark pair is produced. The breakup of a string is represented in Figure 29. The produced particle closer to the edges are the faster moving ones, corresponding to larger rapidities.

Let $p_{\pm 0}$ and $p_{\pm j}$ be momentum of the parent quark and the j -th of the n produced quarks moving along the x_{\pm} light-cone coordinate respectively. Then [49]

$$p_{\pm 0} = \sum_{j=1}^n p_{\pm j}, \quad (268)$$

and the momentum fraction at V_j is defined as [49]

$$z_{\pm j} = \frac{p_{\pm j}}{p_{\pm 0}}. \quad (269)$$

In order to simplify notations, $z_j = z_{+j}$ unless specified otherwise. The invariant interval is

$$ds^2 = dt^2 - dx^2 = dt^2(1 - v^2), \quad (270)$$

giving

$$ds = dt\sqrt{1 - v^2} = \frac{dt}{\gamma} = d\tau, \quad (271)$$

where τ is the proper time. The proper time is also $x_+x_- = (t-x)(t+x) = t^2 - x^2 = \tau^2$ and can be used as dynamic variable such that [49]

$$\Gamma = \kappa^2 x_+x_-. \quad (272)$$

Since Γ is proportional to the proper time square τ^2 , its Lorentz invariant property makes it a good kinematic variable in the light-cone coordinates. Let $W_{\pm 1}$ and $W_{\pm 2}$ be the kinetic energies along x_{\pm} at vertices 1 and 2 respectively. The following identities can be easily proven geometrically by calculating the areas of the rectangles $\Gamma_1 = A_1 + A_3$, $\Gamma_2 = A_2 + A_3$ and m^2 as shown in Figure 30 [49],

$$\Gamma_1 = (1 - z_-)W_{-2}W_{+1}, \quad (273)$$

$$\Gamma_2 = (1 - z_+)W_{-2}W_{+1}, \quad (274)$$

$$m^2 = z_-z_+W_{-2}W_{+1}, \quad (275)$$

where m is the mass of the produced meson. Eqs. (273) and (274) can be expressed with the help of Eq. (275) as [49]

$$\Gamma_1 = \frac{m^2(1 - z_-)}{z_+z_-}, \quad (276)$$

$$\Gamma_2 = \frac{m^2(1 - z_+)}{z_+z_-}. \quad (277)$$

Differentiating these equations gives [49]

$$\frac{\partial \Gamma_1}{\partial z_-} = -\frac{m^2}{z_+ z_-^2}, \quad (278)$$

$$\frac{\partial \Gamma_2}{\partial z_+} = -\frac{m^2}{z_+^2 z_-}, \quad (279)$$

which will be used later in the next section.

Let $H(\Gamma_1)$ be a probability distribution such that $H(\Gamma_1) d\Gamma_1 dy_1$ is the probability of a quark-antiquark pair being produced at the spacetime position V_1 . From now on, the symbol V_n also represents the breakup event that leads to the creation of the n -th quark-antiquark pair along a surface of constant τ . Let $f(z_+)dz_+$ be the transition probability of obtaining V_2 given that V_1 occurs. The transition probability of V_2 via V_1 is then $H(\Gamma_1) d\Gamma_1 dy_1 f(z_+)dz_+$. Similarly the probability of V_1 via V_2 is $H(\Gamma_2) d\Gamma_2 dy_2 f(z_-)dz_-$. It is reasonable to assume that the probability of V_1 via V_2 is equal to that of V_2 via V_1 such that [49]

$$H(\Gamma_1) d\Gamma_1 dy_1 f(z_+)dz_+ = H(\Gamma_2) d\Gamma_2 dy_2 f(z_-)dz_-. \quad (280)$$

The Jacobian J in

$$d\Gamma_1 dz_+ = J d\Gamma_2 dz_-, \quad (281)$$

is

$$J = \left\| \begin{array}{cc} \frac{\partial \Gamma_1}{\partial \Gamma_2} & \frac{\partial \Gamma_1}{\partial z_-} \\ \frac{\partial z_+}{\partial \Gamma_2} & \frac{\partial z_+}{\partial z_-} \end{array} \right\| = \frac{z_+}{z_-}, \quad (282)$$

which can be easily computed by using Eqs. (278), (279) and $\partial \Gamma_1 / \partial \Gamma_2 = \partial z_+ / \partial z_- = 0$. Eq. (281) can now be re-expressed as [49]

$$d\Gamma_1 \frac{dz_+}{z_+} = d\Gamma_2 \frac{dz_-}{z_-}. \quad (283)$$

Since rapidity is additive (*i. e.* $y_2 = y_1 + \Delta y$),

$$dy_1 = dy_2. \quad (284)$$

With Eqs. (283) and (284), Eq. (280) is simplified as [49]

$$H(\Gamma_1)_{z_+} f(z_+) = H(\Gamma_2)_{z_-} f(z_-). \quad (285)$$

New definitions are now made to facilitate the solution of the equation [49],

$$h(\Gamma) = \log H(\Gamma), \quad (286)$$

$$g(z) = \log(zf(z)). \quad (287)$$

The new definitions transform Eq. (285) as [49]

$$h(\Gamma_1) + g(z_+) = h(\Gamma_2) + g(z_-). \quad (288)$$

Notice that [49]

$$\frac{\partial^2 g(z_+)}{\partial z_+ \partial z_-} = \frac{\partial^2 g(z_-)}{\partial z_+ \partial z_-} = 0. \quad (289)$$

Differentiate Eq. (288) with respect to z_+ and z_- , eliminate terms with $\partial^2 g / \partial z_+ \partial z_-$ using Eq. (289) and cancel out factors of $\partial \Gamma / \partial z$ on the both sides of the equation to obtain [49]

$$\frac{\partial h(\Gamma_1)}{\partial \Gamma_1} + \Gamma_1 \frac{\partial^2 h(\Gamma_1)}{\partial \Gamma_1^2} = \frac{\partial h(\Gamma_2)}{\partial \Gamma_2} + \Gamma_2 \frac{\partial^2 h(\Gamma_2)}{\partial \Gamma_2^2}, \quad (290)$$

or equivalently [49]

$$\frac{d}{d\Gamma} \left(\Gamma \frac{dh}{d\Gamma} \right) = -b, \quad (291)$$

where b is a constant. The solution is [49]

$$h(\Gamma) = -b\Gamma + a \ln \Gamma + \ln C, \quad (292)$$

where C is a constant of integration. It yields the distribution [49]

$$H(\Gamma) = e^{h(\Gamma)} = C \Gamma^a e^{-b\Gamma}. \quad (293)$$

Substituting Eqs. (276) and (277) into Eq. (288) gives [49]

$$\begin{aligned} g_{12}(z_+) + \frac{bm^2}{z_+} + a_1 \ln \frac{m^2}{z_+} - a_2 \ln \frac{1-z_+}{z_+} + \ln C_1 \\ = g_{21}(z_-) + \frac{bm^2}{z_-} + a_2 \ln \frac{m^2}{z_-} - a_1 \ln \frac{1-z_-}{z_-} + \ln C_2, \end{aligned} \quad (294)$$

where $g_{12}(z_+)$ is $g(z_+)$ of V_1 transitioning to V_2 and $g_{21}(z_-)$ is $g(z_-)$ of V_2 transitioning to V_1 . If $a = a_1 = a_2$, the transition probability distribution is [49]

$$f(z_j) = N \frac{1}{z_j} (1-z_j)^a e^{-\frac{bm^2}{z_j}}, \quad (295)$$

where N is a constant of integration. Otherwise, the transition probability from V_α to V_β is [49]

$$f_{\alpha\beta}(z_j) = N_{\alpha\beta} \frac{1}{z_j} z_j^{a_\alpha} \left(\frac{1-z_j}{z_j} \right)^{a_\beta} e^{-\frac{bm^2}{z_j}}, \quad (296)$$

where $N_{\alpha\beta}$ is a constant of integration specific to the vertices V_α and V_β . Let z_{0j} be the j -th rank momentum fraction scaled with respect to p_{+0} , then [49]

$$z_{01} = z_1, \quad (297)$$

$$z_{02} = z_2(1-z_1). \quad (298)$$

The probability of two dependent events is the product of the probabilities of the two individual events. The existence of the rank-2 hadron depends on that of the rank-1 hadron according to the Lund Model so that joint probability of their mutual existence is the product of the two individual probabilities of V_1 and V_2 . With Eqs. (296-298), the combined distribution of the 1st and 2nd rank hadrons is [49]

$$\begin{aligned} f(z_1)dz_1 f(z_2)dz_2 &= f(z_{01})dz_{01} f\left(\frac{z_{02}}{1-z_{01}}\right) \frac{dz_{02}}{1-z_{01}} \\ &= \frac{N dz_{01}}{z_{01}} \frac{N dz_{02}}{z_{02}} (1-z_{01})^a \left(1 - \frac{z_{02}}{1-z_{01}}\right)^a e^{-\frac{bm^2}{z_1} - \frac{bm^2}{z_2}} \\ &= \frac{N dz_{01}}{z_{01}} \frac{N dz_{02}}{z_{02}} (1-z_{01}-z_{02})^a e^{-b(A_1+A_2)}. \end{aligned} \quad (299)$$

The geometrical identity $A_j = bm^2/z_j$ is used in the last step. Generalizing the product of two vertices to that of n vertices, the differential probability for the production of n particles is easily seen as [49]

$$dP(1, \dots, n) = (1-z)^a \prod_{j=1}^n \frac{N dz_{0j}}{z_{0j}} e^{-bA_j}, \quad (300)$$

where $z = \sum_{j=1}^n z_{0j}$. Let $p_{0j} = z_{0j} p_{+0}$ and $d^2p = dp_+ dp_-$. Use the identity [49]

$$\int dC dB \delta(BC - D) = \frac{dB}{B} \quad (301)$$

to obtain [49]

$$\frac{dz_{01}}{z_{01}} \frac{dz_{02}}{z_{02}} = d^2p_{01} d^2p_{02} \delta^+(p_{01}^2 - m^2) \delta^+(p_{01}^2 - m^2). \quad (302)$$

With Eq. (302), Eq. (300) can be rewritten as [49]

$$dP(p_{01}, \dots, p_{0n}) = (1-z)^a \prod_{j=1}^n N d^2 p_{0j} \delta^+(p_{0j}^2 - m^2) e^{-bA_j}. \quad (303)$$

It can be shown from simple geometry in Figure 31 that the kinetic energies of the quarks along the \pm light-cones are [49]

$$W_+ = z p_{0+}, \quad (304)$$

$$W_- = \sum_{j=1}^n \frac{m_j^2}{z_{0j} p_{0+}}, \quad (305)$$

and the total kinetic energy square at V_n is [49]

$$s = W_+ W_- = \sum_{j=1}^n \frac{m_j^2 z}{z_{0j}}. \quad (306)$$

The total differential probability of n -particle production is [49]

$$\begin{aligned} & dP(z, s; p_{01}, \dots, p_{0n}) \\ &= dz \delta \left(z - \sum_{j=1}^n z_{0j} \right) ds \delta \left(s - \sum_{j=1}^n \frac{m_j^2 z}{z_{0j}} \right) dP(p_{01}, \dots, p_{0n}) \\ &= \frac{dz}{z} \delta \left(1 - \sum_{j=1}^n u_j \right) ds \delta \left(s - \sum_{j=1}^n \frac{m_j^2}{u_j} \right) dP(p_{01}, \dots, p_{0n}), \end{aligned} \quad (307)$$

where $u_j \equiv p_{0+j}/W_{n+}$. Use the trick [49]

$$\begin{aligned} & \delta \left(1 - \sum_{j=1}^n \frac{z_{0j}}{z} \right) \delta \left(s - \sum_{j=1}^n \frac{m_j^2}{u_j} \right) \\ &= \delta \left(W_{n+} - W_{n+} \sum_{j=1}^n u_j \right) \delta \left(W_{n-} - \sum_{j=1}^n \frac{m_j^2}{u_j W_{n+}} \right) \\ &= \delta \left(W_{n+} - \sum_{j=1}^n p_{0j+} \right) \delta \left(W_{n-} - \sum_{j=1}^n p_{0j-} \right) \\ &\equiv \delta^2 \left(p_{rest} - \sum_{j=1}^n p_{0j} \right), \end{aligned} \quad (308)$$

where $p_{rest} = (W_{n+}, W_{n-})$, to re-organize Eq. (307) as [49]

$$dP(z, s; p_{01}, \dots, p_{0n}) = ds \frac{dz}{z} (1-z)^a e^{-b\Gamma} \delta \left(p_{rest} - \sum_{j=1}^n p_{0j} \right) \times \prod_{j=1}^n N d^2 p_{0j} \delta^+(p_{0j}^2 - m^2) e^{-bA_{rest}}, \quad (309)$$

with the definition [49]

$$A_{total} \equiv \sum_{j=1}^n A_j = \Gamma + A_{rest}. \quad (310)$$

The claim is that A_{total} is Lorentz invariant. It is called the ‘‘Area Law’’ [51]. Eq. (309) can be separated in the external and internal parts as in [49]

$$dP_{ext} = ds \frac{dz}{z} (1-z)^a e^{-b\Gamma}, \quad (311)$$

$$dP_{int} = \prod_{j=1}^n N d^2 p_{0j} \delta^+(p_{0j}^2 - m^2) \delta \left(p_{rest} - \sum_{j=1}^n p_{0j} \right) e^{-bA_{rest}}. \quad (312)$$

The external part contains kinematic variables s , z and Γ . The internal part contains dynamic variables p_{0j} . Eqs. (311) and (312) are the final results.

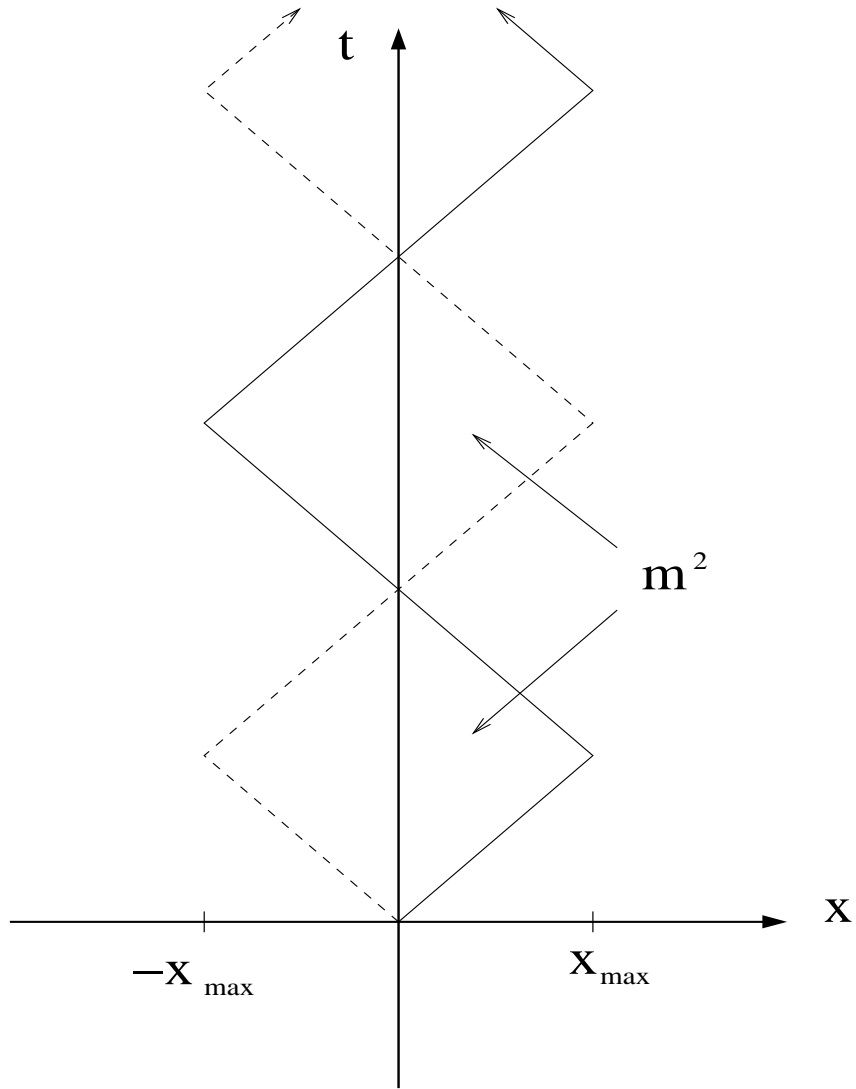


Figure 28: The yoyo motion of a quark-antiquark pair confined by a linear potential. The two quarks are assumed to be massless. The mass square of the meson is proportional to the area of each square. The meson shown here is at rest.

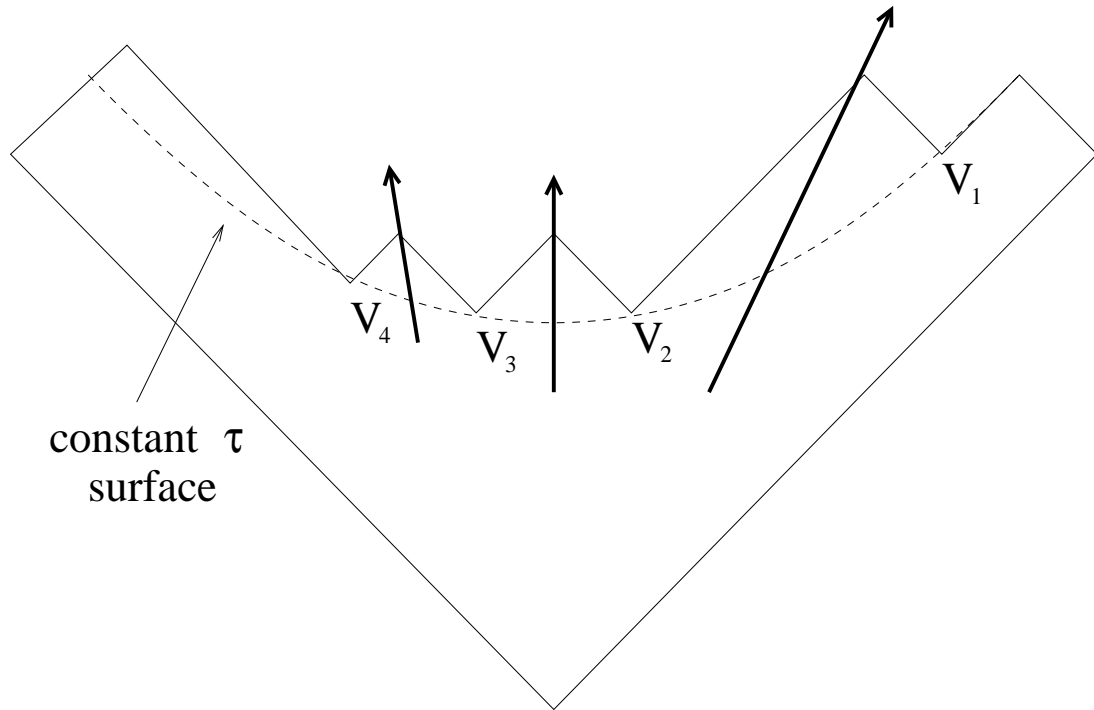


Figure 29: The breakup of a quark-antiquark pair along a surface of constant proper time τ . The bold arrows represents the velocities of the produced mesons. The breakup points are labelled as vertices V_1 to V_n .

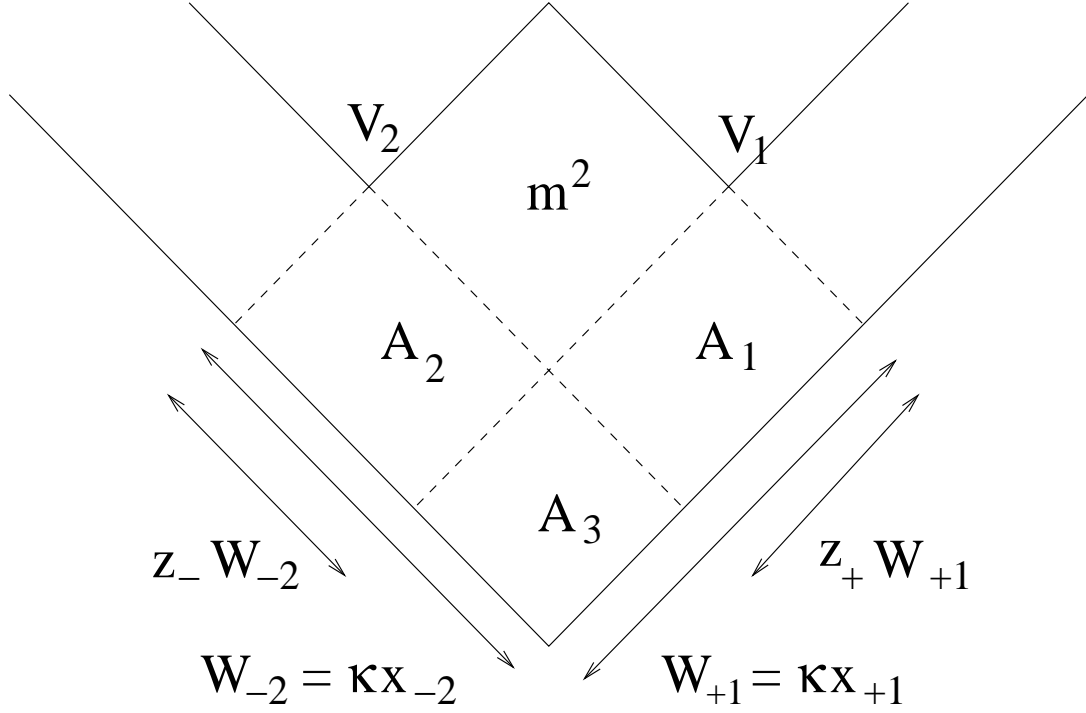


Figure 30: The geometry of the kinematics of two adjacent vertices V_1 and V_2 . V_1 and V_2 are vertices or spacetime positions which also represent the energy carried by the string field. The quark moves along the positive light-cone and the antiquark moves along the negative light-cone. The antiquark of V_1 combines with the quark of V_2 to produce a meson of mass m . W_{+1} is the energy of V_1 along x_+ . $z_+ W_{+1}$ is the fraction of energy used to create a quark from V_2 . W_{-2} is the energy of V_2 along x_- . $z_- W_{-2}$ is the fraction of energy used to create an antiquark from V_1 . A_1 , A_2 , A_3 and m^2 are the areas of the rectangles. The figure is taken from reference [49].

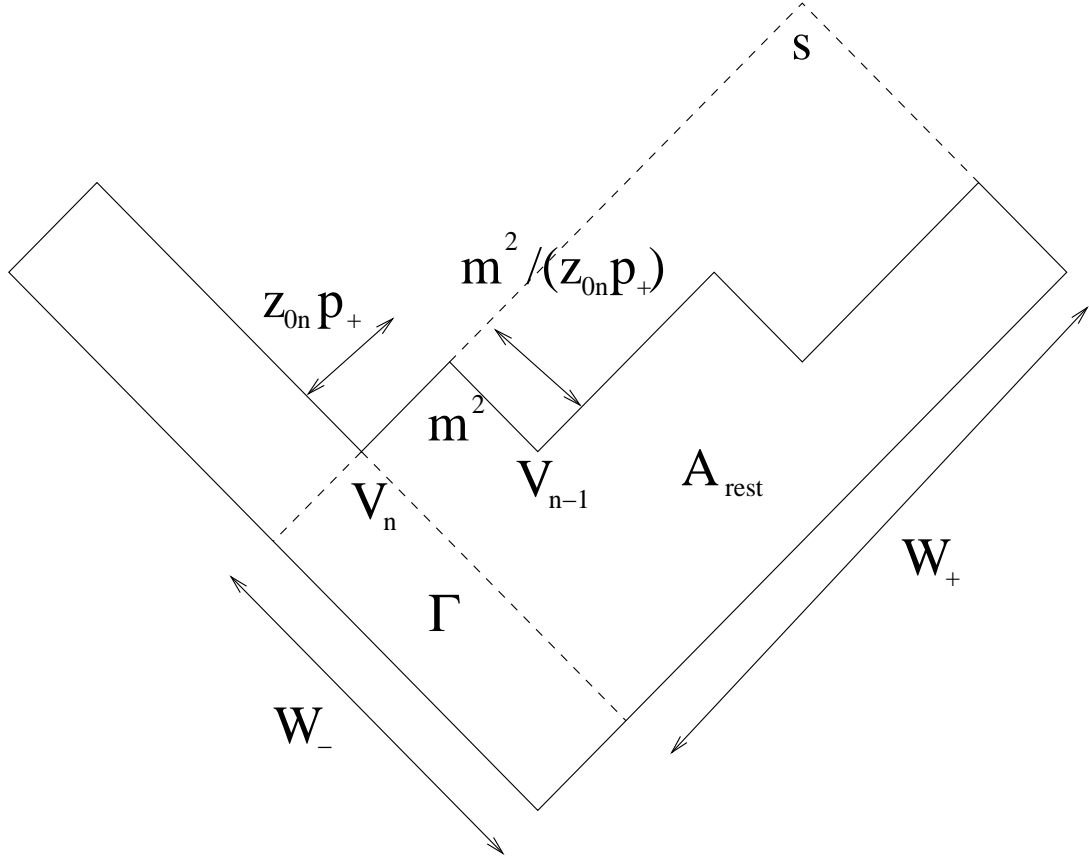


Figure 31: The geometry of the kinematics of involving the total area of the spacetime diagram such that $A_{total} = \Gamma + A_{rest}$. The total energy square $s = W_+W_-$ is represented by the rectangle labelled s . p_{\pm} is the energy of the parent quark (antiquark) along the \pm light-cone coordinates. $z_{0n}p_+$ is the fraction of energy used to create a quark from V_n . $m^2/(z_{0n}p_+)$ is the energy used to create an antiquark from V_{n-1} . The figure is taken from reference [49] with minor modifications.

Appendix C

The Parton Model

The relevant formulas of the parton model in reference [66] are derived below. Several mistakes found in reference [66] have been corrected in this appendix.

C.1 External Cross Section Formulas

The Feynman diagram of hadrons A and B scattering into partons c and d , $A + B \rightarrow c + d$, is illustrated in Figure 32. The external Mandelstam variables are defined as

$$s \equiv (P_A + P_B)^2 = 2P_A \cdot P_B, \quad (313)$$

$$t \equiv (p_c - P_A)^2 = -2p_c \cdot P_A = -\frac{s}{2} x_T \mathcal{T}_c, \quad (314)$$

$$u \equiv (p_c - P_B)^2 = -2p_c \cdot P_B = -\frac{s}{2} x_T \frac{1}{\mathcal{T}_c}, \quad (315)$$

where

$$x_T \equiv \frac{2p_T}{\sqrt{s}}, \quad (316)$$

and

$$\mathcal{T}_c \equiv \tan \frac{\theta_c}{2}. \quad (317)$$

Eq. (314) is proved as follow: In the high energy limit, $m_i = 0$, $\forall i$, such that $E_i = |\mathbf{p}_i|$.

$$E_A = E_B = |\mathbf{P}_A| = |\mathbf{P}_B| = \frac{\sqrt{s}}{2}. \quad (318)$$

From Figure 32, it is obvious that

$$p_T = |\mathbf{p}_c| \sin \theta_c. \quad (319)$$

$$t = -2 p_c \cdot P_A \quad (320)$$

$$= -2 (E_c E_A - |\mathbf{p}_c| |\mathbf{P}_A| \cos \theta_c) \quad (321)$$

$$= -2 (|\mathbf{p}_c| |\mathbf{P}_A| - |\mathbf{p}_c| |\mathbf{P}_A| \cos \theta_c) \quad (322)$$

$$= -2 p_T |\mathbf{P}_A| \frac{1 - \cos \theta_c}{\sin \theta_c} \quad (323)$$

$$= -2 \left(\frac{x_T \sqrt{s}}{2} \right) \left(\frac{\sqrt{s}}{2} \right) \frac{1 - (1 - 2 \sin^2(\theta_c/2))}{2 \sin(\theta_c/2) \cos(\theta_c/2)} \quad (324)$$

$$= -\frac{s}{2} x_T \mathcal{T}_c. \quad (325)$$

Similarly,

$$u = -2 p_c \cdot P_B \quad (326)$$

$$= -2 (E_c E_B - |\mathbf{p}_c| |\mathbf{P}_B| \cos(180^\circ - \theta_c)) \quad (327)$$

$$= -2 (E_c E_B + |\mathbf{p}_c| |\mathbf{P}_B| \cos \theta_c) \quad (328)$$

$$= -\frac{s}{2} x_T \frac{1}{\mathcal{T}_c}. \quad (329)$$

In the massless limit, the sum rule of external Mandelstam variables is

$$s + t + u = 0. \quad (330)$$

A fraction, x_i , of the momentum of the incoming hadron P_i makes up the momentum of parton p_i . More specifically, we have

$$p_a = x_a P_A, \quad (331)$$

$$p_b = x_b P_B. \quad (332)$$

These imply that

$$|\mathbf{p}_a| = \frac{x_a \sqrt{s}}{2}, \quad (333)$$

$$|\mathbf{p}_b| = \frac{x_b \sqrt{s}}{2}. \quad (334)$$

The internal Mandelstam variables, \hat{s} , \hat{t} and \hat{u} , of the partons can now be written in terms of the external Mandelstam variables, s , t and u .

$$\hat{s} = (p_a + p_b)^2 = 2p_a \cdot p_b = x_a x_b s, \quad (335)$$

$$\hat{t} = (p_c - p_a)^2 = -2p_c \cdot p_a = x_a t, \quad (336)$$

$$\hat{u} = (p_c - p_b)^2 = -2p_c \cdot p_b = x_b u. \quad (337)$$

The conservation of energy-momentum is given as

$$p_a + p_b = p_c + p_d. \quad (338)$$

From the expressions of the internal and external Mandelstam variables, it is easily seen that

$$p_T^2 = \frac{tu}{s} = \frac{\hat{t}\hat{u}}{\hat{s}}. \quad (339)$$

In the massless limit, the sum rule of the internal Mandelstam variables is

$$\hat{s} + \hat{t} + \hat{u} = 0, \quad (340)$$

or equivalently,

$$x_a x_b s + x_a t + x_b u = 0 \quad (341)$$

From Eq. (341), we have

$$x_a = \frac{-x_b u}{x_b s + t} = \frac{-x_b u/s}{x_b + t/s} = \frac{x_b x_1}{x_b - x_2}, \quad (342)$$

where

$$x_1 \equiv -\frac{u}{s} = \frac{1}{2} x_T \frac{1}{\mathcal{T}_c}, \quad (343)$$

$$x_2 \equiv -\frac{t}{s} = \frac{1}{2} x_T \mathcal{T}_c. \quad (344)$$

Similarly,

$$x_b = \frac{-x_a t}{x_a s + u} = \frac{-x_a t/s}{x_a + u/s} = \frac{x_a x_2}{x_a - x_1}, \quad (345)$$

The expression $\hat{t} = (p_c - p_a)^2 = (p_d - p_b)^2$ can be considered separately as

$$\hat{t} = (p_c - p_a)^2 = -2p_c \cdot p_a = -\frac{s}{2} x_T x_a \mathcal{T}_c, \quad (346)$$

$$\hat{t} = (p_d - p_b)^2 = -2p_d \cdot p_b = -\frac{s}{2} x_T x_b \frac{1}{\mathcal{T}_d}, \quad (347)$$

where

$$\mathcal{T}_d \equiv \tan \frac{\theta_d}{2}. \quad (348)$$

Eqs. (346) and (347) imply that

$$x_a \mathcal{T}_c = x_b \frac{1}{\mathcal{T}_d}. \quad (349)$$

The internal Mandelstam variables can be re-expressed in terms of the external angles as follow.

$$|\mathbf{p}_a - \mathbf{p}_b| = |\mathbf{p}_c| \cos \theta_c + |\mathbf{p}_d| \cos \theta_d \quad (350)$$

$$= \frac{p_T}{\sin \theta_c} \cos \theta_c + \frac{p_T}{\sin \theta_d} \cos \theta_d, \quad (351)$$

which implies

$$|x_a \mathbf{P}_A - x_b \mathbf{P}_B| = \left| x_a \frac{\sqrt{s}}{2} - x_b \frac{\sqrt{s}}{2} \right| \quad (352)$$

$$= p_T (\cot \theta_c + \cot \theta_d), \quad (353)$$

or equivalently

$$x_a - x_b = x_T (\cot \theta_c + \cot \theta_d) \quad (354)$$

$$= x_T \left(\frac{1 - \tan^2(\theta_c/2)}{2 \tan(\theta_c/2)} + \frac{1 - \tan^2(\theta_d/2)}{2 \tan(\theta_d/2)} \right) \quad (355)$$

$$= x_T \left(\frac{1 - \mathcal{T}_c^2}{2\mathcal{T}_c} + \frac{1 - \mathcal{T}_d^2}{2\mathcal{T}_d} \right) \quad (356)$$

$$= \frac{1}{2} x_T \left[\left(\frac{1}{\mathcal{T}_c} - \mathcal{T}_c \right) + \left(\frac{1}{\mathcal{T}_d} - \mathcal{T}_d \right) \right]. \quad (357)$$

Eqs. (349) and (357) together give

$$x_a = \frac{1}{2} x_T \left(\frac{1}{\mathcal{T}_c} + \frac{1}{\mathcal{T}_d} \right), \quad (358)$$

$$x_b = \frac{1}{2} x_T (\mathcal{T}_c + \mathcal{T}_d). \quad (359)$$

Finally, the internal Mandelstam variables can be re-expressed in terms of the external angles as

$$\hat{s} = \frac{s}{4} x_T^2 \left(2 + \frac{\mathcal{T}_c}{\mathcal{T}_d} + \frac{\mathcal{T}_d}{\mathcal{T}_c} \right), \quad (360)$$

$$\hat{t} = \frac{s}{4} x_T^2 \left(1 + \frac{\mathcal{T}_c}{\mathcal{T}_d} \right), \quad (361)$$

$$\hat{u} = \frac{s}{4} x_T^2 \left(1 + \frac{\mathcal{T}_d}{\mathcal{T}_c} \right). \quad (362)$$

Eqs. (360)–(362) will not be used directly in this work. However it is interesting to know that the internal Mandelstam variables can be measured in terms of the external angles. Another interesting fact worth mentioning is that Eqs. (342) and (345) are still true even if \mathcal{T}_c is replaced by \mathcal{T}_d in Eqs. (343) and (344). This statement can be checked easily by substituting Eq. (349) into Eqs. (342) and (345) and then solve for x_a and x_b . The interchangeability of \mathcal{T}_c and \mathcal{T}_d will become useful later in some of the derivations below.

The differential cross section of parton production for the reaction $A + B \rightarrow c + d$ is

$$d\sigma = f_{A/a}(x_a, Q^2) dx_a f_{B/b}(x_b, Q^2) dx_b \frac{d\hat{\sigma}}{d\hat{t}} d\hat{t}, \quad (363)$$

where $f_{A/a}(x_a, Q^2)$ and $f_{B/b}(x_b, Q^2)$ are the renormalized parton distribution functions (PDF's) of parton a in hadron A and of parton b in hadron B respectively. Although Q^2 has a simple interpretation in QED,

$$Q^2 = (p' - p)^2 = \frac{1}{2} E' E \sin \frac{\theta}{2} \quad (364)$$

(where p and p' are the incoming and outgoing lepton momenta and θ is the scattering angle), there is no clear understanding of what is Q^2 in hadron collisions. Some good guesses are

$$Q^2 = 4\hat{p}_T^2, \quad (365)$$

$$Q^2 = \frac{2\hat{s}\hat{t}\hat{u}}{\hat{s}^2 + \hat{t}^2 + \hat{u}^2}. \quad (366)$$

Although the interest of this work is not parton production *per se*, it serves as an intuitive starting point to introduce hadron production later.

The substitution of Eqs. (343) and (344) into Eq. (342) gives

$$x_a x_b - \frac{1}{2} x_a x_T \mathcal{T}_c = \frac{1}{2} x_b x_T \frac{1}{\mathcal{T}_c}. \quad (367)$$

Differentiating x_b in Eq. (367) with respect to \mathcal{T}_c and x_T while keeping x_a fixed gives

$$\frac{\partial x_b}{\partial \mathcal{T}_c} = \frac{x_a x_T \mathcal{T}_c - x_b x_T \mathcal{T}_c^{-1}}{2x_a \mathcal{T}_c - x_T}, \quad (368)$$

$$\frac{\partial x_b}{\partial x_T} = \frac{x_b + x_a \mathcal{T}_c^2}{2x_a \mathcal{T}_c - x_T}. \quad (369)$$

Repeat the same process with $\hat{t} = -\frac{s}{2} x_T x_a \mathcal{T}_c$ yields

$$\frac{\partial \hat{t}}{\partial \mathcal{T}_c} = -\frac{s}{2} x_T x_a, \quad (370)$$

$$\frac{\partial \hat{t}}{\partial x_T} = -\frac{s}{2} x_a \mathcal{T}_c. \quad (371)$$

The Jacobian now can be computed with Eqs. (368)–(371) as

$$\frac{\partial(x_b, \hat{t})}{\partial(\mathcal{T}_c, x_T)} = \frac{x_a x_b x_T s}{2x_a \mathcal{T}_c - x_T} = \frac{x_a x_b x_T s}{2(x_a - x_1) \mathcal{T}_c}. \quad (372)$$

or

$$\frac{\partial(x_b, \hat{t})}{\partial(\theta_c, x_T)} = \frac{\partial(x_b, \hat{t})}{\partial(\mathcal{T}_c, x_T)} \frac{d\mathcal{T}_c}{d\theta_c} \quad (373)$$

$$= \frac{x_a x_b x_T s}{2(x_a - x_1) \mathcal{T}_c} \left(\frac{1 - \mathcal{T}_c^2}{2} \right) \quad (374)$$

$$= \frac{s}{2} \frac{x_a x_b}{x_a - x_1} \frac{x_T}{\sin \theta_c} \quad (375)$$

Given that $E = m_T \cosh y$ and $p_z = m_T \sinh y$, $dp_z/dy = E$. In the cylindrical coordiantes,

$$dp^3 = \pi dp_z dp_T^2 \quad (376)$$

$$= \pi E dy dp_T^2. \quad (377)$$

With $p_T^2 = \frac{s}{2} x_T dx_T$,

$$dp_T^2 = \frac{s}{2} x_T dx_T. \quad (378)$$

And with

$$y = \frac{1}{2} \ln \frac{1 + \cos \theta_c}{1 - \cos \theta_c}, \quad (379)$$

there is also

$$dy = \frac{d\theta_c}{\sin \theta_c}. \quad (380)$$

Substitute Eqs. (378) and (380) into Eq. (377) to get

$$\frac{dp^3}{E} = \pi dy dp_T^2 \quad (381)$$

$$= \frac{\pi}{2} \frac{x_T s}{\sin \theta_c} d\theta_c dx_T. \quad (382)$$

Combine the Jacobian in Eq. (375) with Eq. (382) and obtain

$$dx_b d\hat{t} = \frac{1}{\pi} \frac{x_a x_b}{x_a - x_1} \frac{dp^3}{E}. \quad (383)$$

With Eq. (383), the Lorentz invariant differential parton production cross section from Eq. (363) can be written as

$$E \frac{d^3\sigma}{dp^3} = \frac{1}{\pi} f_{A/a}(x_a, Q^2) dx_a f_{B/b}(x_b, Q^2) \frac{x_a x_b}{x_a - x_1} \frac{d\hat{\sigma}}{d\hat{t}}. \quad (384)$$

The inclusive cross section for $A + B \rightarrow c + X$ can be obtained from Eq. (384) by integrating over θ_d , or equivalently by integrating over x_a as in $dx_a = (x_a - x_1) dy_d$. The relationship between dy_d and dx_a can be derived as follow. Substitute Eqs. (349), (343) and (344) into Eq. (345) and obtain

$$x_a \mathcal{T}_c \mathcal{T}_d = \frac{x_a (\frac{1}{2} x_T \mathcal{T}_d)}{x_a - \frac{1}{2} x_T \mathcal{T}_d}. \quad (385)$$

x_a can be isolated from Eq. (385) as

$$x_a - \frac{1}{2} x_T \frac{1}{\mathcal{T}_d} = x_1. \quad (386)$$

Differentiating Eq. (386) with x_T and x_1 held fixed yields

$$dx_a = \frac{1}{2} x_T \frac{1}{\mathcal{T}_d^2} d\mathcal{T}_d \quad (387)$$

$$= \frac{1}{2} x_T \frac{1}{\mathcal{T}_d} dy_d \quad (388)$$

$$= \frac{1}{2} x_T \frac{x_a \mathcal{T}_c}{x_b} dy_d \quad (389)$$

$$= \frac{x_a x_2}{x_b} dy_d \quad (390)$$

$$= (x_a - x_1) dy_d. \quad (391)$$

The inclusive cross section for $A + B \rightarrow c + X$ is

$$E \frac{d^3\sigma}{dp^3} = \frac{1}{\pi} \int_{x_a^{min}}^1 dx_a f_{A/a}(x_a, Q^2) f_{B/b}(x_b, Q^2) \frac{x_a x_b}{x_a - x_1} \frac{d\hat{\sigma}}{dt}, \quad (392)$$

where

$$x_a^{min} = \frac{x_1}{1 - x_2} = \frac{x_T/\mathcal{T}_c}{2 - x_T\mathcal{T}_c}. \quad (393)$$

The lower limit of the integral in Eq. (392) is not zero is that x_a , as seen in Eq. (342). $x_a < 0$ for $x_b < x_2$, which is not allowed. At $x_b = x_2$, $x_a \rightarrow \infty$, which is also impossible. Hence the value of x_a is limited by a range of x_b . It can be seen in Figure 33 that x_a is at its minimum when $x_b = 1$ and the maximum value of x_a is 1.

Once the formalism of parton production is complete, the derivation of the inclusive hadron production cross section can be essentially the same. The external Mandelstam variables are similarly defined,

$$s \equiv (P_A + P_B)^2 = 2P_A \cdot P_B, \quad (394)$$

$$t \equiv (P_h - P_A)^2 = -2p_h \cdot P_A = -\frac{s}{2} x_T \mathcal{T}_h, \quad (395)$$

$$u \equiv (P_h - P_B)^2 = -2p_h \cdot P_B = -\frac{s}{2} x_T \frac{1}{\mathcal{T}_h}. \quad (396)$$

The internal Mandelstam variables are slightly modified as

$$\hat{s} \equiv (p_a + p_b)^2 = x_a x_b s, \quad (397)$$

$$\hat{t} \equiv (p_c - p_a)^2 = -2p_c \cdot p_a = -2 \frac{P_h}{z_c} \cdot p_a = \frac{x_a t}{z_c}, \quad (398)$$

$$\hat{u} \equiv (p_c - p_b)^2 = -2p_c \cdot p_b = -2 \frac{P_h}{z_c} \cdot p_b = \frac{x_b u}{z_c}, \quad (399)$$

where

$$p_a = x_a P_A, \quad (400)$$

$$p_b = x_b P_B, \quad (401)$$

$$P_h = z_c p_c. \quad (402)$$

Eq. (340) combined with Eqs. (397)–(402) gives

$$z_c = \frac{x_2}{x_b} + \frac{x_1}{x_a}, \quad (403)$$

with

$$x_1 = -\frac{u}{s} = \frac{1}{2} x_T \frac{1}{\mathcal{T}_h}, \quad (404)$$

$$x_2 = -\frac{t}{s} = \frac{1}{2} x_T \mathcal{T}_h, \quad (405)$$

$$\mathcal{T}_h = \tan \frac{\theta_{cm}}{2}. \quad (406)$$

Differentiate Eq. (403) to obtain

$$\frac{\partial z_c}{\partial \theta_{cm}} = \frac{1}{4} \left(-\frac{1}{x_a \mathcal{T}_h^2} + \frac{\mathcal{T}_h}{x_b} \right) \sec^2 \frac{\theta_{cm}}{2}, \quad (407)$$

$$\frac{\partial z_c}{\partial x_T} = \frac{1}{2} \left(\frac{1}{x_a \mathcal{T}_h} + \frac{\mathcal{T}_h}{x_b} \right), \quad (408)$$

$$\frac{\partial \hat{t}}{\partial \theta} = -\frac{1}{4} \frac{x_T x_a}{z_c} \sec^2 \frac{\theta_{cm}}{2}, \quad (409)$$

$$\frac{\partial \hat{t}}{\partial x_T} = -\frac{1}{2} \frac{x_a}{z_c} \mathcal{T}_h. \quad (410)$$

The Jacobian can be computed from Eqs. (407)–(410),

$$\frac{\partial(z_c, \hat{t})}{\partial(\theta_{cm}, x_T)} = \frac{x_T s}{2z_c \sin \theta_{cm}}. \quad (411)$$

As before,

$$d\theta_{cm} dx_T = \frac{2}{\pi s} \frac{\sin \theta_{cm}}{x_T} \frac{dp^3}{E}, \quad (412)$$

such that

$$dz_c d\hat{t} = \frac{1}{\pi z_c} \frac{dp^3}{E}. \quad (413)$$

The differential hadron production cross section is

$$d\sigma = f_{A/a}(x_a, Q^2) dx_a f_{B/b}(x_b, Q^2) dx_b \frac{d\hat{\sigma}}{d\hat{t}} d\hat{t} D_c^h(z_c, Q^2) dz_c. \quad (414)$$

The major difference between the parton and hadron cross section formulas is the inclusion of the fragmentation function (FF), $D_c^h(z_c, Q^2)$. The inclusive hadron production cross section is

$$E \frac{d^3\sigma}{dp^3} = \frac{1}{\pi} \int_{x_a^{min}}^1 dx_a \int_{x_b^{min}}^1 dx_b f_{A/a}(x_a, Q^2) f_{B/b}(x_b, Q^2) D_c^h(z_c, Q^2) \frac{1}{z_c} \frac{d\hat{\sigma}}{d\hat{t}}, \quad (415)$$

with

$$x_a^{min} = \frac{x_1}{1 - x_2}, \quad (416)$$

$$x_b^{min} = \frac{x_a x_2}{x_a - x_1}. \quad (417)$$

C.2 Internal Cross Section Formulas

The internal cross sections,

$$\frac{d\hat{\sigma}}{d\hat{t}}(ab \rightarrow cd; \hat{s}, \hat{t}) = \frac{\pi\alpha_s^2(Q^2)}{\hat{s}^2} |\overline{\mathcal{M}}(ab \rightarrow cd)|^2, \quad (418)$$

are derived by adding the leading order Feynman diagrams [67] together, with

$$|\overline{\mathcal{M}}(q_i q_j \rightarrow q_i q_j)|^2 = |\overline{\mathcal{M}}(q_i \bar{q}_j \rightarrow q_i \bar{q}_j)|^2 = \frac{4}{9} \frac{\hat{s}^2 + \hat{u}^2}{\hat{t}^2}, \quad (419)$$

$$|\overline{\mathcal{M}}(q_i q_i \rightarrow q_i q_i)|^2 = \frac{4}{9} \left(\frac{\hat{s}^2 + \hat{u}^2}{\hat{t}^2} + \frac{\hat{s}^2 + \hat{t}^2}{\hat{u}^2} \right) - \frac{8}{27} \frac{\hat{s}^2}{\hat{u}\hat{t}}, \quad (420)$$

$$|\overline{\mathcal{M}}(q_i \bar{q}_i \rightarrow q_i \bar{q}_i)|^2 = \frac{4}{9} \left(\frac{\hat{s}^2 + \hat{u}^2}{\hat{t}^2} + \frac{\hat{t}^2 + \hat{u}^2}{\hat{s}^2} \right) - \frac{8}{27} \frac{\hat{u}^2}{\hat{s}\hat{t}}, \quad (421)$$

$$|\overline{\mathcal{M}}(q_i \bar{q}_i \rightarrow gg)|^2 = \frac{32}{27} \left(\frac{\hat{u}^2 + \hat{t}^2}{\hat{u}\hat{t}} \right) - \frac{8}{3} \left(\frac{\hat{u}^2 + \hat{t}^2}{\hat{s}^2} \right), \quad (422)$$

$$|\overline{\mathcal{M}}(gg \rightarrow q_i \bar{q}_i)|^2 = \frac{1}{6} \left(\frac{\hat{u}^2 + \hat{t}^2}{\hat{u}\hat{t}} \right) - \frac{3}{8} \left(\frac{\hat{u}^2 + \hat{t}^2}{\hat{s}^2} \right), \quad (423)$$

$$|\overline{\mathcal{M}}(q_i g \rightarrow q_i g)|^2 = -\frac{4}{9} \left(\frac{\hat{u}^2 + \hat{s}^2}{\hat{u}\hat{s}} \right) + \left(\frac{\hat{u}^2 + \hat{s}^2}{\hat{t}^2} \right), \quad (424)$$

$$|\overline{\mathcal{M}}(gg \rightarrow gg)|^2 = \frac{9}{2} \left(3 - \frac{\hat{u}\hat{t}}{\hat{s}^2} - \frac{\hat{u}\hat{s}}{\hat{t}^2} - \frac{\hat{s}\hat{t}}{\hat{u}^2} \right), \quad (425)$$

and

$$\alpha_{LO}(Q^2) = \frac{12\pi}{(33 - 2n_f) \log\left(\frac{Q^2}{\Lambda^2}\right)}, \quad (426)$$

$$\alpha_s(Q^2) = \alpha_{LO}(Q^2) \left[1 - \frac{1}{4\pi} \frac{306 - 38n_f}{33 - 2n_f} \alpha_{LO}(Q^2) \log \log \left(\frac{Q^2}{\Lambda^2} \right) \right], \quad (427)$$

where n_f is the number of flavors and $\Lambda_{\overline{MS}} \approx 0.2 \text{ GeV}^2$ by convention.

C.3 Fragmentation Functions

The fragmentation function, $D_q^h(z, Q^2)$, registers the number of hadrons of type h with energy fraction,

$$z = \frac{2E_h}{Q}, \quad (428)$$

per dz generated by the initial quark q . Energy conservation gives

$$\sum_h \int_0^1 z D_q^h(z, Q^2) dz = 1. \quad (429)$$

It is assumed that scaling occurs, *i. e.*

$$D_q^h(z, Q^2) = D_q^h(z). \quad (430)$$

The multiplicity of h emerging from q is

$$\int_{z_{min}}^1 D_q^h(z) dz, \quad (431)$$

where $z_{min} = 2m_h/Q$. The fragmentation function cannot be calculated exactly by QCD. Feynman and Field have a semi-analytical parameterization [66], which is now being described below. Let $f(\eta) d\eta$ be the probability that the first hierarchy (rank 1) meson leaves fractional momentum η to the remaining cascade. The function $f(\eta)$ is normalized,

$$\int_0^1 f(\eta) d\eta = 1. \quad (432)$$

Secondly let $F(z) dz$ be the probability of finding a meson (independent of rank) with fractional momentum z within dz in a jet. Feynman and Field assumed a simple stochastic ansatz that probability distribution is recursive. This way $F(z)$ satisfies the integral equation

$$F(z) = f(1-z) + \int_z^1 \frac{d\eta}{\eta} f(\eta) F(z/\eta). \quad (433)$$

The first term gives the probability that the produced meson is rank 1. The second term calculates the probability of the production of a higher rank meson recursively. Data of deep inelastic scattering experiments suggest the simple form

$$zF(z) = f(1-z) = (n+1)(1-z)^n. \quad (434)$$

The power $n = 2$ gives a qualitative description of experimental data.

Next the flavor dependent part of the fragmentation function is considered. Let β_i be the probability of the $q_i\bar{q}_i$ pair. The normalization condition imposes that

$$\sum_{i=1}^{n_f} \beta_i = 1. \quad (435)$$

The isospin symmetry implies that

$$\beta_u = \beta_d = \beta. \quad (436)$$

Furthermore, data indicate that $\beta_s \approx \frac{1}{2}\beta_u$ and that β_c and β_b are small. For a quark of flavor q , the mean number of meson states of flavor $a\bar{b}$ at z is, in analogy of Eq. (433), given by

$$P_q^{a\bar{b}}(z) = \delta_{aq}\beta_b f(1-z) + \int_z^1 \frac{d\eta}{\eta} f(\eta) \beta_q P_q^{a\bar{b}}(z/\eta). \quad (437)$$

The mean number of meson states averaged over all quarks is

$$P_{\langle q \rangle}^{a\bar{b}}(z) = \sum_c \beta_c P_c^{a\bar{b}}(z), \quad (438)$$

so that

$$P_{\langle q \rangle}^{a\bar{b}}(z) = \beta_a \beta_b f(1-z) + \int_z^1 \frac{d\eta}{\eta} f(\eta) P_{\langle q \rangle}^{a\bar{b}}(z/\eta). \quad (439)$$

Comparing with Eq. (433) yields

$$P_{\langle q \rangle}^{a\bar{b}}(z) = \beta_a \beta_b F(z). \quad (440)$$

Comparing Eqs. (437), (439) and (440) yields

$$P_q^{a\bar{b}}(z) = \delta_{aq}\beta_b f(1-z) + \beta_a \beta_b \bar{F}(z), \quad (441)$$

where

$$\bar{F}(z) = F(z) - f(1-z). \quad (442)$$

Eqs. (434) and (442) together give

$$z\bar{F}(z) = (n+1)(1-z)^{n+1}. \quad (443)$$

The mean number of meson state, $P_q^{a\bar{b}}(z)$, is related to the fragmentation function as in

$$D_q^h(z) = \sum_{a,b} \Gamma_{a\bar{b}}^h P_q^{a\bar{b}}(z), \quad (444)$$

where $\Gamma_{a\bar{b}}^h$ is the probability of h containing $a\bar{b}$. For example, $\Gamma_{u\bar{d}}^{\pi^+} = 1$ and $\Gamma_{u\bar{u}}^{\pi^0} = \Gamma_{d\bar{d}}^{\pi^0} = \frac{1}{2}$. Substitute Eq. (441) into Eq. (444) to obtain

$$D_q^h(z) = A_q^h f(1-z) + B^h \bar{F}(z), \quad (445)$$

where

$$A_q^h = \sum_b \Gamma_{q\bar{b}}^h \beta_b, \quad (446)$$

$$B^h = \sum_q \beta_q A_q^h. \quad (447)$$

As a example, given that $\beta_u = \beta_d = 2\beta_s = \beta$ and $\beta_c = \beta_b = \beta_t = 0$, it is easily shown that $\beta = 0.4$, and

$$A_u^{\pi^0} = \frac{1}{2} \beta, \quad (448)$$

$$A_d^{\pi^0} = \frac{1}{2} \beta, \quad (449)$$

$$A_s^{\pi^0} = 0, \quad (450)$$

$$B^{\pi^0} = \beta^2. \quad (451)$$

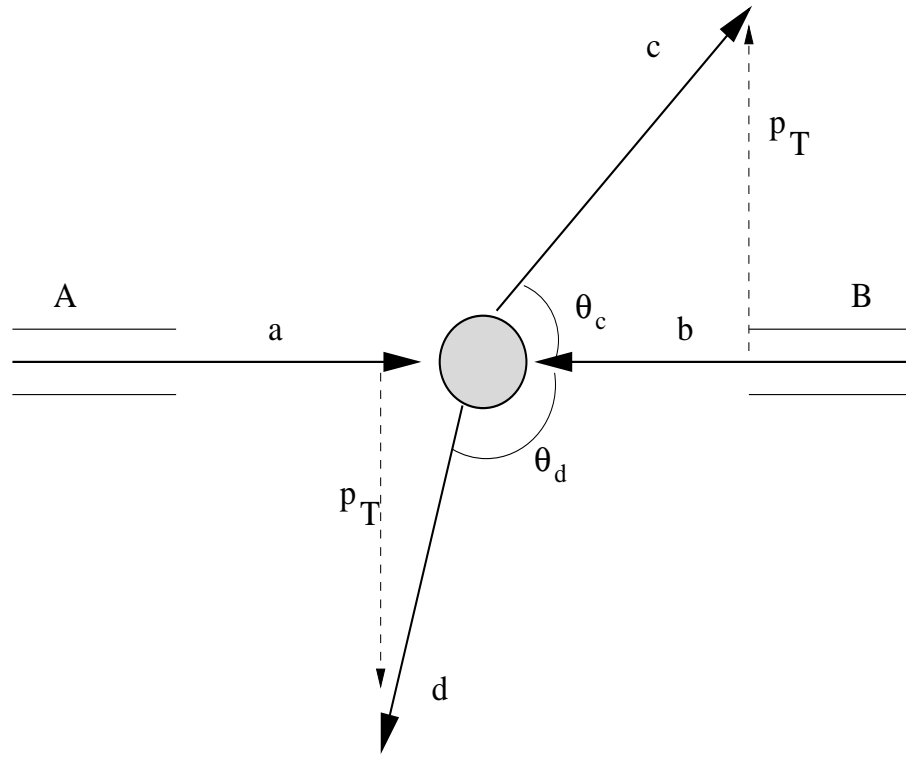


Figure 32: Parton a of hadron A collides with parton b of hadron B producing partons c and d . The transverse momenta, p_T , of c and d are equal and opposite.

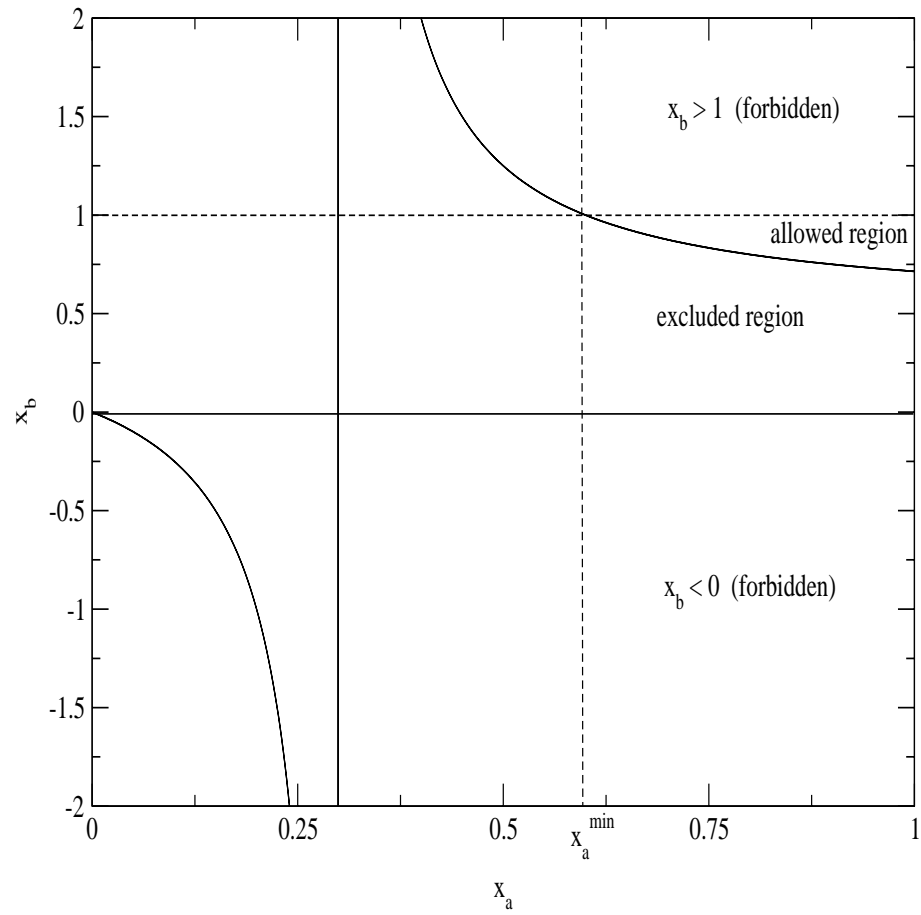


Figure 33: The plot of x_a versus x_b with $x_b = x_a x_2 / (x_a - x_1)$. $x_a^{\min} = x_1 / (1 - x_2)$. The values of $x_1 = 0.5$ and $x_2 = 0.3$ are used.

Bibliography

- [1] E. Di Salvo, L. Kondratyuk and P. Saracco, *hep-ph/9411309*.
- [2] V. V. Andreev and M. N. Sergeenko, *hep-ph/991299*.
- [3] G. F. Chew, *S-Matrix Theory of Strong Interactions*, (W. A. Benjamin, New York, 1961).
- [4] J. J. Sakurai, *Modern Quantum Mechanics*, (Addison-Wesley, Redwood City, California, 1985), 399–410.
- [5] T. Regge, *Nuovo Cim*, **14**, 951 (1959).
- [6] T. Regge, *Nuovo Cim*, **18**, 947 (1960).
- [7] G. F. Chew and S. C. Frautschi, *Phys. Rev. Letters*, **8**, 41 (1962).
- [8] S. C. Frautschi, *Regge Poles and S-Matrix Theory*, (W. A. Benjamin, New York, 1968), 175.
- [9] P. D. B. Collins, *An Introduction to Regge Theory & High Energy Physics*, (Cambridge University Press, Cambridge, 1977).
- [10] R. Ommes and M. Froissart, *Mandelstam Theory and Regge Poles*, (W. A. Benjamin, New York, 1963).
- [11] J. R. Forshaw and D. A. Ross, *Quantum Chromodynamics and the Pomeron*, (Cambridge University Press, Cambridge, 1997), 13–17.
- [12] S. Weinberg, *The Quantum Theory of Fields*, (Cambridge University Press, Cambridge, 1995), 468–469.

- [13] C. B. Chiu, *Annual Review of Nuclear Science*, **22**, 255 (1972).
- [14] E. Segrè, *Nuclei and Particles*, (Benjamin/Cummings, Menlo Park, California, 1982), 832.
- [15] S. Veseli and M. G. Olsson, *hep-ph/9606257*.
- [16] J. M. Cornwall, *Nuclear Physics B*, **128**, 75 (1977).
- [17] J. S. Kang and H. J. Schnitzer, *Physical Review D*, **12**, 841 (1975).
- [18] A. D. Martin and T. D. Spearman, *Elementary Particle Theory*, (Wiley, New York, 1970), 427.
- [19] D. Kahana, K. Maung Maung and J. W. Norbury, *Physical Review D*, **48**, 3408 (1993).
- [20] S. Godfrey and N. Isgur, *Physical Review D*, **32**, 189 (1985).
- [21] W. K. Tang, *Physical Review D*, **48**, 2019 (1993).
- [22] A. Brandt, S. Erhan, A. Kuzucu, D. Lynn, M. Medinnis, N. Ozdes, P. E. Schlein, M. T. Zeyrek and J. G. Zweizig, *Nuclear Physics B*, **514**, 3 (1998).
- [23] L. Burakovsky, *hep-ph/9810296*.
- [24] M. M. Brisudová, L. Burakovsky and T. Goldman, *Physical Review D*, **61**, 054013 (2000).
- [25] D. Haidt and P. M. Zerwas, *The European Physical Journal C*, **3**, 109 (1998).
- [26] H. Grosse and A. Martin, *Particle Physics and the Schrödinger Equation*, (Cambridge University Press, Cambridge, 1997).
- [27] S. Filipponi, *Physical Review D*, **58**, 016003 (1998).
- [28] A. Inopin and G. S. Sharov, *hep-ph/9905499*.
- [29] G. M. Prospero, *hep-ph/9906237*.
- [30] M. Baldicchi, *hep-ph/9911268*.

- [31] J. W. Norbury, K. M. Maung and D. E. Kahana, *Physical Review A*, **50**, 2075 (1994).
- [32] J. W. Norbury, K. M. Maung and D. E. Kahana, *Physical Review A*, **50**, 3609 (1994).
- [33] K. M. Maung, D. E. Kahana and J. W. Norbury, *Physical Review D*, **47**, 1182 (1993).
- [34] D. E. Kahana, K. M. Maung, and J. W. Norbury, *Physical Review D*, **48**, 3408 (1993).
- [35] J. W. Norbury, D. E. Kahana and K. M. Maung, *Canadian Journal of Physics*, **70**, 86 (1992).
- [36] A. Tang, *hep-ph/0103035*.
- [37] W. H. Press, S. A. Teukolsky, W. T. Vetterling and B. P. Flannery, *Numerical Recipes in C*, (Cambridge: Cambridge, 1997).
- [38] I. H. Sloan, *Journal of Computational Physics*, **3**, 322 (1968).
- [39] E. T. Copson, *An Introduction to the Theory of Functions of a Complex Variable*, (New York: Oxford, 1962), 287.
- [40] M. Abramowitz and I. A. Stegun, *Handbook of Mathematical Functions*, (Washington, D. C.: National Bureau of Standards, 1964), 334.
- [41] R. Cc. Weast, *Handbook of Tables for Mathematics*, (Cleveland: CRC, 1975), 783.
- [42] D. E. Kahana, K. M. Maung and J. W. Norbury, *Physical Review D*, **48**, 3408 (1993).
- [43] A. Tang, G. Nill and D. Shillinglaw, *quant-ph/0011116*.
- [44] A. Tang and J. W. Norbury, *Physical Review D*, **62**, 016006 (2000).
- [45] M. Kaku, *Introduction to Superstrings*, (Springer-Verlag, 1988).

- [46] J. I. Illana, *hep-ph/0110092* (9 October 2001).
- [47] N. Isgur, *Physical Review*, **D60**, 114016 (1999).
- [48] N. Isgur and H. B. Thacker, *Physical Review*, **D64**, 094507 (2001).
- [49] B. Andersson, *The Lund Model.*, (Cambridge Univ. Press, 1998).
- [50] B. Andersson and F. Söderberg, *European Physics Journal*, **C16**, no. 30, (2000).
- [51] B. Andersson, S. Mohanty and F. Söderberg, *hep-ph/0106185*, (16 June 2001).
- [52] T. Sjöstrand, L. Lönnblad and S. Mrenna, *hep-ph/0108264*, (31 August 2001).
- [53] S. R. Blattnig, S. R. Swaminathan, A. T. Kruger, M. Ngom and J. W. Norbury, *NASA Technical Paper*, NASA/TP-2000-210640, (December 2000).
- [54] G. P. Lepage, *Cornell University Publication*, CLNS-80/447 (1980).
- [55] J. Pumplin, D. R. Stump, J. Huston, H. L. Lai, P. Nadolsky, and W. K. Tung, *hep-ph/0201195* (22 January 2002).
- [56] R. D. Field and R. P. Feynman, *Nuclear Phys.*, **B136**, 1-76 (1978).
- [57] C. Y. Wong, *Introduction to High-Energy Heavy-Ion Collisions*, (Singapore: World Scientific, 1994).
- [58] T. Iitaka, *Physical Review E*, **49**, 4684 (1994).
- [59] S. Succi, *Physical Review E*, **53**, 1969 (1996).
- [60] J. J. Sakurai, *Modern Quantum Mechanics*, (Redwood City, CA: Addison- Wesley, 1985), 238-242.
- [61] I. S. Gradshteyn and I. M. Ryzhik, *Tables of Integrals, Series, and Products*, (San Diego: Academic, 1980), 526.
- [62] S. Gasiorowicz, *Quantum Physics* (New York: Wiley, 1974), 197.
- [63] J. Polchinski, *Introduction to String Theory*, (Cambridge Univ. Press, 1998).

- [64] B. Hatfield, *Quantum Field Theory of Point Particles and Strings*, (Addison-Wesley, 1992).
- [65] T. J. Allen, C. Goebel, M. G. Olsson and S. Veseli, *Physical Review*, **D64**, 094011 (2001).
- [66] R. D. Field, *Applications of Perturbative QCD*, (Addison-Wesley, 1989).
- [67] B. L. Combridge, J. Kripfganz and J. Ranft, *Phys. Lett.*, **70B**, 2, 234-238 (26 September 1977).

Alfred Tang

Dissertation Title

Topics in Hadronic Physics

Place of Birth

Hong Kong

Degrees

University of Wisconsin - Milwaukee,	1999-2002, Ph.D.
University of Wisconsin - Milwaukee,	1997-1999, M.S.
Biola University,	1991-1997, Th. M.
Biola University,	1988-1991, M. Div.
Massachusetts Institute of Technology,	1984-1987, B.Sc.

Publications

1. "Nystrom plus Correction Method for Solving Bound State Equations in Momentum Space" (Alfred Tang and John W. Norbury), *Physical Review*, **E63**, 066703 (2001).
2. "Properties of Regge Trajectories" (Alfred Tang and John W. Norbury), *Physical Review*, **D62**, 016006 (2000).
3. "Observation of Charge Induced Recovery of Ozone Concentration after Catalytic Destruction by Chlorofluorocarbons" (A. Y. Wong, D. K. Sen-sharma, A. W. Tang, R. G. Suchanek and D. Ho), *Physical Review Letters*, **72**, 3124-3127 (1994).

Presentations

1. “Nystrom plus Correction Method for Solving Bound State Equations in Momentum Space,” APS Annual Meeting (April 2001), Washington, D. C.
2. “A Brief Introduction to Regge Trajectories,” APS Annual Meeting (April 2000), Long Beach, CA.
3. “Mitigation of Catalytic Destruction of Ozone,” Conference of Research Trends in Environmental Physics (November 1993), La Jolla International School of Physics, La Jolla, CA.

Major Department

Physics

Professor John W. Norbury

Date